Title	Theoretical Study on the Mechanism of Transition Metal Catalyzed Reactions and Spin-Forbidden Reactions
Author(s)	趙, 黎明
Citation	北海道大学. 博士(理学) 甲第14255号
Issue Date	2020-09-25
DOI	10.14943/doctoral.k14255
Doc URL	http://hdl.handle.net/2115/82731
Type	theses (doctoral)
File Information	Zhao_Liming.pdf

Theoretical Study on the Mechanism of Transition Metal Catalyzed Reactions and Spin-Forbidden Reactions

Zhao Liming

Hokkaido University

2020

遷移金属錯体による触媒反応および スピン禁制反応のメカニズムに関する 理論的研究

趙　黎明

北海道大学

2020

Contents

Chapter 1. General Introduction

1.1 Transition metal catalysts 5
1.2 Spin in chemical reactions 6
    1.2.1 Spin crossing in biological system 7
    1.2.2 Spin crossing in inorganic reaction 8
1.3 Theoretical perspective of spin-forbidden reactions 10
    1.3.1 Minimum energy intersystem crossing point 11
    1.3.2 Methods to optimize ISC points 14
    1.3.3 Spin-orbit coupling 19
1.4 Overviews of the thesis 20

Chapter 2. Theoretical Study on the Rhodium-Catalyzed Hydrosilylation of C=C and C=O Double Bonds with Tertiary Silane

2.1 Introduction 28
2.2 Computational details 31
2.3 Results and discussion 33
    2.3.1 Oxidative addition of hydrosilane to the catalyst 33
    2.3.2 Formation of active species 34
    2.3.3 Chalk-Harrod (CH) mechanism 35
    2.3.4 Modified Chalk-Harrod (mCH) mechanism 38
    2.3.5 Alternative Chalk-Harrod (aCH) mechanism 40
    2.3.6 Double hydride (DH) mechanism 45
    2.3.7 Outer-sphere mechanism 53
2.4 Conclusion 54

Chapter 3. Controlled Intersystem Crossing in Myoglobin Catalyzed Cyclopropanation: A Theoretical Study

3.1 Introduction..60
    3.1.1 Experimental background..60
    3.1.2 Theoretical background..63
3.2 Computational details..67
    3.2.1 Small model..68
    3.2.1 Large model..68
3.3 Results and discussions..73
    3.3.1 Small model..73
    3.3.2 Large model..80
3.4 Conclusions..91

Chapter 4. Method Development and Applications for Finding Reaction Pathway Including Intersystem Crossing

4.1 A example of multiple states reaction..98
    4.1.1 Introduction..98
    4.1.2 Computational details..100
    4.1.3 Results and discussions..100
    4.1.4 Conclusions..103
4.2 Nudged elastic band method development for multiple states reactions..103
    4.2.1 Introduction..103
    4.2.2 NEB method..106
    4.2.3 Multiple spin states NEB method..107
    4.2.4 Computational details..110
    4.2.5 Benchmark calculations..111
        A. C-C double bond rotation of ethylene..111

B. In-catalyzed C-H bond activation 113
C. Activation of methane by CoH^+ 117
4.2.6 Conclusions 121

Chapter 5. General Conclusion

Chapter 1

General introduction

1.1 Transition metal catalysts

Catalysts are one of the central topics of the chemistry and closely related to our daily life. The transition metal catalysts are no doubt the heart of homogeneous catalyst. The advantages of the homogeneous catalysts are not limited to the state-of-the-art chemical synthesis in the forefront of fundamental chemistry. Overcoming difficulties in practical application, many successful applications in industrial process are reported. One of the famous examples is Suzuki-Miyaura coupling for chemical synthesis in material and pharmaceutical industries. There are diverse kinds of transition metal complexes and many of them are designed as the catalysts. The wide applications of transition metal catalysts can be found in C-C bond activation,[1] C-H bond activation and functionalization,[2, 3] hydrosilylation,[4, 5] polymerization reaction,[6, 7] hydrogenation,[8, 9] dehydrogenation[10] and other fundamental or frontier chemical reactions. These catalysts can dramatically reduce the energy barrier that either can reduce the experimental pressure or lower the temperature and consequently improve the reaction efficiency. Theoretical researches on the mechanism of transition metal catalyzed reactions not only help to understand the reaction better but also help to design more efficient catalyst.

Transition metal catalysts are extensively utilized for hydrosilylation of organic compounds. Hydrosilylation has been especially investigated for its versatility in the reduction of unsaturated chemical compounds such as ketones and alkenes to generate organosilicon products.[11-15] Metal complexes such as iron-[16, 17], ruthenium-[18, 19], nickel-[20], platinum-[21, 22] complexes are active catalysts for the hydrosilylation of C=C and C=O double bonds. Among these catalysts, Rh-containing catalysts occupy a prominent place in hydrosilylation reactions because mild reaction conditions are available. Chalk-Harrod mechanism and modified Chalk-Harrod mechanism are two famous classical mechanisms to understand hydrosilylation reaction. More explanation about these two mechanisms and two newly proposed mechanisms can be found in Chapter 2.

1.2 Spin in chemical reactions

Because transition metal has active d orbital electrons, these reactions may also take place on multiple spin surfaces. Spin crossing reactions are, therefore, of our research interest. Many textbooks of quantum mechanics mentioned the famous Stern-Gerlach experiment in 1922 which first showed the existence of spin.[23] In that experiment, one silver atom beam passed through an inhomogeneous magnetic field and was deflected into two directions. In 1925, Uhlenbeck and Goudsmit first proposed the hypothesis[24, 25] that electron has intrinsic property of spin. In 1928, Dirac developed the relativistic treatment of spin.[26] His elegant work gave a correct description of the effects connected with spin such as the spin-orbit coupling.[27]

Since spin was discovered as the intrinsic property of electron, the discussion about the role of electronic spin in chemical reactions has been a long-standing issue. The reactions in which the reactant spin state is different from the product spin state are called *spin-forbidden reactions*. Because the majority of chemical reactions are taken place on single potential energy surfaces (PES),[28] spin-forbidden reactions were thought to be difficult to take place or to be very slow basing on the experimental observations. For example, the coordination of CO to the $Fe(CO)_4$ (the ground state is triplet) to form $Fe(CO)_5$ (the ground state is singlet) is found to be 500 times slower than the coordination of CO to the $Fe(CO)_3$ (the ground state is triplet).[29] On the other hand, a paper published in 1995 demonstrated experimentally the spin-forbidden reaction can be rapid.[30] In that work, the CO addition or elimination to the Co-complex would change the total spin state but the reaction can proceed fast. And then, there are many other evidences in the experiment support either spin change accelerating the reaction or the spin change slowing the reaction.

Recent years, spin-forbidden reactions have been common in metal compounds. Relative studies can be found in biochemistry, inorganic chemistry, as well as organic chemistry. To name a few, the reactions catalyzed by heme protein family and cytochrome P450s family, the metal complexes catalyzed C-H bond activations, transition metal ligand association and dissociation. The spin changes are ubiquitous in heme protein catalysts. In the following subsections, some more detail examples well be explained.

1.2.1 Spin crossing in biological system

One of the most well-known examples of spin crossing in biological system may be the oxygen binding to the heme. This is an important reaction inside human because the heme works as the carrier to transport oxygen to the cells throughout the body. This seemingly simple reaction actually has complex spin crossing process. The ground states of the deoxyheme and oxygen are quintet and triplet, respectively. Their binding product oxyheme, however, is in the singlet state as tested in the experiments.[31, 32] There is a theoretical study investigated seven lowest electronic states in this binding reaction.[33] They found in a region where the Fe-O distance is more than 2.5 Å, the calculated seven electronic states are almost parallel to each other. These near-degenerate states facilitate the spin crossing. Thus, although the spin-obit coupling (SOC, also known as spin-orbit interaction) is very weak in the heme, the spin-transition possibility was estimated to be 0.06 to 1.[33] Comparing with much smaller spin-transition possibility in nonbiological $Fe-O^+$ system, the porphyrin and proximal heme ligand was found to effectively accelerate the O_2 binding to the heme. More detailed electronic structure of the Fe-O bond and the effect of the protein environment can be found in another QM/MM and pure QM study.[34]

Intersystem crossing often appears in the hemoprotein catalyzed reactions. For example, in a cytochrome P450 catalyzed carbene-transfer reaction where the carbene is inserted into the S-H bond,[35] the ground state of iron-carbene, intermediate, transition state, and the product are in the different spin states. At least five spin surfaces are involved, including open-shell singlet, doublet, triplet, quintet, and sextet. The actual spin inversion can be extremely complex. Recently, the mutations of heme protein are hot topic for the high catalytic activity and the research about spin-change helps to reveal the mechanism behind. A special case study will be discussed in Chapter 3.

1.2.2 Spin crossing in inorganic reaction

a) Transition metal catalyzed C-H bond activation

Significant amount of C-H bond activations was found to be related to the spin changes. One typical example is the Theopold's complex (Cobalt(III) imido complex) catalyzed C-H bond activation.[36] A recent mechanistic study shows the evidence of spin crossover in that reaction.[37] In that study, they used NMR spectroscopy, VT crystallography, and magnetic susceptibility measurements and confirmed the spin crossing in the reaction. Moreover, they found the use of low coordination number ligands can create a sufficiently compressed ligand field which favors the electronic states with unpaired electrons. In other words, by controlling the ancillary ligand field strength can approach higher spin state of Co^{III} imidos complex and therefore change the reactivity of the complex.

Indium catalyzed methane C-H bond activation[38] and CoH^+ catalyzed C-H bond activation were also well-known examples.[39] In the first study, the liquid Indium catalyzed dehydrogenation of methane, and low-coordinated Indium atoms, which appears on gas/liquid interface, are best described by small Indium clusters such as In_2 model because of the lowest activation energy among several Indium clusters. With this small model, the potential energy profile was calculated for different electronic states. A spin crossing was found between the singlet state and the triplet state because the spin multiplicity of the reactant and the product is not the same. For the second study, not only CoH^+ but also FeH^+ and NiH^+ were used as the catalyst. Such reactions that transition metal ions catalyzed C-H bond activation of small alkanes are designed to reveal the intrinsic interaction between the metal ions and the C-H bonds. Through density functional theory (DFT) calculation, they found in all three cases although the reactants and the products are in the same spin states (quintet for the case of FeH^+, quartet for the case of CoH^+, and triplet for the case of NiH^+), the most stable states of the transition states are different from those in the reactant and product states. This is because the electronic structures of reactants and products prefer a $3d^{n-1}4s^1$ electron configuration, however, the transition states prefer a $3d^n$ electronic structure. Consequently, lead to the spin crossing mode of high spin-low spin-high spin. In chapter 4, our program reproduced the feature of such reaction pathway and even generated the structures of the crossing points simultaneously.

b) Other transition metal involved reactions

Except for the C-H bond activation reaction, there are also plenty examples of spin-forbidden reactions in transition-metal involved reactions. One well-known example is the ligand association and dissociation as mentioned CO association reaction. The unligated metal atoms or the ions prefer high spin electronic structure because of the degenerated d orbitals. The ligands tend to stabilize the complex to low spin states because of the ligand field which leads to the splitting of the degenerated orbitals.

Transition metal oxo species are another example of spin crossing. Transition metal oxo species have the form M=O, where M can be iron, chromium, manganese, and so on. There is a very recent and interesting theoretical research about the reactivity of such oxo species by using minimum energy crossing point (MECP) method and transition state SOC (TS SOC) method.[40] Simply say, the MECP method is to locate the spin crossing point on two diabatic surfaces. The TS SOC method is to locate the transition point on the adiabatic surface by including the SOC term. The definition of diabatic and adiabatic surface can be found in subsection 1.2.1. TS SOC method has been applied to very limited case studies because of the relativistic calculation is quite time-consuming. In many cases, this newly applied TS SOC method would give similar results as MECP method does, although an exception was reported.[41] In the recent study,[40] through three cases study, cycloaddition of ethylene to chromyl chloride, iron oxide cation insertion into hydrogen molecule, and H-abstraction from toluene by a Mn^{V}-oxo-porphyrin cation, the energy surfaces calculated by TS SOC method and MECP method are very similar to each other. The positions of the spin crossing points are as well alike. Consequently, in the usual cases, these two methods can give qualitatively and quantitatively similar results. Other introductions and discussions about spin crossing of transition metal involved reactions can be found in reviews or books.[42-44]

1.3 Theoretical perspective of spin-forbidden reactions

As mentioned in subsection 1.1, there were debates whether spin crossing slows the reaction. The rapid development of theoretical chemistry helps to understand the contradictory experimental observations.

The origin of spin crossing can be attributed to the SOC. In the nonrelativistic quantum chemistry description, the total Hamiltonian can be written as equation (1):

$$H_{tot} = T_n + V_{nn} + T_e + V_{ne} + V_{ee} \tag{1}$$

where T_n and T_e represent the kinetic energy of nuclei and electrons, respectively. V_{nn}, V_{ne}, and V_{ee} are the coulomb interaction between nuclei and nuclei, nuclei and electrons, and electrons and electrons, respectively. The total Hamiltonian can be divided into two parts, the first two items on the left side of equation 1 is noted as nuclei Hamiltonian and the rest items is called electronic Hamiltonian (H_e). In the Born-Oppenheimer approximation, the electrons are moving much faster than the nuclei. Thus, the electrons can be assumed to move under the fixed nuclei potential so that the nuclei Hamiltonian can be ignored because it only contributes a constant term in the final solution. The explicit form of H_e is

$$H_e = -\frac{1}{2}\sum_i \nabla_i^2 - \sum_i \sum_A \frac{Z_A}{r_{iA}} + \sum_i \sum_{j>i} \frac{1}{r_{ij}}. \tag{2}$$

The i and A index electrons and nuclei, respectively. Obviously, the electronic Hamiltonian doesn't contain the operator related to spin. The full answer about spin needs to be found in the relativistic quantum chemistry where the spin operator is included. On the other hand, for the investigation of the mechanisms of the spin-forbidden reactions, the geometry information of the spin crossing points is very crucial, especially, the minimum energy intersystem crossing point (MEISCP). The tools of nonrelativistic quantum chemistry are strong enough to find such geometries of these MEISCPs.

1.3.1 Minimum energy intersystem crossing point

As shown in Fig. 1, two spin surfaces may cross in some region which is called crossing seam. On the seam, the lowest point is called MEISCP which is the spin inversion junction. For simplicity, sometimes it is just called intersystem crossing (ISC) point. ISC point takes the role like the "transition state" in the minimum energy pathway (MEP) that connecting two minima in different spin surface. In fact, the surfaces in Fig. 1 are the diabatic surfaces so that the "hopping" happens at a crossing point. If we describe the PES by using adiabatic surface, the ISC point is exactly a transition state as shown in Fig. 2. The difference between diabatic and adiabatic surface lies in the form of Hamiltonian. For the adiabatic surfaces, the Hamiltonian contains SOC term which is omitted in calculation of diabatic surfaces. The energy difference at the crossing point on the adiabatic surface is determined by spin-orbit coupling strength $H_{12} =< \Psi_1|H_{SOC}|\Psi_2 >$.[45] Consequently, unless the SOC matrix equals to zero, at the crossing point there is a small energy gap. Obviously, in the adiabatic surfaces description the crossing point is a transition state connecting two minima. In practice, many cases are that the two-states coupling are very weak except for a rather small region near the crossing point. Thus, the system looks like hopping suddenly at the crossing point. So, in most cases we can use both diabatic and adiabatic surfaces to explain the spin-forbidden reactions.

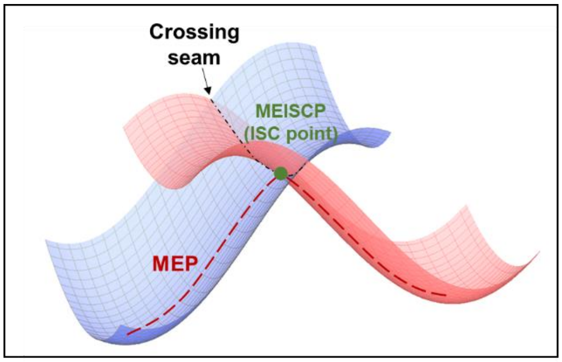

Figure 1 Explanation of crossing seam, MEISCP, and MEP.

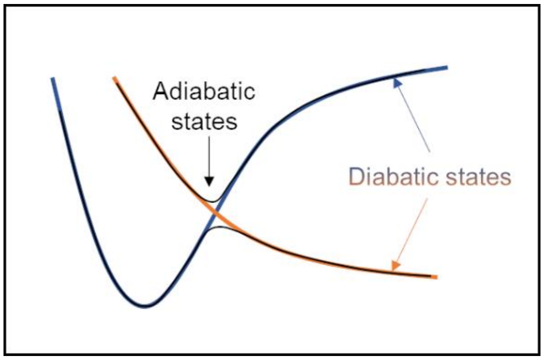

Figure 2 Adiabatic and diabatic surfaces for ISC.

ISC point may become the bottleneck of the reaction in two ways. Fig. 3(a) shows the first case that to reach the crossover point, a relatively high energy barrier needs to be overcomed. In the second case (Fig. 3(b)), although the energy needed to cross the crossing point is lower than the transition state, the SOC could be weak at that region. Consequently, particles can't easily go to another spin surface and therefore the spin inversion step becomes the rate-determining step.

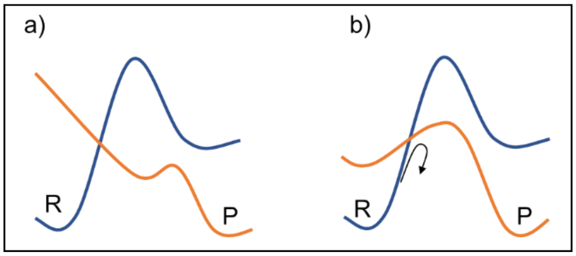

Figure 3 Two ways that ISC points influence the reaction rate

Inversely, if the spin-orbit coupling is strong in the second case, the reaction can be greatly accelerated because the spin crossing leads to a much lower energy barrier.

The relative energy of the ISC points provide the qualitative information of the reactivity. The properties of the ISC points also allow us to quantitatively calculate the spin-forbidden reaction rate constant. From above discussion, it is obvious that there are two factors influence the chemical reactivity of spin-forbidden reaction. First, the necessary energy to reach the ISC point from the reactant. Second, the possibility of surface hopping from one spin state to another. This factor is greatly determined by the SOC term of the two crossing surfaces. Considering these two factors and the traditional transition state theory (TST), a variant of TST, called non-adiabatic TST, was used to estimate the reaction rate in spin-forbidden reactions.[45] The canonical expression for the reaction rate is:

$$k(T) = \frac{1}{hQ_R(T)}\int_0^{\infty} N_{cr}(E)e^{-\frac{E}{k_B T}}dE \qquad (3-A)$$

$$N_{cr}(E) = \int dE_h \rho_{cr}(E-E_h)\rho_{sh}(E_h) \qquad (3-B)$$

where h is the Planck constant, Q_R is the partition function for the reactants, k_B is the

Boltzmann constant in equation 3-A. $N_{cr}(E)$ represents for the effective number of all the rovibrational states near the MECP to cross the intersection seam. Consequently, it is calculated by integrating two kinds of states density, ρ_{cr} and ρ_{sh}. ρ_{sh} is the density of states that represents the motion in the vertical direction (also known as the "hopping" coordinate) to cross the seam. The SOC term is included in this term. ρ_{cr} is the density of states which contains the motion parallel to the crossing seam, thus it is also called the "spectator" degrees. More details about equation 3 can be found in the references.[45, 46] An open source package called MESMER includes this theory to calculate the spin-forbidden reaction coefficient.[47]

1.3.2 Methods to optimize ISC points

There are three types of methods for locating conical intersection points, and therefore also ISC points. In this section, the theory behind these three methods will be explained.

a) Lagrange-Newton method

The first type of the method was proposed by Yarkony in 1993, known as Lagrange-Newton method.[48, 49] An earlier development by Koga and Morokuma falls into this category.[50] The crossing point is determined by minimizing the Lagrange function

$$L_{IJ}(\boldsymbol{R},\boldsymbol{\xi},\boldsymbol{\lambda}) = E_I + \xi_1(E_I - E_J) + \xi_2 H_{IJ} + \sum_{i=1}^{M} \lambda_i C_i(\boldsymbol{R}), \tag{4}$$

where H_{IJ} is defined by

$$H_{IJ} = \langle \Psi_I | \mathbf{H} | \Psi_J \rangle \tag{5}$$

In equation 4, the first term on the right side minimize the energy of one state. As we know, at the crossing point, the two electronic surfaces are energetically equal to each other. We can choose to minimize either of the states or the average of the two states. The mandatory constraints of the Lagrange-Newton method are

$$E_I - E_J = 0 \tag{6}$$

and

$$H_{IJ} = 0, \tag{7}$$

which are the second and third terms of equation 4. The last term in equation 4 allows certain geometric constraints during the optimization, such as the bond lengths or the angles.

Recalling the Newton-Raphson method, a function $f(x)$ can be expanded according to the Taylor series

$$f(x) = f(x^k) + g_k(x - x^k) + \frac{1}{2}(x - x^k)^T H(x^k)(x - x^k), \tag{8}$$

Where g_k and $H(x^k)$ are the gradient and the second-order derivative of $f(x)$ at $x = x^k$, respectively. At the extrema, the gradient of function $f(x)$ equals to 0. Thus, we can write

$$\nabla f(x) = g_k + H(x^k)(x - x^k) = 0. \tag{9}$$

Consequently,

$$H(x^k)(x - x^k) = -g_k. \tag{10}$$

Analogous to the Newton-Raphson method (derivation of equation 10), at the extrema, the second order of equation 4 satisfies

$$\begin{pmatrix} \nabla\nabla L_{IJ} & \mathbf{g_{IJ}} & \mathbf{h_{IJ}} & \mathbf{k} \\ \mathbf{g_{IJ}^{\dagger}} & 0 & 0 & \mathbf{0} \\ \mathbf{h_{IJ}^{\dagger}} & 0 & 0 & \mathbf{0} \\ \mathbf{k}^{\dagger} & \mathbf{0} & \mathbf{0} & \mathbf{0} \end{pmatrix} \begin{pmatrix} \delta\boldsymbol{R} \\ \delta\xi_1 \\ \delta\xi_2 \\ \delta\boldsymbol{\lambda} \end{pmatrix} = -\begin{pmatrix} \nabla L_{IJ} \\ E_I - E_J \\ 0 \\ \mathbf{K} \end{pmatrix}. \tag{11}$$

The gradient of L_{IJ} is

$$\nabla L_{IJ} = \mathbf{g_I} + \xi_1 \mathbf{g_{IJ}} + \xi_2 \mathbf{h_{IJ}} + \sum_{i=1}^{M} \lambda_i \mathbf{k_i}\,, \tag{12}$$

in which $\mathbf{g_I}$ is the gradient of E_I. $\mathbf{g_{IJ}}$ and $\mathbf{h_{IJ}}$ are the gradient of $E_I - E_J$ and H_{IJ}, respectively. The Hessian of the Lagrange $\nabla\nabla L_{IJ}$ can be updated by using quasi-Newton methods. In practice, the Broyden-Fletcher-Goldfarb-Shannon (BFGS) method was found to be very efficient.

b) Gradient projection method

One year later, another approach which is called gradient projection method was proposed by Bearpark and coworkers.[51] In this method, instead of using Lagrange multiplier, the minimization of the energy difference $E_I - E_J$ and the one state E_J is conducted at the same time.

First, it is better to introduce two gradient vectors $\mathbf{x_1}$ and $\mathbf{x_2}$ which are defined by

$$\mathbf{x_1} = \frac{\partial}{\partial \boldsymbol{R}}\left(E_I - E_J\right) \tag{13 − A}$$

$$\mathbf{x_2} = \langle C_I^\dagger \left(\frac{\partial \mathbf{H}}{\partial \boldsymbol{R}}\right) C_J \rangle \tag{13 − B}$$

where C_I and C_J are the CI coefficients of state I and J, respectively. It is easy to find that the $\mathbf{x_1}$ and $\mathbf{x_2}$ are indeed equal to $\mathbf{g_{IJ}}$ and $\mathbf{h_{IJ}}$ in equation 12. According to the definition of conical intersection, the degeneracy of the two states is lifted along linearly independent coordinates $\mathbf{x_1}$ and $\mathbf{x_2}$. The gradient of $\mathbf{x_1}$ can be used to minimize $E_I - E_J$ so that the gradient is defined as

$$\mathbf{f}_1 = 2\left(E_I - E_J\right)\frac{\mathbf{x_1}}{|\mathbf{x_1}|}. \tag{14}$$

As for the minimization of the energy of E_J, the gradient of E_J is projected into the intersection space spanned by $\mathbf{x_1}$ and $\mathbf{x_2}$. The direction of the projection is

$$\mathbf{P} = \mathbf{I} - \mathbf{x_1}\mathbf{x_1^T} - \mathbf{x_2}\mathbf{x_2^T}. \tag{15}$$

The corresponding gradient is

$$\mathbf{f_2} = \mathbf{p}\frac{\partial E_J}{\partial \boldsymbol{R}}. \tag{16}$$

The final gradient is the combination of $\mathbf{f}_1$ and $\mathbf{f}_2$,

$$\mathbf{g} = a_0[a_1\mathbf{f}_1 + (1 - a_1)\mathbf{f}_2], \qquad (a_0 > 0, 0 < a_1 \leq 1) \tag{17}$$

where a_0 and a_1 are user defined constants. The quasi-Newton method is also used for this optimization with BFGS scheme for the hessian updating.

Here we have a simple introduction for the BFGS method. To implement Newton method programmatically, the equation 10 is written as

$$x^{k+1} = x^k - g_k H^{-1}(x^k). \tag{18}$$

The second term on the right can be seen as the search direction. However, the calculation of the H^{-1} matrix is not an easy task. To solve this problem, BFGS method was proposed. Recall equation 9, if we substitute x by x^{k-1}, then we can get

$$g_k - g_{k-1} = H_k(x^k - x^{k-1}), \tag{19}$$

where $H_k = H(x^k)$. The basic idea of BFGS method is to use a matrix approximate B_k to replace H_k. The initial B_0 is an unit matrix. The matrix B_k is determined according to the matrix B_{k-1}, g_{k-1}, g^k x^{k-1}, and x^k.

c) Penalty function method

In 2004, penalty function method was proposed by Ciminelli et al.[52] The original form of object function is written as

$$f(\boldsymbol{R}) = \frac{E_I + E_J}{2} + c_1 c_2^2 \ln\left[1 + \left(\frac{E_I - E_J}{2}\right)^2\right] \tag{20}$$

where c_1 and c_2 are the user defined constants. Obviously, the first term minimizes the average energy of the two states while the second term minimize the energy difference. Later, another forms of the object function was proposed by Benjamin,[53] which is

$$f(\boldsymbol{R}) = \frac{E_I + E_J}{2} + \sigma \frac{\left(E_I - E_J\right)^2}{\left(E_I - E_J\right) + \alpha}. \tag{21}$$

In this definition, E_I is the upper state. The updating branching plane method would also be classified as a penalty function method.[54]

The biggest advantage of the penalty function is that, during the optimization there is no need to calculation the two state intersect coupling term ($\mathbf{h_{IJ}}$) which is required in both Lagrange-Newton method and gradient projection method. The calculation of intersect coupling term is only available when the method can calculate more than one electronic state at the same time like full CI or MCSCF (Multi-Configuration Self-Consistent Field) method. Consequently, that two methods can’t be applied to some electronic methods like widely used density function theory or the perturbation theory. People may wonder if the MEISCP located by the penalty function method is close enough to the real crossing point. It is said that with acceptable small energy gap, in most cases the optimized structure is the near-degenerate crossing point.[53]

This two-states penalty function method was applied in some packages, such as our group self-developed codes or the global reaction route mapping (known as GRRM) program.[55] Recently, the penalty function method was broadened to the three-states system and was even applied to the QM/MM system.[56]

Now we have introduced three methods for the optimization of the ISC points. A common feature of the three approaches are that an initial guess for the ISC point optimization is required. We can easily give an initial guess to the traditional transition state according to our chemical knowledge and experience. However, to guess the structure of an ISC is not much tougher. Current method is to do a scan calculation along the reaction coordination such as the bond length, angle or dihedral on one certain spin surface. Then, do a series of single point energy calculation at each structure from scan calculation on another spin surface. The structure with least energy gap will be the candidate for the ISC optimization. However, according to our experience, this method often can't promise a good initial guess. In chapter 3, we will give a solution to this problem.

1.3.3 Spin-orbit coupling

Sometimes it is not enough just to locate the spin crossing point because we know the region around that point is influenced much by the nonadiabatic effects. How difficult can the system transfer to another spin state should be concern. In this sense, the strength of SOC should be considered.

The operator include SOC can be found in the relativistic quantum chemistry, which is known as Breit-Pauli Hamiltonian (equation 22).[57]

$$H_{SO} = \sum_{A}\sum_{i} \frac{e^2\hbar}{2m^2c^2}\frac{Z_A}{r_{iA}^3}\boldsymbol{S}_i(\boldsymbol{r}_i \times \boldsymbol{p}_i) - \sum_{i\neq j} \frac{e^2\hbar}{2m^2c^2}\frac{1}{r_{ij}^3}(\boldsymbol{r}_{ij} \times \boldsymbol{p}_i)(\boldsymbol{S}_i + 2\boldsymbol{S}_j) \tag{22}$$

A and i index the nuclei and electrons, respectively. Z_A represents the nuclei charge. According to the involved number of electrons, the first term is called one-electron term and the second is called the two-electron term. In the computational chemistry, it was found that the two-electron term is rather time consuming, and thus, an approximate of Breit-Pauli Hamiltonian is adopted.[58] The alternate is written as

$$H_{SO} \cong \left(\frac{\alpha^2}{2}\right)\sum_{i}\sum_{A} \frac{Z_{eff}(A)}{r_{iA}^3}\boldsymbol{S}_i(\boldsymbol{r}_i \times \boldsymbol{p}_i), \tag{23}$$

where α is called fine structure constant (the approximate value is $1/137$) and $Z_{eff}(A)$ is the effective charge of the nuclei A. $\boldsymbol{S}_i$, $\boldsymbol{r}_i$ and $\boldsymbol{p}_i$ are the spin matrix, displacement, and momentum of electron i, respectively. The contribution of the two-electron term is considered by choosing proper effective core charges. There are well optimized Z_{eff} values in the literatures.[58, 59] From this equation, the approximate strength of SOC can be estimated.

1.4 Overviews of the thesis

In Chapter 1, the general introduction is explained. In the first, the wild application and importance of transition mental catalysts is addressed. Because of the active d orbital electrons, the spin states are usually a matter of discussion in these reactions and consequently become our research topic. The history of spin in chemical reactions is introduced from the first observation of the spin phenomenon in the experiment to the proper description in the quantum mechanics, then the applications in the chemical reactions. The examples for the spin crossing are listed in three fields, biological system, C-H bond activation, and the transition metal involved reaction. The debating whether the spin crossing slows the reaction is well explained by theoretical chemistry. The background relating to the calculation of spin crossing was then introduced. For computational chemistry, one of the most important point in a spin-forbidden reaction is the ISC point which can be used to reveal the reaction mechanism and estimate the reaction rate. Three different methods for locating ISC point is introduced and also their features and shortcomings. Simple explanation about relativistic quantum chemistry is also introduced.

Chapter 2 is entitled as "Theoretical Study on the Rhodium-Catalyzed Hydrosilylation of C=C and C=O Double Bonds with Tertiary Silane". It is a systematic research about homogenous Rh catalyst in hydrosilylation reaction with ketone and alkene. Previously proposed three mechanisms, Chalk-Harrod (CH) mechanism, modified Chalk-Harrod (mCH) mechanism, as well as outer-sphere mechanism were examined. Besides, we also found two mechanisms, alternative CH (aCH) mechanism and double hydride (DH) mechanism. Different from the expectation that acetone hydrosilylation should take place through mCH mechanism, we found the CH mechanism is much more preferred. Our newly proposed aCH mechanism where the active species is a four coordinated complex was found to have similar energy barrier as the CH mechanism. As we know, CH mechanism is widely applied in many other reactions. Considering the similar performance of CH and aCH mechanism, we suggest to estimate the aCH mechanism if the CH mechanism is found to be applicable. Moreover, the lowest energy barrier of acetone and ethylene hydrosilylation appeared in the newly proposed DH mechanism. The active species of DH mechanism is a six coordinated Rh complex with two Rh-H bonds. We found that the extra Rh-H bond can effectively improve the catalyst's performance. Thus, we suggest to consider strategies to directly synthesize or to generate in situ such a catalyst with double Rh-H bond catalyst to improve the reactivity.

In Chapter 3, "Controlled Intersystem Crossing in Myoglobin Catalyzed Cyclopropanation: a theoretical study", a study investigated the styrene cyclopropanation reaction with ethyl diazoacetale catalyzed by natural and reconstituted myoglobin will be explained. In the experiment, the artificial myoglobin is much more active than the wild-type one. To figure out the reason of the reactivity differences, two computational models were used to explore the reaction mechanism. The smaller one only concerned about the active site by using DFT method. The larger model contains both protein environment, as well as some solvent water, by using quantum mechanics/molecular mechanics (QM/MM) method. Through the small model, basing on three reasons 1) the lower total energy barrier with reconstituted myoglobin; 2) less ISC points in the case of reconstituted myoglobin; 3) easily quenching to the ground state of the reactant in the case of natural myoglobin, it is concluded that the reaction catalyzed by reconstituted myoglobin is more active as consistent with the experiment result. The results from larger model shows similar potential energy surface to the smaller model. However, the relative energy of some intermediates is changed because the protein environment changes the electronic structure of the active site, also the solvent water has interaction with the catalyst through hydrogen-bonding. Finally, it is the first report to apply free energy perturbation method to the iron- carbene system with QM/MM method. Not like the previous work where the additive scheme was used,[60-62] in this work, a subtractive scheme QM/MM method known as ONIOM method was used. The results showed the large activation energy difference between the two catalysts and also indicated the significance of the solvent.

Chapter 4, "Method Development and Applications for Finding Reaction Pathway Including Intersystem Crossing", stated an application of a method to locate MEISCP in multiple spin states reaction and then explained a newly development method which works like intrinsic reaction coordinate (IRC) method to explore the reaction pathway but conducted on the multiple electronic surfaces. In the case study, a newly reported reaction, photo-induced β-elimination of 9-fluorenylmethanol leading to dibenzofulvene, was computationally studied. The process of using theoretical tool to study spin crossing reaction was displayed. The experience of the case studies provided a direction of our method development. Basing on the merits of traditional nudged elastic band method and the penalty function method, we proposed a new approach to combine these two methods and accomplished by Fortran coding. Through this new approach, it is possible to locate the MEISCP and the transition state while optimizing the reaction pathway. The program was tested in three cases, ethylene rotation, In_2 catalyzed C-H bond activation and the CoH^+ catalyzed C-H bond activation. The definition of the candidate for the MEISCP was found significantly important. In the simple cases where only one MEISCP is on the reaction pathway, a so called two-image selection scheme is enough. However, for more complicated case where ISC happens more than once like CoH^+ catalyzed C-H bond activation, we defined a three-image selection scheme to reduce the number of special points. All of the three calculated reaction pathways are converged near to the real MEP. Besides, we also proposed a revised version of multiple states nudged elastic band method to improve the precision of the calculation.

Chapter 5 summarizes the thesis. Except for listing the conclusions of each chapters, the consideration and perspectives about the calculation of spin crossing reaction and the free energy perturbation method for the biological system is explained.

Reference

1. Jun, C.-H., Transition metal-catalyzed carbon–carbon bond activation. *Chem. Soc. Rev.* **2004,** *33* (9), 610-618.
2. Crabtree, R. H., Alkane C–H activation and functionalization with homogeneous transition metal catalysts: a century of progress—a new millennium in prospect. *Dalton Trans.* **2001,** (17), 2437-2450.
3. Dyker, G., Transition Metal Catalyzed Coupling Reactions under C−H Activation. *Angew. Chem. Int. Ed.* **1999,** *38* (12), 1698-1712.
4. Nakajima, Y.; Shimada, S., Hydrosilylation reaction of olefins: recent advances and perspectives. *RSC Advances* **2015,** *5* (26), 20603-20616.
5. Roy, A. K., A Review of Recent Progress in Catalyzed Homogeneous Hydrosilation (Hydrosilylation). In *Advances in Organometallic Chemistry*, West, R.; Hill, A. F.; Fink, M. J., Eds. Academic Press: 2007; Vol. 55, p 1-59.
6. Zhang, J.; Wang, X.; Jin, G.-X., Polymerized metallocene catalysts and late transition metal catalysts for ethylene polymerization. *Coord. Chem. Rev.* **2006,** *250* (1), 95-109.
7. Gromada, J.; Carpentier, J.-F.; Mortreux, A., Group 3 metal catalysts for ethylene and α-olefin polymerization. *Coord. Chem. Rev.* **2004,** *248* (3), 397-410.
8. Widegren, J. A.; Finke, R. G., A review of soluble transition-metal nanoclusters as arene hydrogenation catalysts. *J. Mol. Catal. A-Chem.* **2003,** *191* (2), 187-207.
9. Bond, G. C.; Wells, P. B., The Mechanism of the Hydrogenation of Unsaturated Hydrocarbons on Transition Metal Catalysts. In *Advances in Catalysis*, Eley, D. D.; Pines, H.; Weisz, P. B., Eds. Academic Press: 1965; Vol. 15, p 91-226.
10. Dobereiner, G. E.; Crabtree, R. H., Dehydrogenation as a Substrate-Activating Strategy in Homogeneous Transition-Metal Catalysis. *Chem. Rev.* **2010,** *110* (2), 681-703.
11. Speier, J. L., Homogeneous Catalysis of Hydrosilation by Transition Metals. In *Advances in Organometallic Chemistry*, Stone, F. G. A.; West, R., Eds. Academic Press: 1979; Vol. 17, p 407-447.
12. Harrod, J. F.; Chalk, A. J., Organic Synthesis via Metal Carbonyls. Wender, I.; Pino, P., Eds. John Wiley & Sons Ltd.: New York, 1977; Vol. 2, p 673.
13. Ojima, I., The Hydrosilylation Reaction. In *Organic Silicon Compounds* John Wiley & Sons, Ltd: Chichester, UK., 1989; Vol. 1 and Vol. 2, p 1479-1526.
14. Tilley, T. D., The Chemistry of Organic SIlicon Compounds. Patai, S.; Rappoport, Z., Eds. John Wiley & Sons Ltd.: New York, 1989; p 1415.
15. Du, X.; Huang, Z., Advances in Base-Metal-Catalyzed Alkene Hydrosilylation. *ACS Catalysis* **2017,** *7* (2), 1227-1243.
16. Bleith, T.; Gade, L. H., Mechanism of the Iron(II)-Catalyzed Hydrosilylation of Ketones:

Activation of Iron Carboxylate Precatalysts and Reaction Pathways of the Active Catalyst. *J. Am. Chem. Soc.* **2016,** *138* (14), 4972-4983.
17. Kamata, K.; Suzuki, A.; Nakai, Y.; Nakazawa, H., Catalytic Hydrosilylation of Alkenes by Iron Complexes Containing Terpyridine Derivatives as Ancillary Ligands. *Organometallics* **2012,** *31* (10), 3825-3828.
18. Chatterjee, B.; Gunanathan, C., Ruthenium Catalyzed Selective Hydrosilylation of Aldehydes. *Chem. Commun.* **2014,** *50* (7), 888-890.
19. Beddie, C.; Hall, M. B., A Theoretical Investigation of Ruthenium-Catalyzed Alkene Hydrosilation: Evidence To Support an Exciting New Mechanistic Proposal. *J. Am. Chem. Soc.* **2004,** *126* (42), 13564-13565.
20. Pappas, I.; Treacy, S.; Chirik, P. J., Alkene Hydrosilylation Using Tertiary Silanes with α-Diimine Nickel Catalysts. Redox-Active Ligands Promote a Distinct Mechanistic Pathway from Platinum Catalysts. *ACS Catalysis* **2016,** *6* (7), 4105-4109.
21. Kong, Y. K.; Kim, J.; Choi, S.; Choi, S.-B., Hydrosilylation and Double Silylation of Carbonyl Compounds with 1,1′-bis(dimethylsilyl)ferrocene Using Nickel- and Platinum-Catalysts. *Tetrahedron Lett.* **2007,** *48* (11), 2033-2036.
22. Chandra, G.; Lo, P. Y.; Hitchcock, P. B.; Lappert, M. F., A Convenient and Novel Route to Bis(η-alkyne)platinum(0) and Other Platinum(0) Complexes from Speier's Hydrosilylation Catalyst $H_2[PtCl_6].xH_2O$. X-ray Structure of $[Pt\{(\eta\text{-}CH_2{=}CHSiMe_2)_2O\}(P\text{-}t\text{-}Bu_3)]$. *Organometallics* **1987,** *6* (1), 191-192.
23. Gerlach, W.; Stern, O., Der experimentelle Nachweis der Richtungsquantelung im Magnetfeld. *Zeitschrift für Physik* **1922,** *9* (1), 349-352.
24. Uhlenbeck, G. E.; Goudsmit, S., Ersetzung der Hypothese vom unmechanischen Zwang durch eine Forderung bezüglich des inneren Verhaltens jedes einzelnen Elektrons. *Die Naturwissenschaften* **1925,** *13* (47), 953-954.
25. Uhlenbeck, G. E.; Goudsmit, S., Spinning Electrons and the Structure of Spectra. *Nature* **1926,** *117* (2938), 264-265.
26. Dirac, P. A. M.; Fowler, R. H., The quantum theory of the electron. *Proceedings of the Royal Society of London. Series A, Containing Papers of a Mathematical and Physical Character* **1928,** *117* (778), 610-624.
27. Pauncz, R., *The Construction of Spin Eigenfunctions An Exercise Book*. 1st ed. 2000. ed.; 2000.
28. Swart, M.; Costas Salgueiro, M., *Spin states in biochemistry and inorganic chemistry : influence on structure and reactivity*. 2016; p 103-129.
29. Seder, T. A.; Ouderkirk, A. J.; Weitz, E., The wavelength dependence of excimer laser photolysis of Fe(CO)5 in the gas phase. Transient infrared spectroscopy and kinetics of the Fe(CO)x (x=4,3,2) photofragments. *J. Chem. Phys.* **1986,** *85* (4), 1977-1986.
30. Detrich, J. L.; Reinaud, O. M.; Rheingold, A. L.; Theopold, K. H., Can Spin State Change Slow Organometallic Reactions? *J. Am. Chem. Soc.* **1995,** *117* (47), 11745-11748.
31. Pauling, L.; Coryell, C. D., The Magnetic Properties and Structure of Hemoglobin, Oxyhemoglobin and Carbonmonoxyhemoglobin. *Proc Natl Acad Sci U S A* **1936,** *22* (4), 210-216.
32. Pauling, L., Nature of the Iron–Oxygen Bond in Oxyhæmoglobin. *Nature* **1964,** *203* (4941), 182-183.
33. Jensen, K. P.; Ryde, U., How O2 binds to heme: reasons for rapid binding and spin inversion. *J. Biol. Chem.* **2004,** *279* (15), 14561-9.

34. Chen, H.; Ikeda-Saito, M.; Shaik, S., Nature of the Fe−O2 Bonding in Oxy-Myoglobin: Effect of the Protein. *J. Am. Chem. Soc.* **2008,** *130* (44), 14778-14790.
35. Chen, K.; Zhang, S.-Q.; Brandenberg, O. F.; Hong, X.; Arnold, F. H., Alternate Heme Ligation Steers Activity and Selectivity in Engineered Cytochrome P450-Catalyzed Carbene-Transfer Reactions. *J. Am. Chem. Soc.* **2018,** *140* (48), 16402-16407.
36. Shay, D. T.; Yap, G. P. A.; Zakharov, L. N.; Rheingold, A. L.; Theopold, K. H., Intramolecular C H Activation by an Open-Shell Cobalt(III) Imido Complex. *Angew. Chem. Int. Ed.* **2005,** *44* (10), 1508-1510.
37. King, E. R.; Sazama, G. T.; Betley, T. A., Co(III) Imidos Exhibiting Spin Crossover and C–H Bond Activation. *J. Am. Chem. Soc.* **2012,** *134* (43), 17858-17861.
38. Ohtsuka, Y.; Nishikawa, Y.; Ogihara, H.; Yamanaka, I.; Ratanasak, M.; Nakayama, A.; Hasegawa, J.-y., Theoretical Study on the C–H Activation of Methane by Liquid Metal Indium: Catalytic Activity of Small Indium Clusters. *J. Phys. Chem. A* **2019,** *123* (41), 8907-8912.
39. Zhang, Q.; Bowers, M. T., Activation of Methane by MH+ (M = Fe, Co, and Ni): A Combined Mass Spectrometric and DFT Study. *J. Phys. Chem. A* **2004,** *108* (45), 9755-9761.
40. Ricciarelli, D.; Belpassi, L.; Harvey, J. N.; Belanzoni, P., Spin-Forbidden Reactivity of Transition Metal Oxo Species: Exploring the Potential Energy Surfaces. *Chem. Eur. J.* **2020,** *26* (14), 3080-3089.
41. Demissie, T. B.; Garabato, B. D.; Ruud, K.; Kozlowski, P. M., Mercury Methylation by Cobalt Corrinoids: Relativistic Effects Dictate the Reaction Mechanism. *Angew. Chem. Int. Ed.* **2016,** *55* (38), 11503-11506.
42. Harvey, J. N.; Cundari, T. R., *Spin-Forbidden Reactions in Transition-Metal Chemistry*. 2001.
43. Poli, R.; Harvey, J. N., Spin forbidden chemical reactions of transition metal compounds. New ideas and new computational challenges. *Chem. Soc. Rev.* **2003,** *32* (1), 1-8.
44. Brik, M. G.; Camardello, S. J.; Srivastava, A. M.; Avram, N. M.; Suchocki, A., Spin-Forbidden Transitions in the Spectra of Transition Metal Ions and Nephelauxetic Effect. *ECS J. Solid State Sci. Technol.* **2015,** *5* (1), R3067-R3077.
45. Harvey, J. N., Understanding the kinetics of spin-forbidden chemical reactions. *Phys. Chem. Chem. Phys.* **2007,** *9* (3), 331-343.
46. Harvey, J. N., Spin-forbidden reactions: computational insight into mechanisms and kinetics. *WIRES Comput. Mol. Sci.* **2014,** *4* (1), 1-14.
47. Glowacki, D. R.; Liang, C.-H.; Morley, C.; Pilling, M. J.; Robertson, S. H., MESMER: An Open-Source Master Equation Solver for Multi-Energy Well Reactions. *J. Phys. Chem. A* **2012,** *116* (38), 9545-9560.
48. Yarkony, D. R., Systematic determination of intersections of potential energy surfaces using a Lagrange multiplier constrained procedure. *J. Phys. Chem.* **1993,** *97* (17), 4407-4412.
49. Manaa, M. R.; Yarkony, D. R., On the intersection of two potential energy surfaces of the same symmetry. Systematic characterization using a Lagrange multiplier constrained procedure. *J. Chem. Phys.* **1993,** *99* (7), 5251-5256.
50. Koga, N.; Morokuma, K., Determination of the lowest energy point on the crossing seam between two potential surfaces using the energy gradient. *Chem. Phys. Lett.* **1985,** *119* (5), 371-374.
51. Bearpark, M. J.; Robb, M. A.; Bernhard Schlegel, H., A direct method for the location of the lowest energy point on a potential surface crossing. *Chem. Phys. Lett.* **1994,** *223* (3), 269-

274.
52. Ciminelli, C.; Granucci, G.; Persico, M., The Photoisomerization Mechanism of Azobenzene: A Semiclassical Simulation of Nonadiabatic Dynamics. *Chem. Eur. J.* **2004,** *10* (9), 2327-2341.
53. Levine, B. G.; Coe, J. D.; Martínez, T. J., Optimizing Conical Intersections without Derivative Coupling Vectors: Application to Multistate Multireference Second-Order Perturbation Theory (MS-CASPT2). *J. Phys. Chem. B* **2008,** *112* (2), 405-413.
54. Maeda, S.; Ohno, K.; Morokuma, K., Updated Branching Plane for Finding Conical Intersections without Coupling Derivative Vectors. *J. Chem. Theory Comput.* **2010,** *6* (5), 1538-1545.
55. Maeda, S.; Saito, R.; Morokuma, K., Finding Minimum Structures on the Seam of Crossing in Reactions of Type A + B → X: Exploration of Nonadiabatic Ignition Pathways of Unsaturated Hydrocarbons. *J. Phys. Chem. Lett.* **2011,** *2* (8), 852-857.
56. Liu, X.-Y.; Cui, G.; Fang, W.-H., Three-state conical intersection optimization methods: development and implementation at QM/MM level. *Theor. Chem. Acc.* **2016,** *136* (1), 8.
57. Dyall, K. G.; Knut Fægri, J., *Introduction to Relativistic Quantum Chemistry*. 2007.
58. Koseki, S.; Schmidt, M. W.; Gordon, M. S., MCSCF/6-31G(d,p) calculations of one-electron spin-orbit coupling constants in diatomic molecules. *J. Phys. Chem.* **1992,** *96* (26), 10768-10772.
59. Koseki, S.; Gordon, M. S.; Schmidt, M. W.; Matsunaga, N., Main Group Effective Nuclear Charges for Spin-Orbit Calculations. *J. Phys. Chem.* **1995,** *99* (34), 12764-12772.
60. Zhang, Y.; Liu, H.; Yang, W., Free energy calculation on enzyme reactions with an efficient iterative procedure to determine minimum energy paths on a combined ab initio QM/MM potential energy surface. *J. Chem. Phys.* **2000,** *112* (8), 3483-3492.
61. Rod, T. H.; Ryde, U., Accurate QM/MM Free Energy Calculations of Enzyme Reactions: Methylation by Catechol O-Methyltransferase. *J. Chem. Theory Comput.* **2005,** *1* (6), 1240-1251.
62. Kästner, J.; Senn, H. M.; Thiel, S.; Otte, N.; Thiel, W., QM/MM Free-Energy Perturbation Compared to Thermodynamic Integration and Umbrella Sampling: Application to an Enzymatic Reaction. *J. Chem. Theory Comput.* **2006,** *2* (2), 452-461.

Chapter 2

Theoretical Study on the Rhodium-Catalyzed Hydrosilylation of C=C and C=O Double Bonds with Tertiary Silane

2.1 Introduction

In Chapter1, the importance of hydrosilylation reaction has been explained. Mechanistic aspects of the catalytic hydrosilylation reactions are often discussed in terms of the Chalk-Harrod (CH) mechanism and the modified Chalk-Harrod (mCH) mechanism (scheme 1a), both of which were originally suggested from catalytic hydrosilylations of alkenes.[1-8] In both cases, an oxidative addition reaction of hydrosilane results in Si-H bond cleavage on a transition metal catalyst [M] to afford a reactive intermediate having M-H and M-Si bonds [H-M-Si]. In the CH mechanism, a C=C bond of an alkene is firstly inserted into the M-H bond, and a subsequent reductive elimination occurs to form a Si-C bond. On the other hand, in the mCH mechanism, the C=C bond is inserted into the M-Si bond, which is followed by a reductive elimination to form a C-H bond. Although the same product is obtained in both reaction mechanisms, such mechanistic aspects are worthy of understanding reactivity, selectivity, and applicability of hydrosilylation reactions. In the alkene hydrosilylation, it has been well known that Pt-catalyzed hydrosilylation takes place via the CH mechanism[2, 5-7] while Rh-catalyzed hydrosilylation occurs via the mCH mechanism.[9-15] These were also supported from previous computational studies by Sakaki and co-workers, and

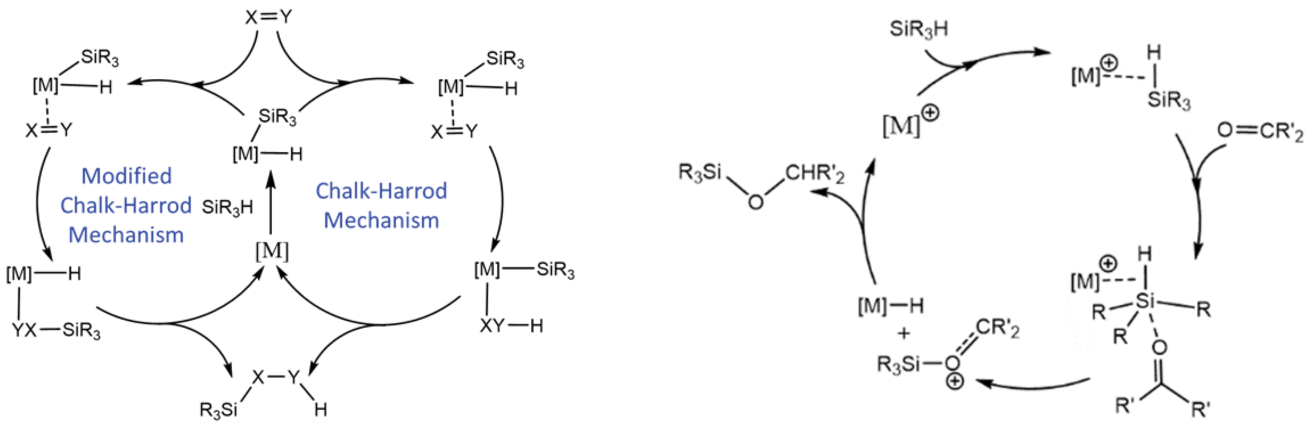

a. Chalk-Harrod (CH) and modified CH (mCH) mechanism

b. Outer-sphere mechanism

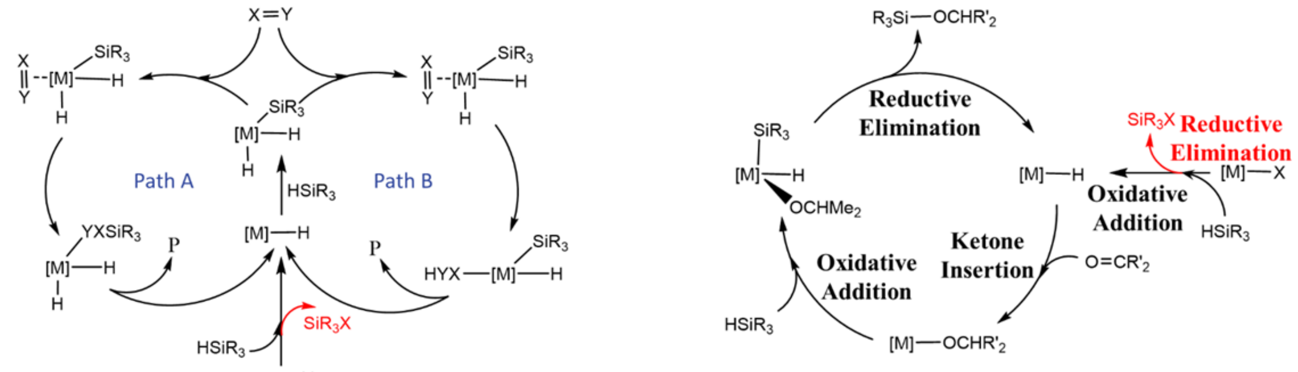

c. Double-hydride (DH) mechanism

d. Alternative Chalk-Harrod (aCH) mechanism

Scheme 1 (a) Chalk-Harrod and modified Chalk-Harrod mechanism, (b) outer-sphere mechanism, (c) double hydride mechanism, (d) alternative Chalk-Harrod mechanism. Some ligands are omitted for clarity.

they concluded that the difference in reaction mechanism of Pt- and Rh-catalyzed hydrosilylations of ethylene is excellently explained based on electronic structure and trans influence of silyl group.[16-19]

In the hydrosilylation of carbonyl compounds, several mechanisms such as Zheng-Chan mechanism[20] and Gade mechanism[21] were proposed for the hydrosilylation with primary and secondary silanes. When tertiary silanes are adopted, due to strong affinity of O atom to Si atom, it has long been believed that the mCH mechanism is only a possible reaction pathway because few catalysts were reported for the Pt-catalyzed hydrosilylation while a common Rh-complex efficiently catalyzes the hydrosilylation of carbonyl compounds (Ojima's work).[7] However, there is no direct evidence on the reaction mechanism of the Rh-catalyzed hydrosilylation of carbonyl compounds neither from experimental nor from computational studies. An alternative pathway, the outer-sphere mechanism (scheme 1b), was recently proposed from the catalytic hydrosilylation of carbonyl compounds by the cationic Ir-complex.[22-25] Of further interest from an exceptional example that we previously reported on the Pt-catalyzed amide reduction with a bifunctional hydrosilane is that the hydrosilylation of carbonyl compounds can occurs via the CH mechanism while the mCH mechanism was clearly ruled out in this case.[26] Therefore, the CH pathway is a potentially possible reaction mechanism for the hydrosilylation of carbonyl compounds. As a current consequence, there is no clear conclusion in the catalytic mechanism for the hydrosilylations of carbonyl compounds, and therefore, it is worthy of revisiting the hydrosilylation catalyzed by a common Rh-catalyst.

In this work, we theoretically investigated the Rh-catalyzed hydrosilylation of acetone or ethylene with tertiary silane to examine three proposed mechanisms, CH mechanism, mCH mechanism and outer-sphere mechanism to reveal the mechanistic aspects behind the hydrosilylation reactions of carbonyl compounds. Moreover, we proposed two new promising reaction pathways, double hydride (DH) mechanism (scheme 1c) and alternative Chalk-Harrod (aCH) mechanism (scheme 1d). The active species in the DH mechanism which has two Rh-H bonds was found to have high catalytic efficiency in Rh-catalyzed hydrosilylation of C=C and C=O double bonds. The extra Rh-H bond plays an important role in reducing energy barrier.

In the following section, details are described for the present density functional theory (DFT) calculations. In section 2.3, outer-sphere mechanism, CH, mCH, aCH, and DH mechanisms will be explained from two aspects, acetone hydrosilylation and ethylene hydrosilylation. A summary will be given in section 2.4.

2.2 Computational details

Both geometry optimization and energy calculation were carried out with DFT using the ωB97XD functional implemented in the Gaussian 09 program.[27] In our previous study, the ωB97XD functional worked reasonably well for the hydrosilylation reactions.[26] We also compared the optimized structure $[RhCl(PMe_3)_3]$ with experimental one. As shown in Table 1, the ωB97XD functional works better than other available functionals. Two kinds of basis sets, which are labeled as BS-I and BS-II were used. In BS-I set, Stuttgart/Dresden (611111/22111/411) valence basis set[28] was used for Rh where 28 core electrons were replaced by the effective core potentials (ECPs).[29] The 6-31+G* basis sets were used for P, O and Cl atoms, and the 6-31G* basis sets were employed for other atoms. In BS-II set, an f polarization function was added to the BS-I set for Rh. The 6-311+G** basis sets were used for P, Cl and O atoms, and the 6-311G** basis sets were employed for other atoms. The BS-I set was used for geometry optimization and vibrational frequency calculation, and the BS-II set, the better basis set, was employed for single-point calculations to evaluate energy changes due to the basis-sets improvement.

Table 1 Important bond distances (Å) from calculated structures using B3LYP, M06 and ωB97XD functionals as well as from the experimental structure.

	Rh-P1	*Rh-P2*	*Rh-P3*	*Rh-Cl*
B3LYP	2.251	2.341	2.351	2.453
M06	2.240	2.327	2.331	2.430
ωB97XD	2.233	2.321	2.329	2.427
Exp.[30]	2.203	2.295	2.296	2.410

The Gibbs free energy correction in solution phase was evaluated with Whiteside's scheme[31] as followings:

$$G_{solv.} = E_{PCM} + H_{gas} - E_{gas} - \left(S_{rot,gas} + S_{vib,gas} + S_{tran,solv.}\right) \cdot T \qquad (1)$$

$$S_{tran,solv.} = 11.1 + 12.5 \cdot \ln T + 12.5 \cdot \ln M_{solute} + 8.3 \cdot \ln V_{free} \qquad (2)$$

where $G_{solv.}$ is the corrected Gibbs free energy. E_{PCM} is the energy calculated in The polarizable continuum model (PCM) model.[32] H_{gas}, E_{gas}, $S_{rot,gas}$ and $S_{vib,gas}$ are enthalpy, potential energy, rotational entropy and vibrational entropy in gas phase, respectively. $S_{tran,solv.}$ is the translational entropy in the solvent which were evaluated with the method developed by Whitesides et al[31]. M_{solute} and T are the molecular mass of the solute and the temperature (room temperature was used in this work), respectively. V_{free} is the free volume of the solute in Free Volume Theory.

To avoid a computational bottle neck from a large triphenylphosphine moiety, tris-

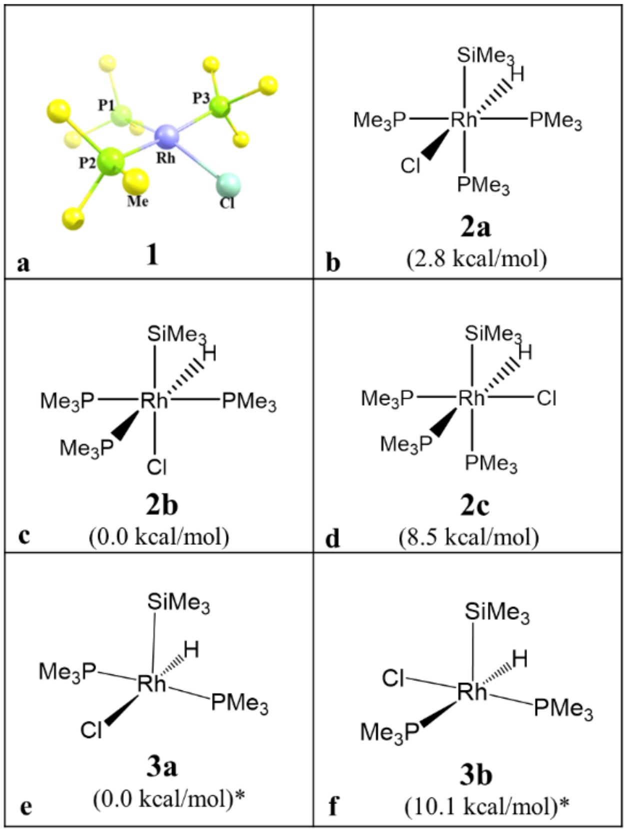

Figure 1 (a) tris-(trimethylphosphine)rhodium(I)chloride [RhCl(PMe$_3$)$_3$], (b-d) three possible isomers after the oxidative addition reaction of hydrosilane, (e-f) structures of **3a** and **3b**. Relative stability in free energy is shown in parenthesis (with "*" means relative to **3a**, otherwise relative to **2b**).

(trimethylphosphine)rhodium(I)chloride [$RhCl(PMe_3)_3$] (**1**) was adopted as a model catalyst for tris-(triphenylphosphine)rhodium(I)chloride [$RhCl(PPh_3)_3$] (Me = methyl, Ph = phenyl) as shown in Figure 1, a. Trimethylhydrosilane ($HSiMe_3$), acetone (Me_2CO), and ethylene ($CH_2=CH_2$) were considered as substrates in this work.

2.3 Results and discussion

2.3.1 Oxidative addition of hydrosilane to the catalyst

The first step of the catalytic hydrosilylation is an oxidative addition of $HSiMe_3$ to **1**. Based on our computational model, three possible isomers (**2a**-**2c**) can be led as a result of the oxidative addition reaction, as shown in Figure 1(b-d). A substrate $HSiMe_3$ approaches the catalyst to form precursor complexes **PC1** and **PC2**, from which **2a** and **2b** are formed through transition states **tsPC1-2a** ($\Delta G^{\ddagger}$=10.2 kcal/mol) and **tsPC2-2b** ($\Delta G^{\ddagger}$=10.0 kcal/mol), respectively. Figure 2 shows these complexes' structural information. Among these isomers, **2b** was found to be the most stable, and **2a** was obtained as being slightly less stable by 2.8 kcal/mol than **2b**, while **2c** was computed to be considerably higher in energy by 8.5 kcal/mol than **2b**. The stability of **2a** and **2b** relative to **2c** is explained by the order of trans-influence: $SiMe_3^-$ > H^- > PMe_3 > Cl^-. In **2a** and **2b**, the Cl^- ligand takes the position trans to H^- and $SiMe_3^-$, respectively. In **2c**, PMe_3 ligands are located at trans positions to either H^- or $SiMe_3^-$. As a consequence, **2c** becomes relatively unstable because of strong σ-donating interaction from PMe_3 ligands. These results agreed well with the previous theoretical work by Sakaki.[17] A strong and weak combination of trans-influence stabilizes the complex more than a strong and strong combination. Therefore, only **2a** and **2b** were considered as possible candidates for the reaction intermediates of each reaction mechanism that we discussed in the latter subsections.

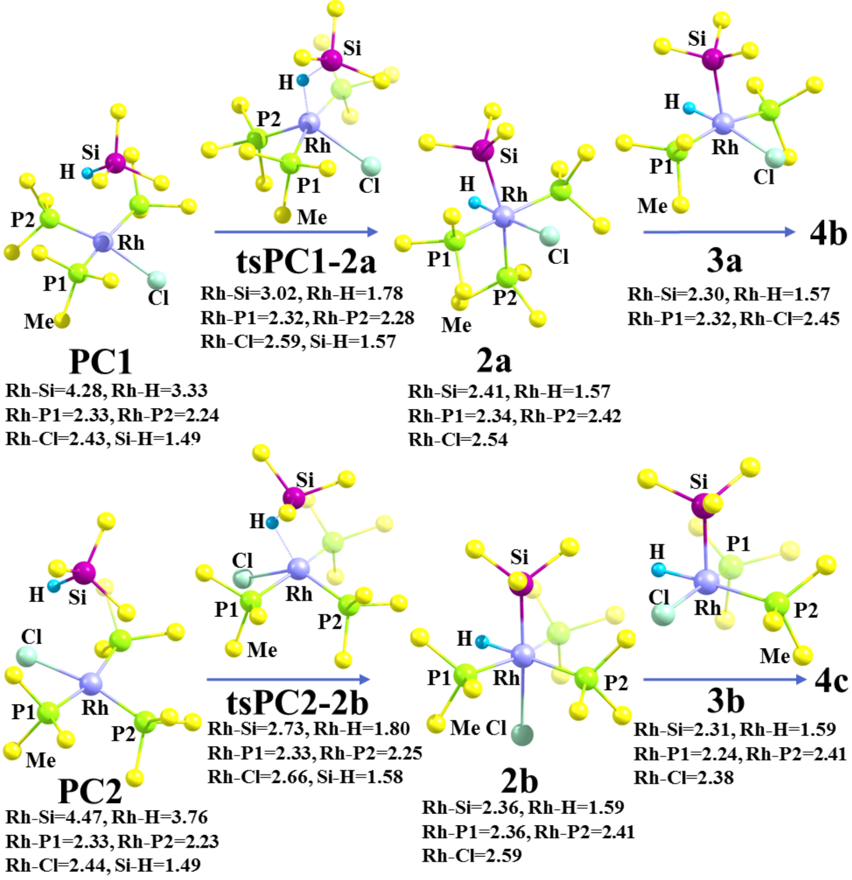

Figure 2 Optimized Geometries of **PC1**, **PC2**, **tsPC1-2a**, **tsPC2-2b**, **2a**, **2b**, **3a** and **3b**. Important bond lengths are shown in Å.

2.3.2 Formation of active species

Because the structures of both **2a** and **2b** are saturated, one phosphine ligand would be substituted by acetone or ethylene to proceed the hydrosilylation reaction. This process will generate different isomers which can be the candidates of active species in different mechanisms. Basing on the relative stabilities and ligand positions, we selected reasonable active species for each mechanism that are listed in Figure 3.

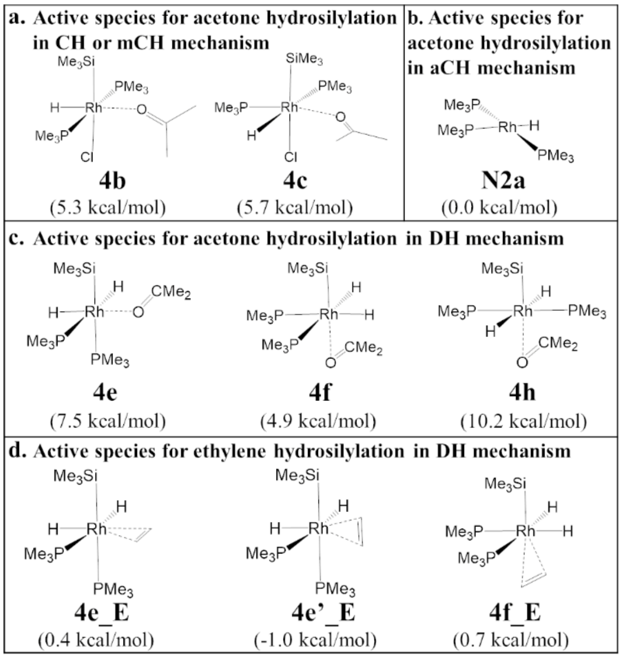

a. Active species for acetone hydrosilylation in CH or mCH mechanism

b. Active species for acetone hydrosilylation in aCH mechanism

c. Active species for acetone hydrosilylation in DH mechanism

d. Active species for ethylene hydrosilylation in DH mechanism

Figure 3 (a) Two active species for the CH and the mCH mechanisms in acetone hydrosilylation. Their coordination modes are also given. (b) The active species for the aCH mechanism. (c) Three active species for the DH mechanism in acetone hydrosilylation. (d) Three active species for the DH mechanism in ethylene hydrosilylation. Relative stability in free energy is shown in parenthesis.

2.3.3 Chalk-Harrod (CH) mechanism

a) Acetone hydrosilylation

In this subsection, we discuss the CH mechanism of acetone hydrosilylation in which **4c** is taken as an active species of the catalytic cycle. Note that the C=O bond insertion into the Rh-H bond is inaccessible in **4b** because the H^- is at the position trans to the acetone. In addition, the C=O bond insertion into the Rh-H bond in **4a** or **4d** did not form any stable intermediates in our calculation. This is due to the strong trans-influence of the silyl group; an isopropoxy group derived from the C=O bond insertion is less likely to be formed at the position trans to the silyl group.

Computed energy profile that starts with **4c** is summarized in Figure 4, The energy of **4c** is taken to be zero since this state is the active species in the catalytic cycle. The C=O bond insertion into the Rh-H bond of **4c** occurs to afford an alkoxide complex **5cC** as shown in Figure 4. In **5cC**, the C-H bond is 1.18Å, which is slightly longer than common aliphatic C-H bonds, and the Rh-H distance is 2.04 Å. This result suggests that **5cC** involves a medium agostic interaction between the Rh center and the C-H bond. The formation of **5cC** is considerably endothermic by 20.2 kcal/mol. Because the geometry of the associated transition state **ts4c-5cC** is very close to that of **5cC** except for the C-H and the Rh-H bonds, the potential energies are very close to each other, and as a result, free energy corrections changed the energy order of **ts4c-5cC** and **5cC**. **5cC** is easily isomerized to **6cC** in which the agostic Rh-H bond is broken and the Cl moves to the position trans to PMe_3, as shown in Figure 4. In **6cC**, the strong trans-influence from the silyl group is avoided. Therefore, **6cC** is more stable in energy by 16.4 kcal/mol than **5cC** and is a stable intermediate in the CH mechanism.

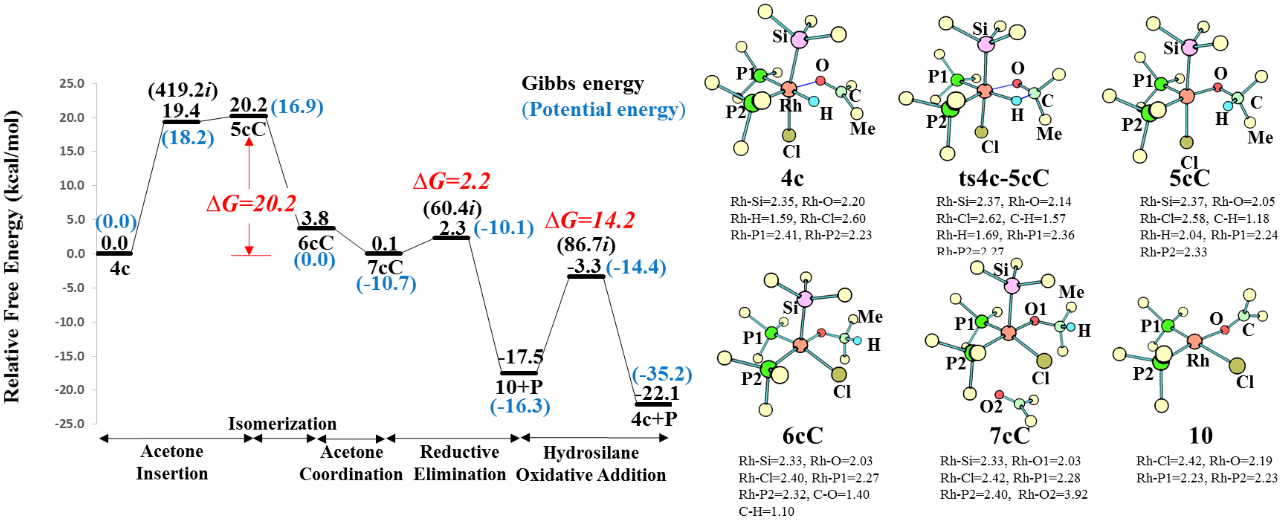

Figure 4 (left) Gibbs free energy profile for the CH mechanism in acetone hydrosilylation. (right) Important intermediates and transition state in the CH mechanism starting with the C=O bond insertion into Rh-H bond of **4c**. Important bond lengths are shown in Å.

Now that **6cC** has a vacant site, another acetone can approach to the Rh center to afford a coordinatively saturated intermediate. After acetone coordination, a six-coordinate complex **7cC** is slightly more stable than **6cC** by 3.7 kcal/mol. Interestingly, a subsequent reductive elimination of the Si-O bond easily occurs with the associated activation barrier of 2.2 kcal/mol, to result in a product with an acetone complex **10**. This small energy barrier is due to the strong affinity of Si and O atom (see Figure 5). Finally, oxidative addition reaction of $HSiMe_3$ occurs with the complex **10** to regenerate active species **4c** to close the catalytic cycle. In consequence, the acetone insertion step is to be the rate-determining step in the CH mechanism, for which the associated activation energy was estimated to be 20.2 kcal/mol.

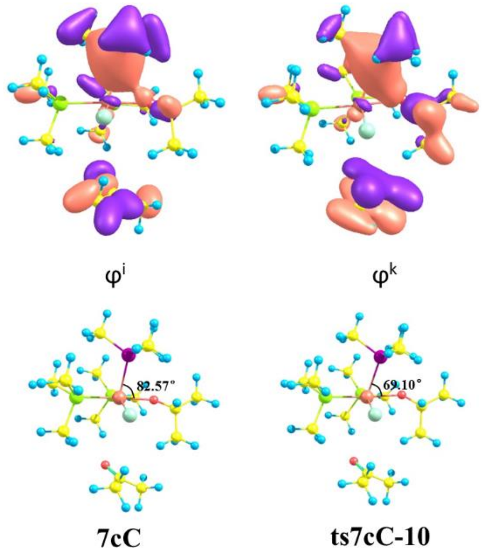

Figure 5 Interactions between Si and O in **7cC** (φ^i), **ts7cC-10** (φ^k).

b) Ethylene hydrosilylation

Sakaki's work has discussed the ethylene hydrosilylation of CH and mCH mechanisms in details. The similar results were gotten in our calculation. The mechanism and the structural changes in the course of the reaction have been well investigated in Sakaki's work,[17] we will just show the energy profiles in Figure 6 which shows similar energy change tendency as they have reported. The Si-C reductive elimination reaction is the rate-determining step with the energy barrier of 21.9 kcal/mol. That contrasts to the Rh-catalyzed acetone hydrosilylation in which only a small activation energy 2.2 kcal/mol is needed in Si-O reductive elimination reaction.

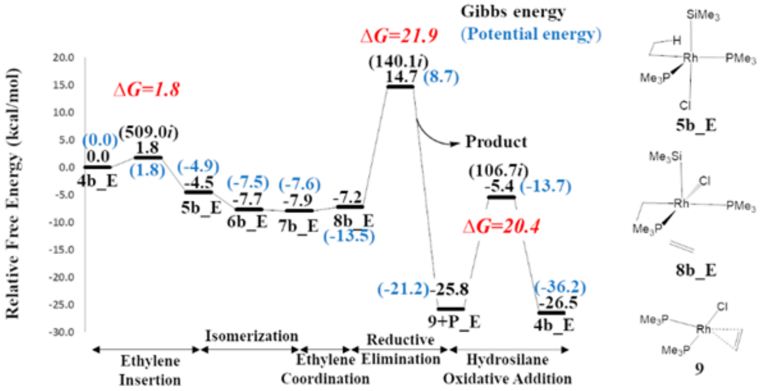

Figure 6 Gibbs free energy profile for the CH mechanism in ethylene hydrosilylation.

2.3.4 Modified Chalk-Harrod (mCH) mechanism

a) Acetone hydrosilylation

Modified Chalk-Harrod (mCH) pathway of acetone hydrosilylation is started from the C=O bond insertion into the Rh-Si bond of **4b** or **4c**. The rate-determining step in the mCH mechanism is in the C=O bond insertion into the Rh-Si bond with the associated activation energy of 43.4-45.8 kcal/mol, which is by 24.0-26.4 kcal/mol higher in energy than that in the CH mechanism (See Figure 7 and Figure 8). The high energy barrier implies this mechanism is less likely to occur. In contrast, mCH pathway of ethylene is favorable since the energy barrier is only 11.2 kcal/mol. Here we just focus on the interesting problem why is the Rh-catalyzed hydrosilylation of acetone difficult to be taken place through mCH mechanism while it is easy for ethylene? This can be attributed to the back donation interaction. In the case of alkenes, the electrons in d_π orbital move to the π anti-bonding orbital of ethylene, forming π backbonding (Figure 9 φ^a). However, in the case of acetone, only lone pair electrons are coordinated with Rh center (Figure 9 φ^b) and there is no interaction of Rh d_π orbital with the π anti-bonding orbital of acetone (Figure 9 φ^c). Thus, the π bond of ethylene is nearly broken in the precursor complex before the insertion into the Rh-Si bond while the π bond breaking in acetone is finished in the transition state of the insertion into the Rh-Si bond. Therefore, this step has to break two bonds, Rh-O and Rh-Si, to make two bonds, Rh-C and Si-O.

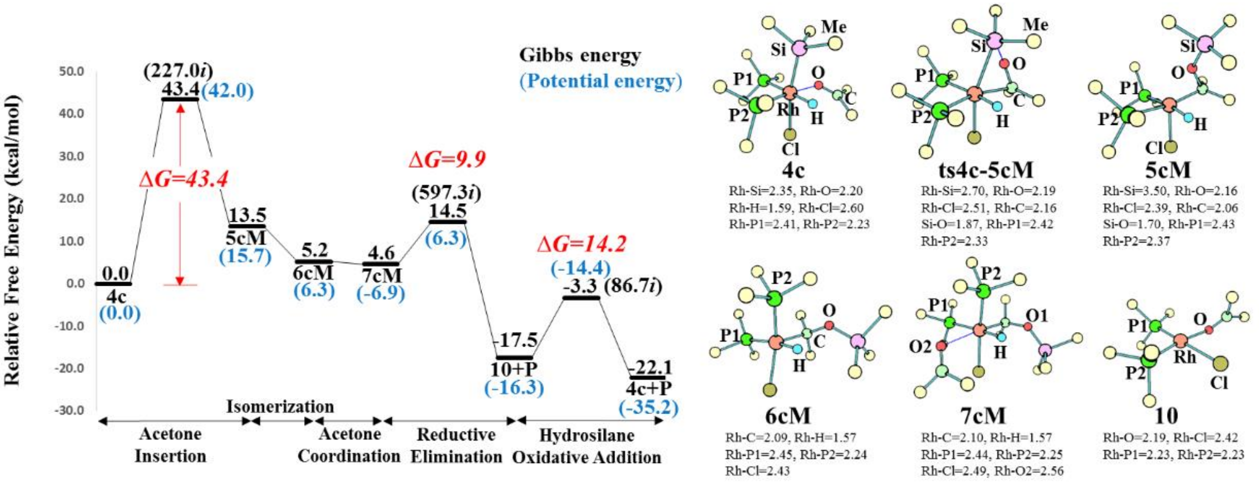

Figure 7 (left) Gibbs free energy profile for the mCH mechanism in acetone hydrosilylation (**4c** pathway). (right) Important intermediates and transition state in the **4c** pathway. Important bond lengths are shown in Å.

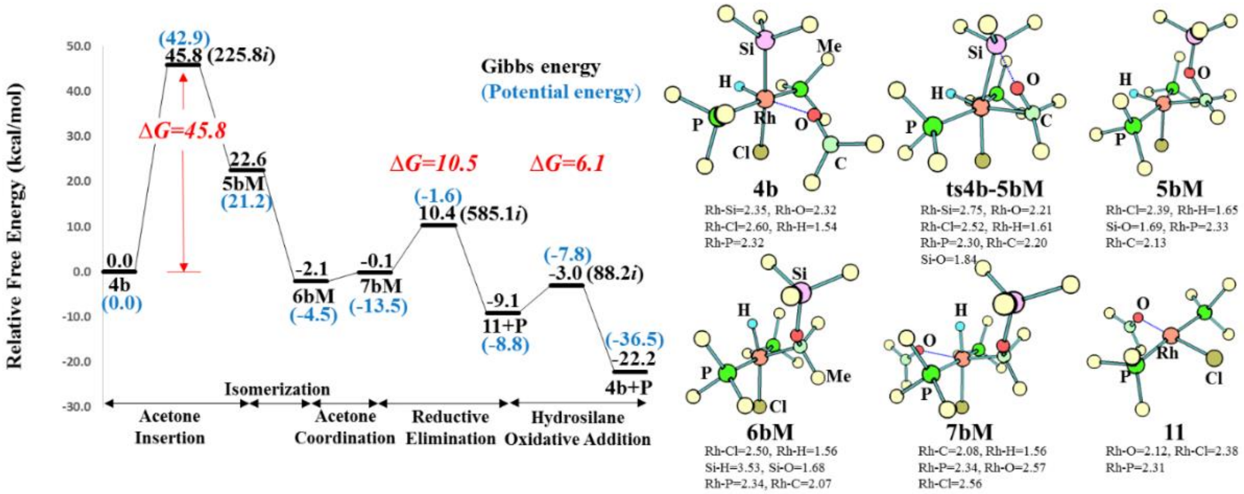

Figure 8 (left) Gibbs free energy profile for the mCH mechanism in acetone hydrosilylation (**4b** pathway). (right) Important intermediates and transition state in the **4b** pathway. Important bond lengths are shown in Å.

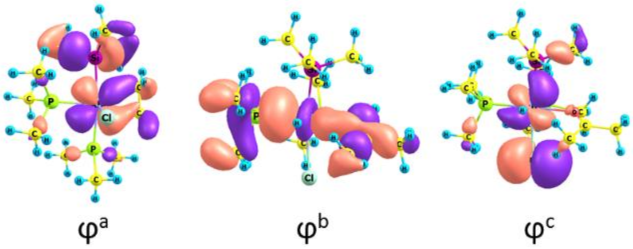
φ^a φ^b φ^c

Figure 9 Important molecular orbitals of **4a'_E** (φ^a) and **4c** (φ^b and φ^c)

b) Ethylene hydrosilylation

Because Sakaki's work[17] has already presented all the geometry changes along the mCH pathway starting from the structure **4a'_E**, **4b'_E** or **4c'_E**, we just discuss the calculated free energy profile for the **4a'_E** pathway as the example since the activation energy of the rate-determining step is the smallest of the three pathways. Our results of the CH and mCH pathways in catalytic cycles of Rh-catalyzed alkene hydrosilylation are quite consistent with those reported in Sakaki's work. Figure 10 summarizes the energy profile of the **4a'_E** pathway. The calculated activation energy of the three steps, ethylene insertion, reductive elimination of product, and oxidative addition of hydrosilane distribute 8.8-11.2 kcal/mol. Among them, the rate-determining step is the hydrosilane oxidative addition whose energy barrier was calculated to be 11.2 kcal/mol. In the **4c'_E** pathway, the rate-determining step is also the hydrosilane oxidative addition with the energy barrier of 15.4 kcal/mol. In the **4b'_E** pathway, the rate-determining step is ethylene insertion into Rh-Si bond and the activation energy barrier is 23.5 kcal/mol which is just 3.1 kcal/mol higher than hydrosilane addition.

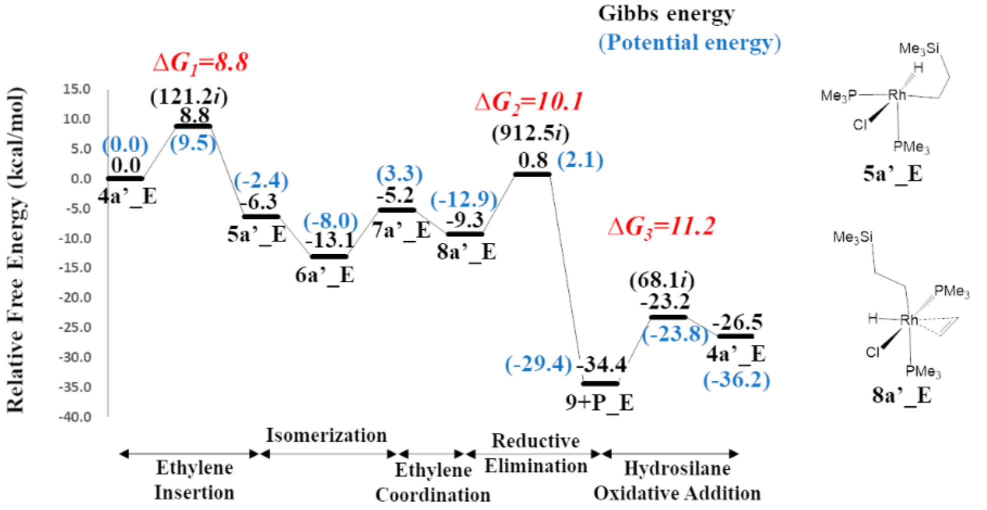

Figure 10 Gibbs free energy profile for the mCH mechanism in ethylene hydrosilylation (**4a'_E** pathway).

2.3.5 Alternative Chalk-Harrod (aCH) mechanism

As we have mentioned, there is a possibility that the active species **N2a** is formed and opens the aCH channel. The optimized structures of the important intermediates are summarized in Figure 11 (upper and lower for acetone and ethylene hydrosilylation, respectively).

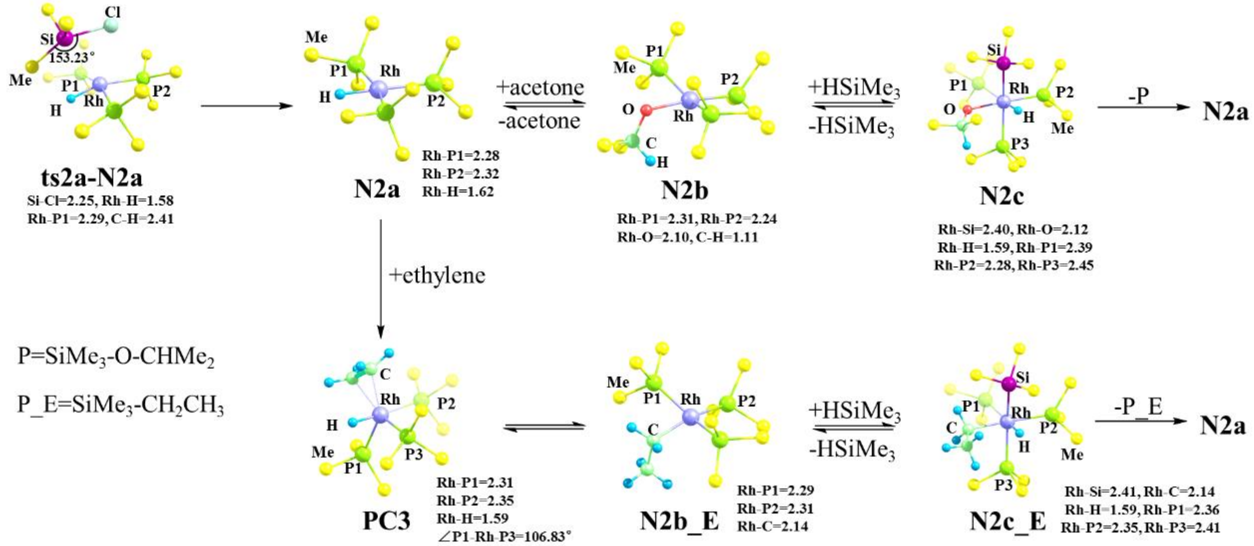

Figure 11 Optimized structures of intermediates in the aCH mechanism (top: acetone cycle; bottom: ethylene cycle). Important bond lengths are also shown (Å). "P" and "P_E" stand for product states of acetone hydrosilylatoion ($SiMe_3$-O-$CHMe_2$) and ethylene hydrosilylation ($SiMe_3$-O-CH_2CH_3), respectively.

Figure 12(a) and (b) shows free energy profiles for acetone and ethylene hydrosilylation, respectively. As described later in detail, the rate-determining steps in the aCH pathway for acetone hydrosilylation is the acetone insertion step (20.9 kcal/mol). Considering the results of the CH pathway (20.2 kcal/mol for acetone insertion into the Rh-H bond), the aCH pathway is competitive to the CH pathway. For ethylene hydrosilylation, the activation energy of the rate-determining step (the Si-C reductive elimination step) was calculated to be 24.1 kcal/mol. This barrier is larger than that in the mCH mechanism (11.2 kcal/mol, see Figure 10), while it is comparable with that of the CH mechanism (21.9 kcal/mol, see Figure 6). It suggests that when the CH mechanism is applicable (such as Pt catalyzed hydrosilylation of alkenes [16, 18]), we should also consider aCH mechanism as a possible alternative pathway.

(a) Acetone hydrosilylation

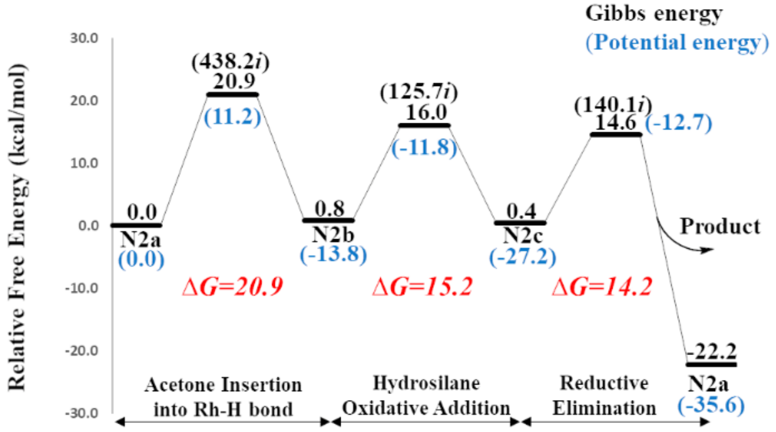

(b) Ethylene hydrosilylation

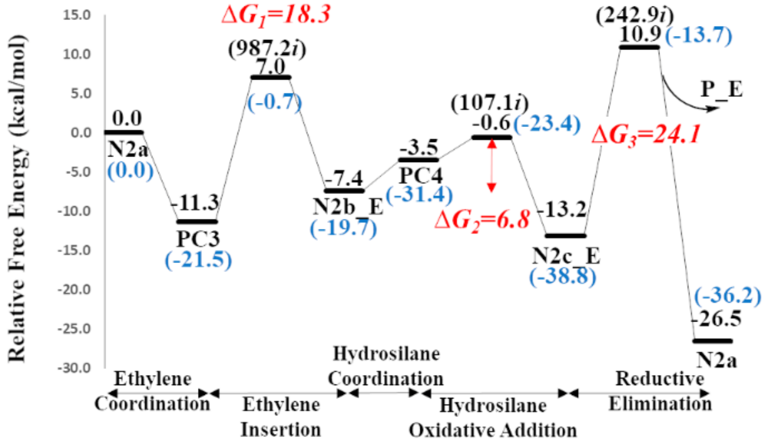

Figure 12 (a) Gibbs free energy profile for aCH mechanism in acetone hydrosilylation. (b) Gibbs free energy profile for aCH mechanism in ethylene hydrosilylation.

a) Active species formation for CH and aCH pathway

To enter the catalytic cycles of the CH mechanism and the alternative CH mechanism, the initial steps are the formation of active species **4c** and **N2a**. The energy barrier to form **4c** is lower than **N2a** by around 18 kcal/mol while **N2a** is more stable than **4c** by 5.7 kcal/mol (See Figure 13). A larger activation energy is needed to form **N2a** due to the distortion of the $SiMe_3Cl$ group. This result is under the condition of room temperature. If heating is adopted in the experiment, **N2a** can be formed in an easier way which makes the alternative CH mechanism more favorable because

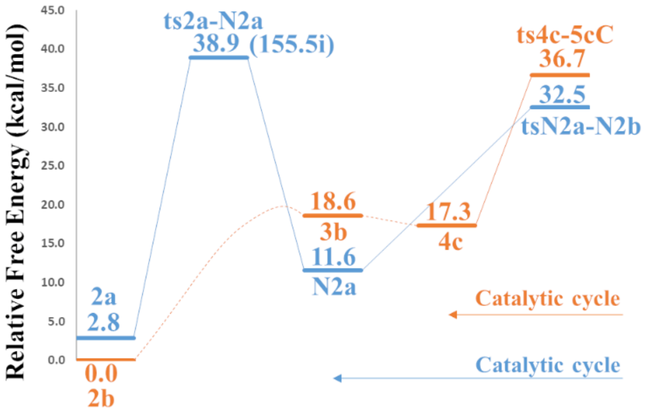

Figure 13 Energy profiles for the formation of **4c** and **N2a**.

4c is thermodynamically unstable.

b) Acetone hydrosilylation

In case of acetone, the free energy profile along the reaction issummarized in Figure 12a. The C=O bond insertion into the Rh-H bond in **N2a** occurs with the moderate activation energy (20.9 kcal/mol) to form a four-coordinate methoxy complex **N2b**, which is slightly endothermic by 0.8 kcal/mol. Although we tried to find a precursor complex before the C=O insertion, no stable complex was obtained. Compared with the CH mechanism, **N2a** is more stable than **3b** by 7.0 kcal/mol, which suggests that the aCH mechanism is thermodynamically favorable. However, the energy barrier to form **N2a** (38.9 kcal/mol) is larger than to form **4c** (18.6 kcal/mol) suggesting that to enter CH mechanism is kinetically favorable at high temperature (see Figure13 for the free energy profile of the active species formation in the CH and aCH mechanisms.). The activation free energies of acetone insertion into the Rh-H bond in the CH and aCH mechanisms are 19.4 kcal/mol (Figure 4) and 20.9 kcal/mol (Figure 12a), respectively. With potential energy, the activation energy was 11.2 kcal/mol for the aCH mechanism. The relatively large change (11.2 kcal/mol in potential energy to 20.9 kcal/mol in Gibbs free energy) is due to the rotation enthalpy correction (7.0 kcal/mol). Next, another $HSiMe_3$ is oxidatively added to **N2b** with the associated activation energy of 15.2 kcal/mol, which results in a six-coordinate complex **N2c**. The Si-O reductive elimination regenerates the active complex **N2a**. The rate-determining step in this mechanism is the C=O bond insertion into the Rh-H bond of **N2a**, and the activation energy was estimated to be 20.9 kcal/mol. This is only 0.7 kcal/mol larger in activation energy in comparison with the traditional CH mechanism. Therefore, the aCH pathway would be equally important to the traditional CH mechanism, particularly at high temperature where more N2a intermediate would be generated.

c) Ethylene hydrosilylation

For the case of ethylene, the changes in free energy are summarized in Figure 12b (bottom). Before the C=C bond insertion into the Rh-H bond, ethylene is coordinated to **N2a** to form a more stable precursor complex **PC3** by 11.3 kcal/mol. After this step, the geometry changes in the ethylene case are similar to that of the acetone case. The rate-determining step is same as that in the CH pathway, which is Si-C reductive elimination reaction. Besides, the energy barrier in this step (24.1 kcal/mol) is also very near to the value in the CH pathway (21.9 kcal/mol)

The ethylene insertion into the Rh-H bond needs an activation energy of 18.3 kcal/mol, a similar value to the acetone insertion into the Rh-H bond in the CH (19.4 kal/mol) or aCH (20.9 kcal/mol) pathways. After the formation of **N2b_E**, another local minima **PC4** is found along the potential energy surface, which is yielded by a hydrosilane coordination to the Rh center. In the step of hydrosilane addition, a very small energy barrier is needed in the case of ethylene (6.8 kcal/mol) while a relatively larger energy barrier (15.2 kcal/mol) is required in the case of acetone. This is because we evaluate the free energy difference between **N2b_E** and **tsN2b_E-N2c_E** as the activation energy, where the potential energy of the former complex is higher than the later one. In the final step, Si-C bond reductive elimination reaction needs an energy barrier of 24.1 kcal/mol, which is 9.9 kcal/mol higher than the Si-O bond elimination in the acetone case.

2.3.6 Double hydride (DH) mechanism

In this last subsection, another newly proposed mechanism, DH mechanism, will be discussed. The active species, **4e**, **4f**, **4h**, for acetone case and **4e_E**, **4e'_E**, **4f_E**, for the ethylene case, are shown in Figure 3(c and d).

a) Active species formation for DH pathway

For the DH pathway, after the formation of **3e** and **3h**, the acetone or the ethylene will be coordinated to the Rh center. We only show the stable candidates in the main body. Actually, we have considered all the possible complexes which are shown in Figure 14 and Figure 15. The energy of these complexes is summarized in Table 2. From the energy data we can easily found that **4g**, **4g_E** and **4h_E** are less stable than the other candidates, thus they can be reasonably

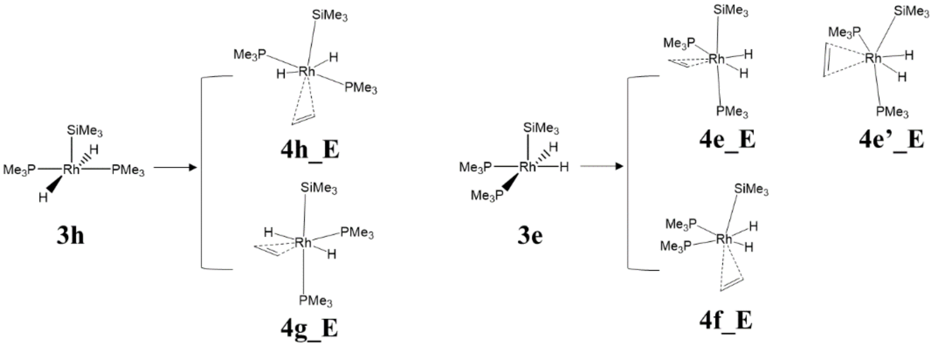

Figure 14 Possible isomers after the ethylene coordination to **3h** (left) and **3e** (right).

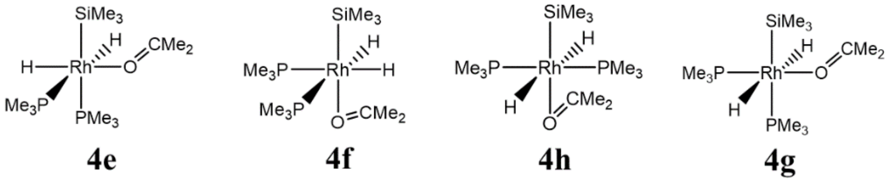

Figure 15 Possible isomers after the acetone coordination to **3h** and **3e**.

excluded from the consideration.

Table 2 Relative energies for possible active species in DH mechanism (left: ethylene cycle; right: acetone cycle).

	Relative Free Energy/kcal·mol^{-1}
4e_E	0.0
4e'_E	-1.4
4f_E	0.3
4h_E	8.8
4g_E	13.4

	Relative Free Energy/kcal·mol^{-1}
4e	0.0
4f	-2.6
4h	2.7
4g	13.6

b) Acetone hydrosilylation

Among **4e**, **4f**, and **4h**, the C=O double bond insertion into Rh-Si bond could only happen in **4e** pathway because acetone is in trans position of silyl group in other two structures. However, unlike other reaction pathways, the acetone insertion into Rh-Si bond in **4e** needs high activation energy ($\Delta G^{\ddagger}$=33.7 kcal/mol). This situation is similar to that in the mCH mechanism in which calculated activation energy for the C=O insertion into the Rh-Si bond was calculated to be 43.4 and 45.8 kcal/mol for the **4e** and **4b** pathways, respectively. As a consequence, we can only consider the C=O bond insertion into the Rh-H bond.

Taking the **4f** pathway as the example, free energy profile is summarized in Figure 16. Those for the **4e** and **4h** pathways are shown in Figure 17. Obviously, the rate-determining step is the C=O bond insertion into the Rh-H bond with a moderate energy barrier of 13.6 kcal/mol. The energy of the transition state **ts4f-5f** is close to that of the **5f** state. This is because the geometry of the **ts4f-5f** state is similar to that of the **5f** state (except for the C-H2 and Rh-H2 bond lengths) as shown in Figure 16.

As for the **5f** structure, several features should be mentioned; remaining Rh-H2 bond (1.77 Å), relatively long C-H2 bond (1.31 Å) and near-flat carbonyl moiety (O, two methyl groups, and

C in acetone part). We found C=O π* bond is not occupied, suggesting that the C=O π bond is not totally broken in the insertion reaction. The Rh-H2 interaction still remains as agostic interaction. Thus, the energy barrier in the DH mechanism is much lower than those in the CH (20.2 kcal/mol) or aCH (20.9 kcal/mol) mechanisms. In the case where the active species are **4e** and **4h**, this step causes activation energy of 17.1 kcal/mol and 12.0 kcal/mol to form **5e** and **5h** (see Figure 17), respectively.

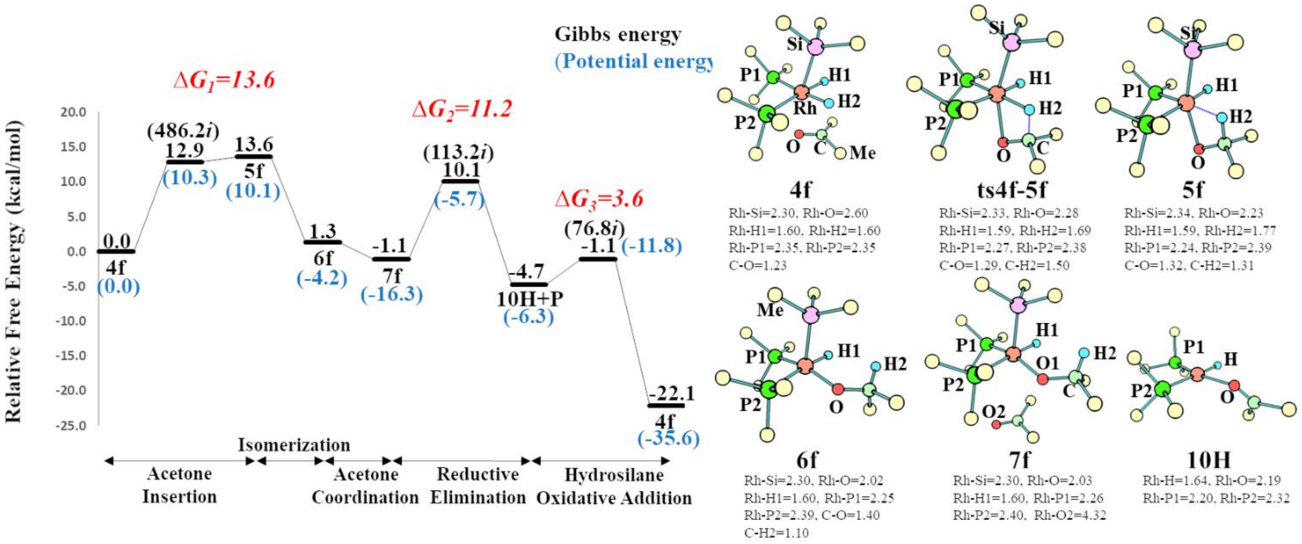

Figure 16 (left) Gibbs free energy profile for the DH mechanism in acetone hydrosilylation (**4f** pathway), (right) Importantintermediates and transition state in the **4f** pathway. Important bond lengths are shown in Å.

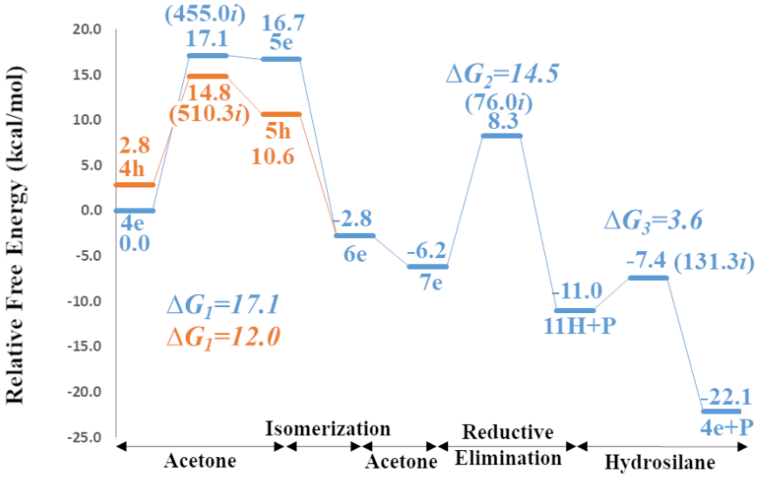

Figure 17 Gibbs free energy profile for DH mechanism in acetone hydrosilylation (blue: 4e pathway; orange: 4h pathway).

In the CH pathway, even though **4a** and **4d** are structural analogous to **4f**, acetone insertion into Rh-H bond was proved to be impossible due to the unstability of the insertion products as explained in subsection 2.3.3. So here comes a question why insertion reaction becomes possible when there are two hydride ligands. As shown in Figure 18, Silyl group was found not in the absolutely axial position when there is a hydride ligand at the cis position to the Rh atom. The Rh-Si-H1 angles are 74.4, 75.3, and 76.6 degrees in **4f**, **ts4f-5s**, and **5f**, respectively. This is due to a weak bonding interaction between Si and H1 in occupied orbital through the insertion step; φ^d of **4f**, φ^e of **ts4f-5f**, and φ^f of **5f**. Hereafter, the interaction is called as Si-H cis interaction. If there is only one H ligand, the C-H bond formation breaks the Si-H interaction in the course of the reaction.

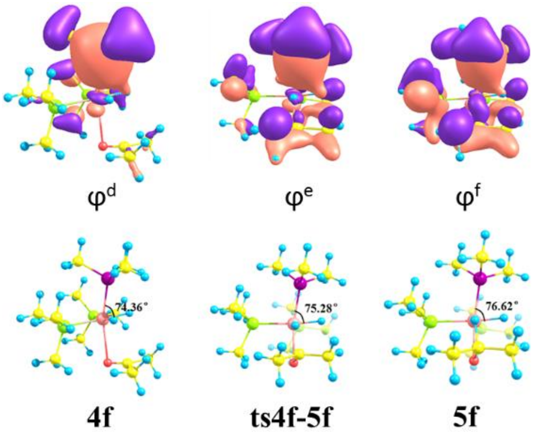

Figure 18 Orbital interactions between silyl group and hydride in **4f** (φ^d), **ts4f-5f** (φ^e) and **5f** (φ^f). The Si-Rh-H2 angles are also given.

Once broken, the silyl group will move back to the axial position and consequently cause a stronger trans-influence. If there are two H ligands, acetone insertion reaction can only break one Rh-H bond. The remaining H ligand still have interaction with the silyl group which weakens the trans-influence to the isopropoxy group.

Since the isopropoxy group is in the trans position of the silyl group, the isomerization is easily taken place to form **6f** (Figure 16) in which the isopropoxy group moves to the position trans to PMe_3 group to avoid trans position to the silyl group. During the isomerization, agostic interaction between Rh and isopropoxy group is broken. The C=O double bond (1.32 Å) becomes more like a single bond (1.40 Å). **6f** is 12.3 kcal/mol more stable than **5f** on account of avoiding stronger trans-influence. The vacant site in **6f** will be occupied by another acetone to form a coordinately saturated complex **7f** which is slightly more stable than **6f** by 2.4 kcal/mol. Next, the reductive elimination follows with an energy barrier of 11.2 kal/mol (see Figure 16), and the Si-O bond is formed. Interestingly, in **4e** and **4h** pathways (see Figure 17), the isomerization of **5e** and **5h** both lead to the **6e** complex (see Figure 19). As a consequence, the two pathways share Si-O reductive elimination reaction with activation energy of 14.5 kcal/mol, leading to the formation of **11H** (Figure 19). **11H**, the isomer of **10H**, has two PMe_3 in trans position of each other and H in trans position to acetone. Thus, **11H** is more stable than **10H** by 3.7 kcal/mol. Finally, a hydrosilane is easily added to **10H** (or **11H**) to reform **4f** (or **4e** and **4h**) taking the activation energy of 3.6 kcal/mol (3.6 kcal/mol for **4e** and 9.4 kcal/mol for **4h**, respectively).

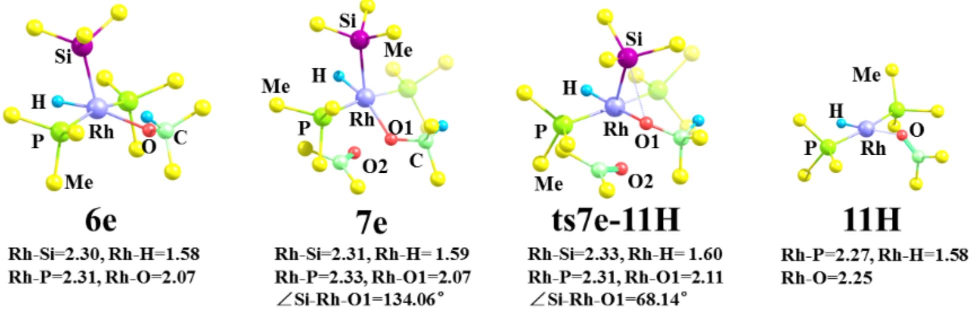

6e
Rh-Si=2.30, Rh-H=1.58
Rh-P=2.31, Rh-O=2.07

7e
Rh-Si=2.31, Rh-H= 1.59
Rh-P=2.33, Rh-O1=2.07
∠Si-Rh-O1=134.06°

ts7e-11H
Rh-Si=2.33, Rh-H= 1.60
Rh-P=2.31, Rh-O1=2.11
∠Si-Rh-O1=68.14°

11H
Rh-P=2.27, Rh-H=1.58
Rh-O=2.25

Figure 19 Optimized geometries of **6e**, **7e**, **ts7e-11H** and **11H**. Important bond lengths are shown in Å.

c) Ethylene hydorsilylation

We also studied the DH mechanism in the ethylene hydrosilylation. As shown in Figure 3d, three candidates for the active species were considered as mentioned in subsection 2.3.3, that are **4e_E**, **4e'_E** and **4f_E**. In the ethylene insertion to these species, the C=C insertion into the Rh-H bond would happen to **4e_E** and **4f_E** while the insertion into the Rh-Si bond does for **4e'_E**. The orientation of ethylene in **4e_E** and **4e'_E** allows π orbital of ethylene to interact H and Si atoms, respectively. In **4f_E**, ethylene is in trans position to the Si atom and would only be accessible to the H atom. In the below, we define the reaction pathways which starts with **4e_E**, **4e'_E**, and **4f_E** states as 4e_E, 4e'_E, and 4f_E pathways, respectively.

In the DH mechanism, the activation free energy for the ethylene insertion into Rh-Si bond is calculated to be 28.5 kcal/mol (4e'_E pathway), which is much larger than that found in the mCH mechanism (8.8 kcal/mol, see Figure 10). The low activation energy in the mCH pathway is explained by π back-donation in a precursor complex (see φ^a in the Figure 20). In the 4e'_E pathway of the DH mechanism, HOMO shows that this interaction still exists (see φ^g in Figure 20). However, the H ligand at the trans position to ethylene has non-negligible interaction with the silyl group (see φ^h in Figure 20). The ethylene insertion into the Rh-Si bond has to break such interactions. Also, H ligand has a stronger trans-influence than the phosphine ligand, which aggravates the instability of the transition state in the 4e'_E pathway.

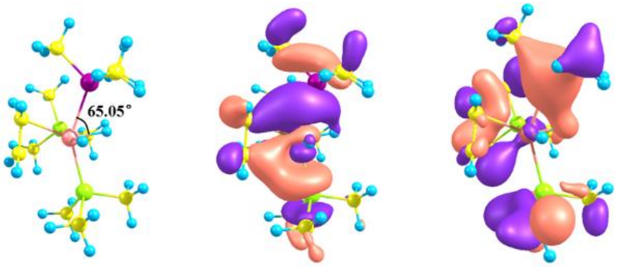

4e'_E φ^g φ^h

Figure 20 The φ^g orbital shows π back-donation from Rh to the silyl group in **4e'_E**. The φ^h orbital shows Si-H interaction in **4e'_E**.

Because the 4e_E and 4f_E pathways have similar geometries each other, the explanation is only given for the 4f_E pathway. Energy profiles are summarized in Figure 21. The C=C double bond insertion into the Rh-H bond in **4f_E** requires a moderate activation energy of 7.9 kcal/mol

(8.2 kcal/mol for **4e_E**) to yield **5f_E** (Figure 21). The **ts4f_E-5f_E** and **5f_E** states are close in energy due to the closeness in the structure; newly formed Rh-C2 bond is 2.21 and 2.15 Å in **ts4f_E-5f_E** and **5f_E**, respectively, and the C1-H1 bond is 1.51 and 1.22 Å in **ts4f_E-5f_E** and **5f_E**, respectively. A slightly long C1-H1 bond length (1.22 Å) in **5f_E** indicates the existence of agostic interaction. Because of the strong trans influence of the silyl group, the ethyl group in **5f_E** is easily isomerized to the position trans to PMe_3 group, leading to the complex **6f_E** which is by 10.7 kcal/mol more stable than **5f_E** (see Figure 21). Since then, the ethyl group is rotated along the Rh-C bond to form complex **7f_E**, a more stable intermediate comparing to **6f_E** by 3.4 kcal/mol. The vacant site in **7f_E** can be occupied by an ethylene to form **8f_E** which is just slightly unstable than **7f_E** by 2.3 kcal/mol because ethylene is taken position trans to silyl group. The next Si-C bond reductive elimination of **8f_E** is the rate-determining step in this catalytic cycle and takes 12.7 kcal/mol activation energy, leading to the product **P_E** and intermediate **10H_E**. The reaction from **8f_E** to **10H_E** is exothermic by 10.4 kcal/mol. In the DH mechanism, the Si-C reductive elimination reaction takes a lower energy barrier ($\Delta G^{\ddagger}$=12.7 kcal/mol) than that in the CH mechanism ($\Delta G^{\ddagger}$=21.9 kcal/mol). This is because the neighbor ligand of the ethyl group is hydride while that in the CH pathway is PMe_3. Hydride has much smaller steric effect so that the ethyl group can rotate to the position where the C-H bond in the ethyl group can have agostic interaction in the transition state. In this way, the activation energy for the Si-C reductive elimination in the 4f_E pathway is reduced. Finally, a hydrosilane is added to **10H_E** nearly without energy barrier to reform **4f_E**. It is reasonable if there is almost no energy barrier in this step, because this is an exothermic reaction and the Si-H bond is quite active. Besides, we scanned the Rh-Si bond from the reactant to the product, the resulting energy curve is monotonically decreased (see Figure 22).

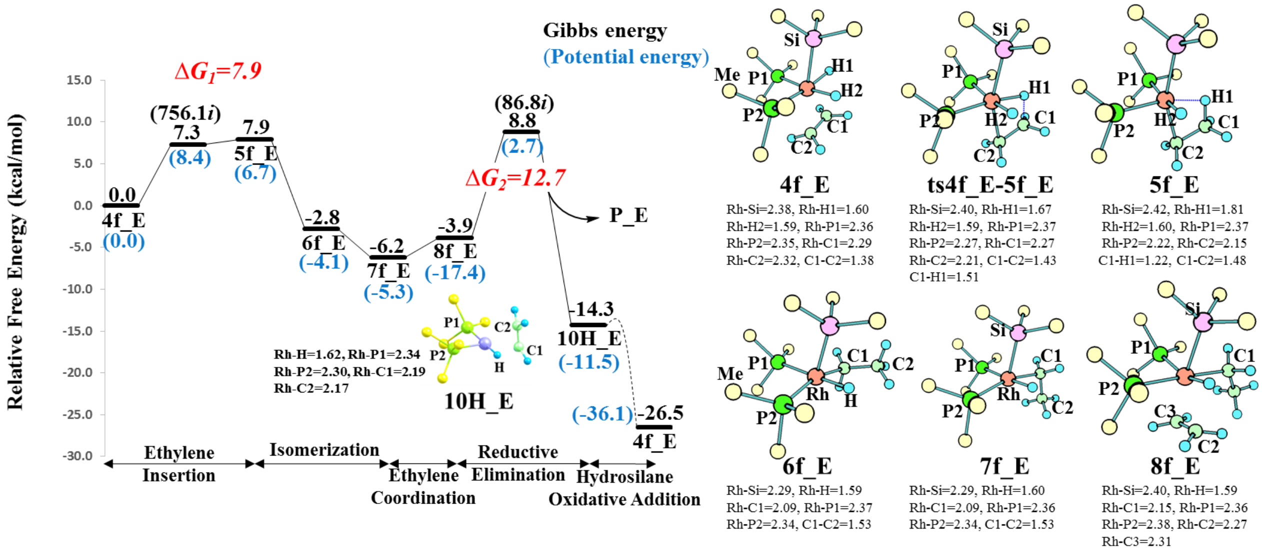

Figure 21 Gibbs free energy profile for the DH mechanism in ethylene hydrosilylation (4f_E pathway), and important intermediates and transition state in the 4f_E pathway. Important bond lengths are shown in Å.

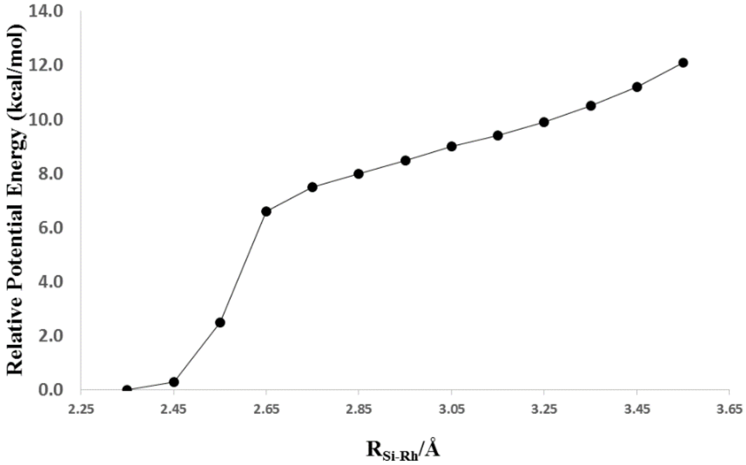

Figure 22 Energy profile in the scan of Si-Rh bond.

In the 4e_E pathway, the Si-C bond reductive elimination is also the rate-determining step. However, different from the 4f_E pathway, an energy barrier of 25.2 kcal/mol is required (see Figure 23). The reason should be attributed to the position of hydride. In the **8f_E** state, hydride is cis to the ethyl group, and the Rh-C1 and Si-C1 distances are 2.15 and 2.97 Å, respectively (See structure in Figure 21). Thus, the agostic interaction between Rh and ethyl group can be found at the transition state of the Si-C reductive elimination. On the other hand, in the **8e_E** state, hydride is trans to the ethyl group (See structure in Figure 24). Consequently, the Rh-C2 distance enlarges to 2.21 Å, and Si-C2 distance also enlarges to 3.33 Å, where no agostic interaction is available in the transition state.

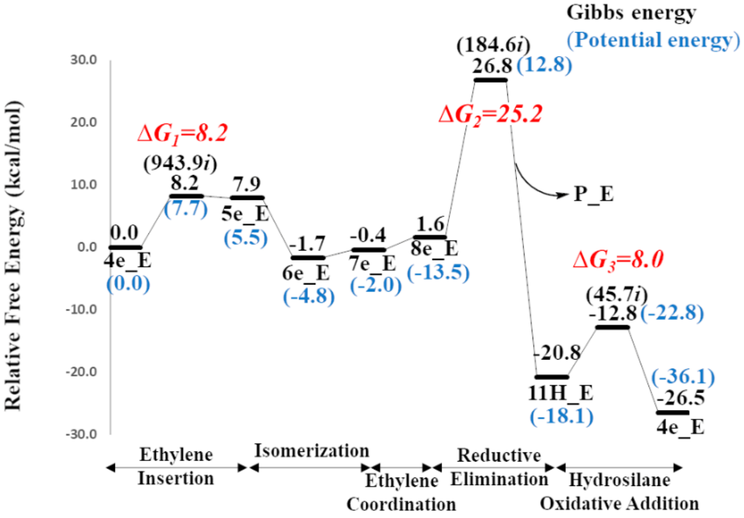

Figure 23 Gibbs free energy profile for DH mechanism in ethylene hydrosilylation (4e_E pathway).

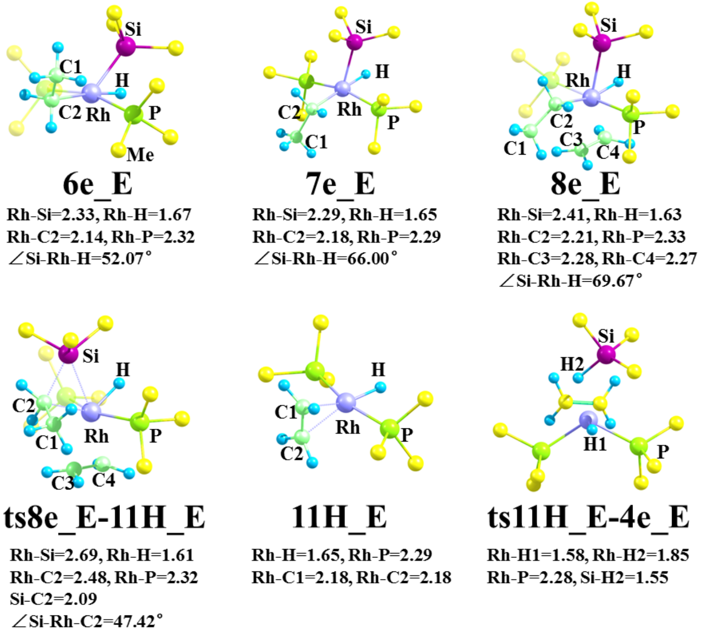

Figure 24 Optimized geometries of **6e_E**, **7e_E**, **8e_E-11H_E** and **ts11H_E-4e_E**. Important bond lengths are shown in Å.

2.3.7 Outer-sphere mechanism

Recently, a new course of the hydrosilylation reaction of carbonyl compounds catalyzed by cationic iridium complexes was proposed. This is known as an outer-sphere mechanism that the carbonyl group directly attacks to the silicon atom of an agostic Si-H bond. In the current work, because there is no agostic Si-H bond in the active species, it is highly expected that the outer-sphere mechanism is not included in the catalytic reaction. Although we found the reaction pathway where an acetone directly attacks to Si atom in **3a** to form a siloxymethyl complex **6bM** (Figure 25), the associated activation energy was estimated to be 45.6 kcal/mol, which is much larger than that 20 kcal/mol in the CH mechanism. Consequently, the outer-sphere mechanism is clearly ruled out.

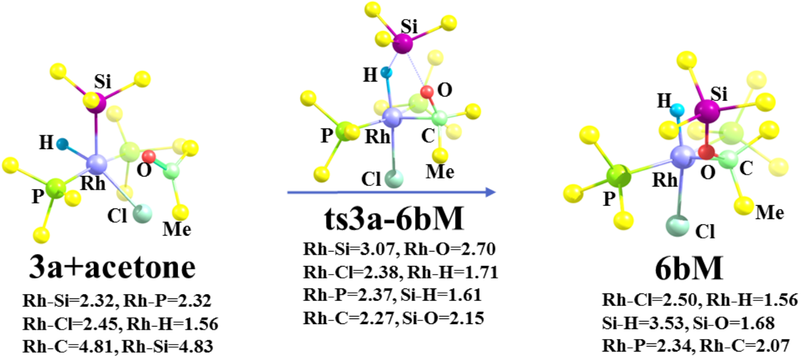

Figure 25 Geometry changes of acetone insertion into Rh-Si bond started from **3a**.

2.4 Conclusion

The mechanism of Rh-catalyzed hydrosilylation of a carbonyl compound (acetone) and an alkene (ethylene) was theoretically investigated by the DFT calculation of free energy profiles. Long standing mechanisms for hydrosilylation, CH and mCH, as well as proposed mechanisms, aCH and DH were examined, and possible interpretations were given.

As for the acetone hydrosilylation, C=O insertion into the Rh-H bond (CH mechanism) is preferred over that into the Rh-Si bond (mCH mechanism). Because acetone coordinates to the Rh center via the lone pair of the O atom, no π backdonation is observed in the Rh complex in the reactant state. As a result, the Rh and C atoms are separated by 3.13 Å due to the coordination structure.

An intermediate species **N2a** was considered since this intermediate opens other catalytic cycles (the aCH and DH mechanisms). This **N2a** is a four-coordinated Rh(I) hydride complex and is formed after the Si-Cl reductive elimination of $SiClMe_3$. Both aCH and DH mechanisms prefer the C=O insertion into Rh-H bond. In particular, the activation energy of the rate-determining step is 13.6 kcal/mol for the DH mechanism, which is smaller than that of CH (20.2 kcal/mol). In the DH mechanism, the Si atom has interaction with the second hydride at the cis position to the silyl group (Si-H cis interaction). This interaction distorts the Rh complex from the octahedral form, and the trans influence of the silyl ligand is weakened. Under the moderate trans influence, the acetone does not break its π bond completely and keeps its original electronic structure in the transition state **ts4f-5f**. Consequently, the activation energy of the C=O insertion into the Rh-H bond would be lowered.

For the ethylene hydrosilylation, the mCH mechanism is calculated to be the most possible mechanism with the energy barrier of 11.2 kcal/mol which is in good agreement with the Sakaki's report. At the same time, our proposed DH mechanism is competitive to the mCH mechanism with a similar energy barrier at the rate-determining step (12.7 kcal/mol). Unlike the mCH pathway, the C=C insertion into the Rh-Si bond becomes energetically more unfavorable than that into the Rh-H bond in the case of the DH pathway. This is due to the Si-H cis interaction which prevents from dissociation of the silyl group from the Rh moiety.

For both aceton hydrosilylation and ethylene hydrosilylation, to generate the **N2a** species, activation energy of 36.1 kcal/mol would be necessary. Although this amount is much larger than that to form the active species **4c** for the CH and mCH mechanisms (18.6 kcal/mol), the resultant active species **N2a** is thermodynamically stable than **4c**. Once **N2a** is formed, the DH catalytic cycle could turn around. Therefore, at reaction conditions where this species is formed, the DH mechanism should be considered.

It should be also noticed that the aCH and CH mechanisms have a common rate-determining step in both C=O and C=C double bond hydrosilylaiton. So, if the CH mechanism is applicable, we should also investigate aCH mechanism (such as Pt-catalyzed hydrosilylation of alkenes).

Finally, the relevance between the proposed mechanisms and the existing mechanisms should be mentioned. If the aCH mechanism is compared with that for $Co_2(CO)_8$ catalyzed hydrosilylation of olefin proposed by Chalk and Harrod, these two mechanisms take different ways to generate reactive species, H-ML_3 (M=Co, L=CO for Chalk and Harrod, M=Rh, L=Me for aCH) and share similar catalytic cycle. As for the DH mechanism, if the Rh-H unit is regarded to single unit such as M=RhH, the Paths A and B in the DH mechanism resemble to the mCH and CH, respectively. However, the advantage of two Rh-H bonds in the Rh catalysts should be noteworthy because these bonds are relevant to lowering the energy barrier in the DH mechanism.

Reference

1. Chalk, A. J.; Harrod, J. F., Reactions between Dicobalt Octacarbonyl and Silicon Hydrides. *J. Am. Chem. Soc.* **1965,** *87* (5), 1133-1135.
2. Chalk, A. J.; Harrod, J. F., Homogeneous Catalysis. II. The Mechanism of the Hydrosilation of Olefins Catalyzed by Group VIII Metal Complexes1. *J. Am. Chem. Soc.* **1965,** *87* (1), 16-21.
3. Chalk, A. J.; Harrod, J. F., Homogeneous Catalysis. IV. Some Reactions of Silicon Hydrides in the Presence of Cobalt Carbonyls. *J. Am. Chem. Soc.* **1967,** *89* (7), 1640-1647.
4. Speier, J. L., Homogeneous Catalysis of Hydrosilation by Transition Metals. In *Advances in Organometallic Chemistry*, Stone, F. G. A.; West, R., Eds. Academic Press: 1979; Vol. 17, p 407-447.
5. Harrod, J. F.; Chalk, A. J., Organic Synthesis via Metal Carbonyls. Wender, I.; Pino, P., Eds. John Wiley & Sons Ltd.: New York, 1977; Vol. 2, p 673.
6. Tilley, T. D., The Chemistry of Organic SIlicon Compounds. Patai, S.; Rappoport, Z., Eds. John Wiley & Sons Ltd.: New York, 1989; p 1415.
7. Ojima, I., The Hydrosilylation Reaction. In *Organic Silicon Compounds* John Wiley & Sons,

Ltd: Chichester, UK., 1989; Vol. 1 and Vol. 2, p 1479-1526.
8. Ohsima, K., Advances in Metal-Organic Chemistry. Liebeskind, L. S., Ed. JAI Press Ltd.: London, 1991; Vol. 2, p 101.
9. Millan, A.; Towns, E.; Maitlis, P. M., The Direct Conversion of α-olefins into Vinyl- and Allyl-silances Catalysed by Rhodium Complexes. *J. Chem. Soc., Chem. Commun.* **1981,** (14), 673-674.
10. Millan, A.; Fernandez, M.-J.; Bentz, P.; Maitlis, P. M., Rhodium-catalysed Hydrosilylation: the Direct Production of Alkenyl(triethyl)silanes from Alk-1-enes and Triethylsilane. *J. Mol. Catal.* **1984,** *26* (1), 89-104.
11. Onopchenko, A.; Sabourin, E. T.; Beach, D. L., Rhodium(I)-Catalyzed Hydrosilylation of Styrene. *J. Org. Chem.* **1983,** *48* (25), 5101-5105.
12. Onopchenko, A.; Sabourin, E. T.; Beach, D. L., Vinyl- and Allylsilanes from the Rhodium(I)-catalyzed Hydrosilylation of 1-Alkenes with Trialkylsilanes. *J. Org. Chem.* **1984,** *49* (18), 3389-3392.
13. Ojima, I.; Fuchikami, T.; Yatabe, M., The Reactions of Hydrosilanes with Trifluoropropene and Pentafluorostyrene Catalyzed by Ruthenium, Rhodium and Palladium complexes. *J. Organomet. Chem.* **1984,** *260* (3), 335-346.
14. Bergens, S. H.; Noheda, P.; Whelan, J.; Bosnich, B., Asymmetric Catalysis. Mechanism of Asymmetric Catalytic Intramolecular Hydrosilylation. *J. Am. Chem. Soc.* **1992,** *114* (6), 2128-2135.
15. Duckett, S. B.; Perutz, R. N., Mechanism of Homogeneous Hydrosilation of Alkenes by (η^5-cyclopentadienyl)rhodium. *Organometallics* **1992,** *11* (1), 90-98.
16. Sakaki, S.; Mizoe, N.; Sugimoto, M., Theoretical Study of Platinum(0)-Catalyzed Hydrosilylation of Ethylene. Chalk−Harrod Mechanism or Modified Chalk−Harrod Mechanism. *Organometallics* **1998,** *17* (12), 2510-2523.
17. Sakaki, S.; Sumimoto, M.; Fukuhara, M.; Sugimoto, M.; Fujimoto, H.; Matsuzaki, S., Why Does the Rhodium-Catalyzed Hydrosilylation of Alkenes Take Place through a Modified Chalk−Harrod Mechanism? A Theoretical Study. *Organometallics* **2002,** *21* (18), 3788-3802.
18. Sakaki, S.; Mizoe, N.; Musashi, Y.; Sugimoto, M., Platinum-catalyzed Hydrosilylation of Ethylene. A Theoretical Study on the Reaction Mechanism Involving cis–trans Isomerization of $PtH(SiH_3)(PH_3)_2$. *J. Mol. Struct.: THEOCHEM* **1999,** *461–462*, 533-546.
19. Sakaki, S.; Mizoe, N.; Sugimoto, M.; Musashi, Y., Pt-catalyzed Hydrosilylation of Ethylene. A Theoretical Study of the Reaction Mechanism. *Coord. Chem. Rev.* **1999,** *190–192*, 933-960.
20. Zheng, G. Z.; Chan, T. H., Regiocontrolled Hydrosilation of α,β-Unsaturated Carbonyl Compounds Catalyzed by Hydridotetrakis(triphenylphosphine)rhodium(I). *Organometallics* **1995,** *14* (1), 70-79.
21. Gade, L. H.; César, V.; Bellemin-Laponnaz, S., A Modular Assembly of Chiral Oxazolinylcarbene–Rhodium Complexes: Efficient Phosphane-Free Catalysts for the Asymmetric Hydrosilylation of Dialkyl Ketones. *Angew. Chem. Int. Ed.* **2004,** *43* (8), 1014-1017.
22. Metsänen, T. T.; Hrobárik, P.; Klare, H. F. T.; Kaupp, M.; Oestreich, M., Insight into the Mechanism of Carbonyl Hydrosilylation Catalyzed by Brookhart's Cationic Iridium(III) Pincer Complex. *J. Am. Chem. Soc.* **2014,** *136* (19), 6912-6915.
23. Wang, W.; Gu, P.; Wang, Y.; Wei, H., Theoretical Study of POCOP-Pincer Iridium(III)/Iron(II) Hydride Catalyzed Hydrosilylation of Carbonyl Compounds: Hydride Not

Involved in the Iridium(III) System but Involved in the Iron(II) System. *Organometallics* **2014,** *33* (4), 847-857.

24. Gutsulyak, D. V.; Vyboishchikov, S. F.; Nikonov, G. I., Cationic Silane σ-Complexes of Ruthenium with Relevance to Catalysis. *J. Am. Chem. Soc.* **2010,** *132* (17), 5950-5951.

25. Huang, L.; Wang, W.; Wei, X.; Wei, H., New Insights into Hydrosilylation of Unsaturated Carbon–Heteroatom (C═O, C═N) Bonds by Rhenium(V)–Dioxo Complexes. *J. Phys. Chem. A* **2015,** *119* (16), 3789-3799.

26. Nakatani, N.; Hasegawa, J. Y.; Sunada, Y.; Nagashima, H., Platinum-catalyzed Reduction of Amides with Hydrosilanes Bearing Dual Si-H Groups: A Theoretical Study of The Reaction Mechanism. *Dalton Trans* **2015,** *44* (44), 19344-56.

27. Frisch, M. J.; al, e., Gaussian 09, Revision B.01. Wallingford CT, 2010.

28. Ehlers, A. W.; Böhme, M.; Dapprich, S.; Gobbi, A.; Höllwarth, A.; Jonas, V.; Köhler, K. F.; Stegmann, R.; Veldkamp, A.; Frenking, G., A Set of f-Polarization Functions for Pseudo-potential Basis Sets of the Transition Metals Sc-Cu, Y-Ag and La-Au. *Chem. Phys. Lett.* **1993,** *208* (1), 111-114.

29. Andrae, D.; Häußermann, U.; Dolg, M.; Stoll, H.; Preuß, H., Energy-adjusted Ab Initio Pseudopotentials for the Second and Third Row Transition Elements. *Theoret. Chim. Acta* **1990,** *77* (2), 123-141.

30. Jones, R. A.; Real, F. M.; Wilkinson, G.; Galas, A. M. R.; Hursthouse, M. B.; Malik, K. M. A., Synthesis of trimethylphosphine complexes of rhodium and ruthenium. X-Ray crystal structures of tetrakis(trimethylphosphine)rhodium(I) chloride and chlorotris(trimethylphosphine)rhodium(I). *Journal of the Chemical Society, Dalton Transactions* **1980,** (3), 511-518.

31. Mammen, M.; Shakhnovich, E. I.; Deutch, J. M.; Whitesides, G. M., Estimating the Entropic Cost of Self-Assembly of Multiparticle Hydrogen-Bonded Aggregates Based on the Cyanuric Acid·Melamine Lattice. *J. Org. Chem.* **1998,** *63* (12), 3821-3830.

32. Tomasi, J.; Mennucci, B.; Cammi, R., Quantum Mechanical Continuum Solvation Models. *Chem. Rev.* **2005,** *105* (8), 2999-3094.

Chapter 3

Controlled Intersystem Crossing in Myoglobin Catalyzed Cyclopropanation: A Theoretical Study

3.1 Introduction

3.1.1 Experimental background

In 1977, Mansuy and coworkers found the first example of a carbene complex yielded by metalloporphyrin.[1] In fact, the researches about heme carbene involved carbene transfer reactions blossomed only until recent 10 years. Most of these researches focused on the artificial hemoproteins because the engineered hemoproteins were found to own much better catalytic performance. These carbene transfer reactions include cyclopropanation reaction,[2-10] olefinations of aldehyde,[11] Doyle–Kirmse reaction,[12] insertion reactions of C-H bond,[7, 8, 13-15] Si-H bond,[9, 16] N-H bond,[7, 10, 17, 18] S-H bond,[7, 19] and B-H bond.[20-22] Initially, the native cytochrome P450s were found be effective catalysts in a broad range of important biochemical reactions.[23-26] Inspired by that, the artificial cytochrome P450s and myoglobin were developed as high efficiency catalysts. Hayashi's group recently focused on the structure and reactivity of metal substituted hemoproteins by using the technology of spectroscopy, in order to reveal the mechanism experimentally.[27-30] One of their recent work reported the spectroscopic observation of reconstituted myoglobin which was found able to effectively promote the reaction activity of styrene cyclopropanation reaction with ethyl diazoacetale (EDA).[31]

In their work, two kinds of myoglobin were used as the catalyst of the cyclopropanation reaction, the natural type myoglobin (nMb) and the reconstituted myoglobin (rMb). The former is the combination of protein environment and the iron porphyrin ligand as shown in Fig. 1. The later

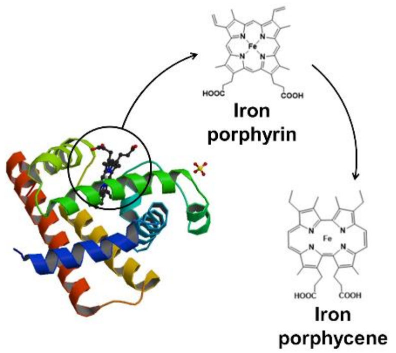

Figure 1 Reconstitution of rMb from nMb

one is synthesized by replacing iron porphyrin in nMb by iron porphycene (see Fig. 1). The idea of using porphycene to replace porphyrin is because porphycene is an isomer of porphyrin but showing totally different physicochemical properties and Hayashi’s group previously found the metal-porphycene myoglobin complexes can help in dioxygen binding or act as the catalyst in peroxidase and hydroxylase reactions.[31] A plausible reaction mechanism of myoglobin catalyzed cyclopropanation reaction is shown in Fig. 2. Obviously, there are two steps for the whole reaction.

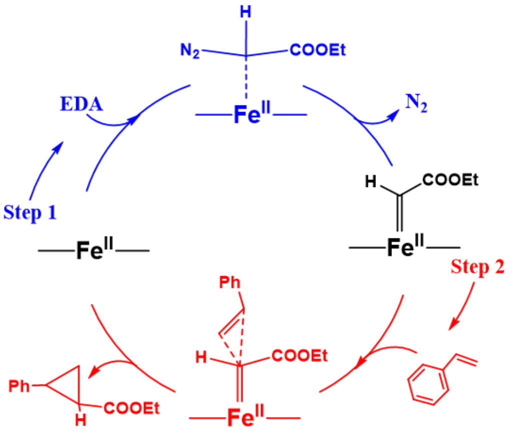

Figure 2 A plausible reaction mechanism of myoglobin catalyzed cyclopropanation

The first step is the carbene generation, followed by the metal-carbene catalyzed cyclopropanation reaction, leading to the product (*E*)-ethyl 2-phenyl-cyclopropanecarboxylate.

In the experiment, the turnover frequency (TOF) and Michaelis-Menten parameters were tested to compare the catalysts' reaction activity. In Michaelis-Menten kinetics, enzyme catalyzed reaction is represented as

$$\mathrm{E + S} \underset{k_{-1}}{\overset{k_1}{\rightleftharpoons}} \mathrm{ES} \xrightarrow{k_{\mathrm{cat}}} \mathrm{E + P},$$

where E, S, and P index the enzyme, substrate, and the product, respectively. Under some assumptions (for example, k_1 and k_{-1} are much larger than k_{cat} so that the enzyme and substrate combination reaction is always in equilibrium), the reaction rate v is written as

$$v = k_{cat}[E]_0 \frac{[S]}{K_M + [S]}, \tag{1}$$

where K_M (also known as Michaelis constant) is

$$K_M = \frac{k_{-1} + k_{cat}}{k_1}. \tag{2}$$

Usually, the constant k_{cat}/K_M is one way to judge how fast the enzyme turns the substrate into product. $[E]_0$ is the initial concentration of the enzyme. When using rMb as the catalyst, the initial TOF is 2.2 s^{-1} which is 35 times higher than using nMb (TOF=15-20 s^{-1} in the same condition.). Similarly, the Michaelis-Menten parameters showed that the k_{cat} value for nMb depends on the EDA concentration, the reaction of the ferrous state of nMb with EDA dominantly limits the rate of product formation. Several reports also support this suggestion.[32, 33] In the case of rMb, k_{cat} and K_m were determined to be 2.1 s^{-1} and 1.9 mM^{-1}, respectively. The k_{cat} values were consistently above one, indicating that the typical steady state analysis can successfully be applied to catalysis by rMb.

On the other hand, the reaction of rMb and nMb with EDA was also evaluated with stopped flow techniques. The results indicated that the catalytic reaction by rMb smoothly proceeds via the carbene intermediate to yield the cyclopropane derivatives. Consequently, they concluded that the reaction rate with rMb is not limited by either the reaction of the ferrous state with EDA or the reaction of the carbene species with styrene.

3.1.2 Theoretical background

As shown in Fig. 2, the reaction is consisted of two steps, carbene formation and the carbene catalyzed cyclopropanation. There are several theoretical studies concerning these two steps, including the formation of carbene, the electronic structure of carbene, the cyclopropanation process, and the role of protein. In this subsection, a short review of these theoretical studies will be introduced.

a) Carbene formation and the properties of carbene

In 2015, the first theoretical study where the DFT method was adopted to investigate the iron porphyrin carbene formation was reported.[34] The reaction pathway of carbene formation is shown in Fig. 3. The diazo complex approaches to the iron porphyrin followed by the N_2 leaving away to generate iron carbene complex. In that study, the binding mode of Fe-C in carbene structure was found to be the terminal mode (the carbon of carbene only form a bond with iron).

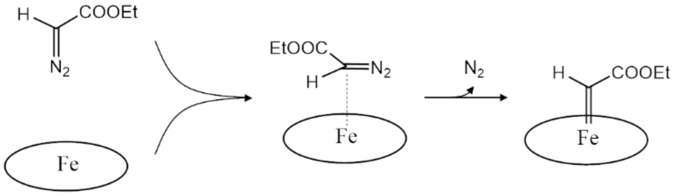

Figure 3 Process of iron carbene formation.

The details about binding mode will be explained in the next paragraph. According to the that study,[34] using electronic-donating group for the carbene substituent or using electronic-withdrawing group for the porphyrin substituent can lower the energy barrier. This is because from the reactant to the transition state, the largest atom charge transfer was found between Fe-C and the transfer direction is from the C to the Fe. If the phenyl substituent was used on the carbene, hydrogen bond may be formed at the transition state. Thus, the stabilized transition state can lead to a smaller energy barrier. The axial ligand was also found to have influence on the activation energy. For the iron carbene formation reaction, the Gibbs free energy barrier and reaction energy were estimated to be 15.8 kcal/mol and -17.5 kcal/mol, respectively. Either the Fe-C bonding mode or the estimation of the energy, the calculated results were consistent with the experimental observations. Another important phenomenon found in the theoretical work is the ISC points in the reaction pathway. Because the active d orbital electrons of iron, the ground spin states of the ferrous state are different from the carbene state. Our study,[31] as well as other theoretical works[35, 36] found the importance of ISC in this reaction. More details about ISC will be explain in subsection 3.3.

In fact, the studies about the electronic and geometric properties of iron carbene structure is even earlier than the whole reaction pathway. The first computational work is in 2014.[37] There are three possible electronic structures were proposed for the bonding of Fe-C in carbene structure as shown in Fig. 4. Fig. 4(a) shows the carbene can be described by $\mathrm{Fe^{II}} \leftarrow [:\mathrm{CHOOEt}]^0$. There are many experimental and theoretical evidences to support this closed-shell singlet electronic

a) $\mathrm{Fe^{II}} \longleftarrow [:\mathrm{CHCOOEt}]^0$

b) $\mathrm{Fe^{IV}} = [\mathrm{CHCOOEt}]^{-2}$

c) $\cdot\,\mathrm{Fe^{III}} \uparrow\downarrow [\cdot\,\mathrm{CHCOOEt}]^-$

Figure 4 Three types of electronic structures of iron carbene.

structure. Experimental evidences include the UV/Vis and the NMR spectroscopy,[38, 39] X-ray tested bond lengths and number of bonds[38, 40-43]. For case Fig. 4(a), there is only one single bond between Fe-C, their binding mode is called terminal mode. For case Fig. 4(c), the carbon usually connects with iron and one N on the porphyrin, the binding mode is called bridging mode.[44]

Some of the experimental evidences were also further explained by the computational work.[34] Theoretical works confirmed structure (a) by charges (only case (a) shows partially positive charge on carbon of carbene),[34, 37, 45, 46] molecular orbitals, [34] and so on. The evidence for case (b) was only found in the experiments basing on the Mössbauer number. It was observed that the Mössbauer isomer shifts of the heme carbene[40, 47, 48] are close to the Fe^{IV} species.[48, 49] The case (c), where the carbene is negatively charged and the total complex is in open-shell singlet state, was only very recently proposed from the computational results.[35]

b) Cyclopropanation process

The first theoretical investigation of heme carbene catalyzed cyclopropanation reaction was reported in 2018.[46] In that work, two possible reaction pathways, which are called concerted reaction pathway and stepwise reaction pathway, were considered as shown in Fig. 5. In the concerted reaction pathway, the C=C double bond breaking and the C-C formation are in the same

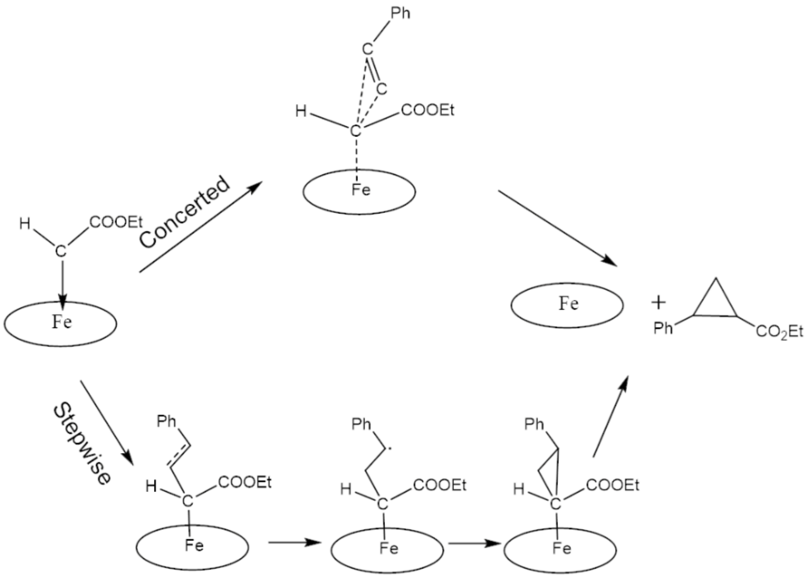

Figure 5 Possible mechanisms of cyclopropanation.

step. In the stepwise one, C-C bond formation and C=C double bond breaking are in different steps. According to the results, the concerted way is more favorable than the stepwise way by around 4-7 kcal/mol. The free energy barrier of the concerted way is about 10.5 kcal/mol, which is smaller than the energy barrier of iron carbene formation by 3.1 kcal/mol. This result again confirmed that the iron carbene formation is the rate-determining step of the whole reaction.

Also, the concerted reaction pathway displayed the selectivity of the *trans* products which is consisted with the experiment. They also studied different kinds of iron carbene by using different carbene substituents, axial ligands or the porphyrin ligands. As for the effect of the carbene substituent, they found the electron-withdrawing substituent can enhance the reactivity.[46] Besides, the steric effect of the carbene substituent would also influence the stability of the transition state. As for the axial effect, neutral ligand is better because of smaller geometry changes. The imidazole ligand is obviously preferable than the charged thiolate ligand (RS^-) or no axial ligand not only in cyclopropanation step but also in carbene formation step. The effect of the ligands on the porphyrin ring is similar to the carbene substituents that the electronic effect and steric effect plays the main role. With electronic-withdrawing group on the porphyrin ring, the carbon is more positive, leading to lower energy barrier than the case of no substituents.

c) Protein environment

If we consider the protein environment, the calculation system will be much larger than the active site because thousands of atoms should be calculated at the same time. Thus, the reports related to this effect only appeared recently. The stereoselectivity was found to have tight relationship with the protein environment by a QM/MM study.[50] Such stereoselectivity is determined by several factors, including the protein steric effect, substrate binding affinity and so on. In another research, the molecular dynamic calculation revealed the kinetic conformation changes of the protein open the gate for reaction.[51] These two studies took the whole protein environment into consideration. There is the third research that only the active site and a small layer of protein atoms were used.[52] DFT method was used in that research with two sets of basis sets, larger basis set for active site and smaller one for the lower layer. This research confirmed that the steric effect will influence the carbene to a specific configuration. Also, they found the attractive van der Waals interaction (hydrogen bond) and the $\pi - \pi$ interaction between the protein and the olefin substrate will influence the stereoselectivity.

From the experimental results and previous studies, the carbene formation is the rate-determining step of the whole reaction. Thus, my research mainly focused on the step of carbene formation. Previously, DFT calculations on the iron carbene species with porphyrin ligand were reported.[34, 35] In these studies, only porphyrin ligand was concerned, and the porphycene ligand was out of their focuses. Zhang et al. also calculated the energy profile of the carbene formation process for the porphyrin ligand.[34] However, their calculations omitted the intersystem crossing processes from quintet state to triplet state and then to singlet state. Therefore, the present calculation provides new insight into the ligand effect (nMb vs rMb) on intersystem crossing pathway, which is one of the essential points of the carbene formation. In the following subsections, a small model where only active site was considered and a large model where the protein was included will be discussed to investigate the mechanism of this reaction.

3.2 Computational details

3.2.1 Small model

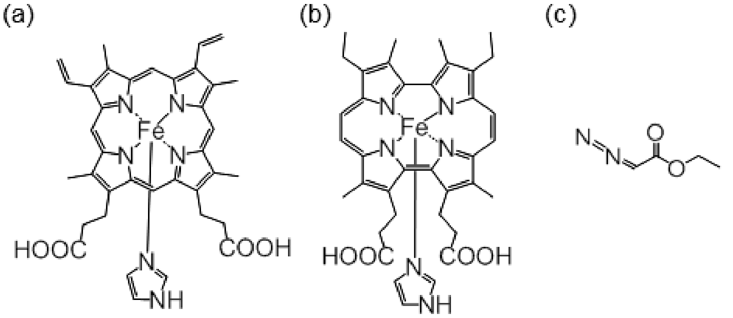

Figure 6 Computational models for the (a) Fe(II)-porphyrin-imidazole and (b) Fe(II)-porphycene-imidazole complexes, and (c) EDA.

At first, we only calculated the reaction happened on the active site which is called small model. For the computational models of Fe(II)-porphyrin-imidazole and Fe(II)-porphycene-imidazole complexes, the structures shown in Fig. 6 were used. The structure of EDA is also shown. All the structures in this work were fully optimized with DFT method by using the unrestricted B97D functional.[53] As for the basis sets, Stuttgart/Dresden (611111/22111/411) sets of the effective-core potential and valence sets were adopted for Fe,[54] while the 6-31g* basis set was used for the other atoms. We adopted this functional and basis sets because this computational setting reproduced the energy difference between spin states for oxyheme ($O_2FePorIm$) in our previous study.[55] Frequency calculations and IRC analyses were conducted to ascertain that proper energy minima and transition states were obtained. All of the above calculations were performed with the Gaussian 09 program package.[56] In finding the MEISCP, the geometries were optimized under the constraint that the two states have to be energetically degenerate. Such optimizations were carried out with a program package developed by our group, which allows for the identification of minimum energy crossing points.[57, 58]

3.2.1 Large model

In the previous work, the protein environment was considered for the second step in the Fig.

2, cyclopropanation reaction.[50-52] I was aimed at investigating the protein effect in the process of iron carbene formation. Also, because the protein structure is flexible, a small geometric change can lead to the fluctuation of the potential energy. Thus, it is necessary to calculate the free energy surface which is the fundamental property of the reaction by using dynamic sampling method. In this work, it is the first trying to apply free energy perturbation (FEP) method for the heme protein system.

a) System setup

All the calculations are based on the nMb crystal structure (PDB ID: 1YMB) and rMb crystal structure (PDB ID: 2V1K). In our computational model, to have a better comparison, the metal atom Mn in 1YMB was replaced by Fe since they have similar electronic structure. The sulfate was removed for its far distance to the active region. The hydrogen atoms were added via Amber tool.[59] Protein residues were carefully checked with visual software VMD to confirm the charge numbers of the system.[60] The Amber tool MCPB.py was used to apply force field to the model system, where RESP charges were calculated at the B3LYP/6-31G* level and TIP3P water model was used.[61] For the standard residues, the general amber force field was used. All the simulations in this work were done by using Amber16. [59] The EDA was manually put on the top of porphyrin or porphycene ring. Then the combined structures were relaxed by 1000 steps minimization followed by 100 ps simulation of heating. Both systems reached the equilibrium before 20 ps. We took two proper snapshots from each simulation as the initial structures for the next step.

b) QM/MM calculation

Considering such large systems, to balance the accuracy and the computational costs, the

QM/MM method was adopted. The ONIOM method implemented in Gaussian16 [62] was used because it allows to define the DFT functional and basis set freely for the QM part. All the QM/MM calculations in this work were conducted with electronic embedding scheme.[63] We adopted a two-layer scheme. QM region was consisted of all the EDA atoms, iron-porphyrin or iron-porphycene ring and part of axial His93 atoms which was truncated between the Cα and the Cβ (see Fig. 7). Therefore, there are 98 QM atoms and 102 QM atoms (capping atoms are not included) for nMb and rMb, respectively. Fig. 7 shows the representative image of QM part. The rest part was considered as MM part. In the two-layer ONIOM method, the total energy is calculated by

$$E_{ONIOM} = E_{high,model} + E_{low,real} - E_{low,model}, \tag{3}$$

where the E_{ONIOM} indexes the total energy estimated by using ONIOM method. $high$ and low represent whether the energy is calculated with high-level or low-level method. $model$ and $real$ index the smaller layer and the total system, respectively. $E_{high,model}$ corresponds to the energy of QM region calculated by DFT method. $E_{low,real}$ and $E_{low,model}$ correspond to the energy of the total system and the MM region calculated by using molecular dynamic method (in this work, the amber method was used), respectively. In ONIOM calculations, the boundary atom was capped by hydrogen.[63] As mentioned, the initial geometries for QM/MM calculation were generated from MM calculation. To save the computational resources, all the counterions and the solvent water that are further than 5 Å to the QM atoms were removed. For the QM part, DFT method with uB97D functional were used as we did in the small model.[31] Effective core potentials and valence electrons of Fe were represented with SDD. The 6-31g* basis sets were adopted for C, H, O, and N.

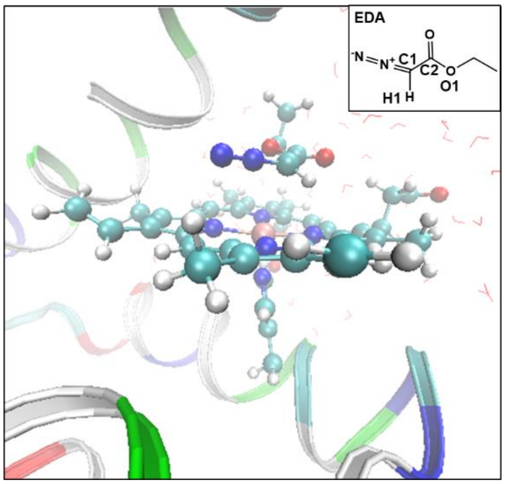

Figure 7 QM region of the large model.

From a simple dynamic simulation, we already had an initial MM optimized structures of reactants. Then, these two reactants were further refined by frozen MM structures and only optimize the QM region. In the same way, only the QM atoms were allowed to move to get the initial structures for the transition state and the carbene complex for each spin state. Finally, each structure was optimized in an iterative way. That is, optimizing the MM and QM part separately until they converged to the same structure. Although it is possible to optimize the whole system together with ONIOM method, in the practice, doing such calculation can easily meet errors like SCF (self-consistent field) errors.

c) Free energy calculation

We used QM/MM method to fully optimize the geometries of reactants, transition states, ISC points, and the products. These structures were the foundation to make potential energy profiles or calculate the free energy. FEP method is a powerful and wild applied technique for the large system like proteins.[64-66] The free energy difference ΔA_{ij} between system i and j can be calculated by

$$\Delta A_{ij} = A_i - A_j = -\frac{1}{\beta}\ln < e^{-\beta(E_i - E_j)} >_j , \quad (4)$$

where the angle brackets represented for the assemble average over the configuration space of system j. E_i and E_j are the potential energy of system i and system j, respectively. In practice, we can't reach all the configurations in one sampling. Such nonergodic problem is quite common in large systems. One of our effort to overcome this problem is to use multi-staging strategy as many other works did.[66-68]

As mentioned, basing on the fully optimized structures, FEP calculations were performed via multi stages. For a pair of target systems, for example the reactant and the transition state, a series of intermediate images were generated. In this way, the QM structure could change little by little. We expected the small step size helps to enlarge the configuration phase space overlap between each pair. A good choice to get the intermediates is to choose structures according to the reaction coordinates, like a certain bond distance or the dihedral angle.[64, 67] After yielding intermediate images, dynamic simulations were done with each fixed QM structure. Belly type dynamic was performed to restrain the QM atoms. After 2000 steps optimization, the systems were heated to the target temperature (300K) by 0.5 fs simulations. Then, the systems were equilibrated to the constant pressure (1 atm). Finally, 600 ps NVT assemble simulations were performed. Every 1 ps the new configuration was saved. We used Gaussian to do the QM/MM single point energy calculation for the selected configurations. According to Equation 4, the QM/MM free energy difference between two images can be calculated by

$$\Delta A_{qm/mm}\left(R_{qm}^{i} \rightarrow R_{qm}^{i+1}\right) = -k_B T ln < \exp\left[-\frac{\Delta E^i}{k_B T}\right] >_{mm,i} \quad (5)$$

where

$$\Delta E^i = E_{qm/mm}\left(\boldsymbol{R}_{qm}^{i+1}, \boldsymbol{R}_{mm}^{i}\right) - E_{qm/mm}\left(\boldsymbol{R}_{qm}^{i}, \boldsymbol{R}_{mm}^{i}\right). \quad (6)$$

In Equation (5), the angle bracket means the simulation is done at QM structure i (notated as simulation i). $E_{qm/mm}\left(\boldsymbol{R}_{qm}^{i+1}, \boldsymbol{R}_{mm}^{i}\right)$ represents the potential energy where the MM structure is gotten from simulation i and QM structure is the image $i+1$. We can call the energy difference calculated in this direction as the forward perturbation energy. If we exchange the label i and $i+1$, then the energy difference is the reverse perturbation energy.

To better estimate the free energy difference, we used overlap sampling (OS) method to average the two direction perturbation results.[65] The original form of OS method is

$$\exp(-\beta \Delta A)=\frac{< w(u) \exp(-\beta u/2) >_0}{< w(u) \exp(+\beta u/2) >_1}, \tag{7}$$

where $u=(E_1-E_0)$ is the potential energy change corresponding to the perturbation. In our case, u is equal to ΔE^i in equation 5 and we simply chose $w(u)=1$.This is referred as simple overlap sampling method. [65] Although we saved 600 trajectories for each simulation, it is not possible to average the potential energy of all these structures due to limited computational resource. According to the work of Thomas, the energy barrier can be converged at 20 data points.[67] Thus, we selected 30 trajectories which are equally spaced to do the single point energy calculation. These potential energy values were used in equation 6.

3.3 Results and discussions

3.3.1 Small model

Although there are several DFT studies on the electronic structure and energy profile for the carbene species with a porphyrin ligand,[34, 35] the present one is the first report on the comparison between the porphyrin and porphycene ligands and also on the reaction pathway via intersystem crossing. The optimized structures and relative potential energies of the ferrous state, the EDA adduct, and the carbene species were calculated for each spin state, singlet, triplet, and quintet.

The estimated energy diagrams for rMb and nMb are summarized in Fig. 8 with showing the key structures at each step. All optimized structures of stable intermediates in different spin states are shown in Fig. 9. In the case of nMb, the stable quintet state of the catalytically-active ferrous state converts to the quintet EDA adduct, and then a quintet/triplet transition occurs via the Q/T crossing point, which is the MEISCP. However, the structure at the Q/T point and its potential energy are both similar to those of the optimized triplet EDA adduct, indicating that the triplet species is efficiently quenched to the stable quintet state of the EDA adduct via a negligible kinetic barrier. The inefficiently generated triplet EDA adduct must overcome an energy barrier of 4.0 kcal/mol (MEISCP T/S) to produce the singlet EDA adduct, which is allowed to transform to the singlet carbene species over an energy barrier of 7.0 kcal/mol. The total barrier for the transition from the quintet state to the singlet state of the EDA adduct is estimated to be 8.2 kcal/mol, because the direct transition from a quintet to a singlet state is prohibited by the selection rule of spin-orbit coupling (the suggested overall pathway to form the carbene species is summarized in Fig. 9). In contrast to nMb, the stable triplet state of ferrous rMb,[69, 70] which results from the strong ligand field of the porphycene relative to the porphyrin, yields the triplet state of the EDA adduct. The triplet adduct is converted to the singlet adduct via MEISCP T/S (energy barrier = 6.2 kcal/mol), and then, the singlet carbene species is produced from the singlet EDA adduct via an energy barrier of 4.6 kcal/mol. Therefore, fewer steps in intersystem crossing are observed for rMb, and the smaller kinetic barriers in rMb relative to nMb strongly support the larger rate constants for the reaction of rMb with EDA compared to that of nMb.

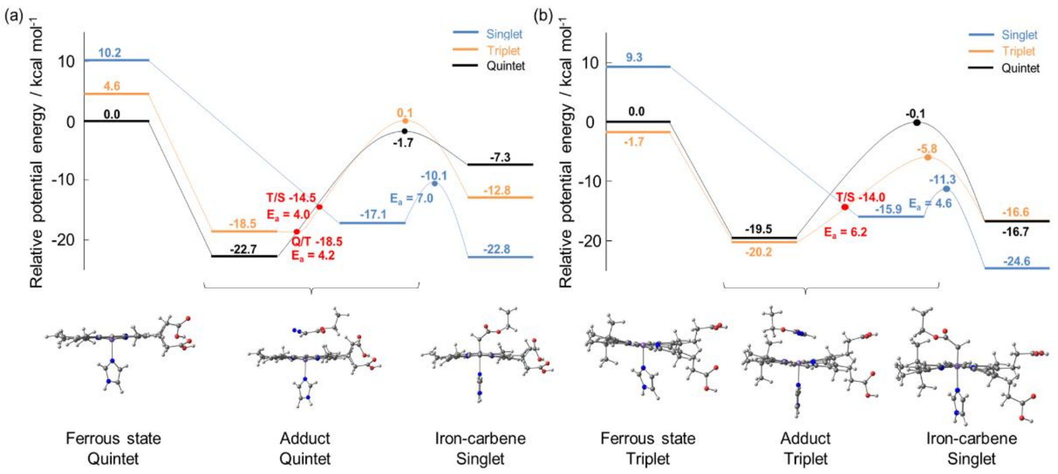

Figure 8 Potential energy diagrams for the reactions of (a) the native heme-imidazole complex with EDA and (b) the FePc-imidazole complex with EDA. Optimized structures of stable intermediates in different spin states at each step in the reaction are shown below the diagrams.

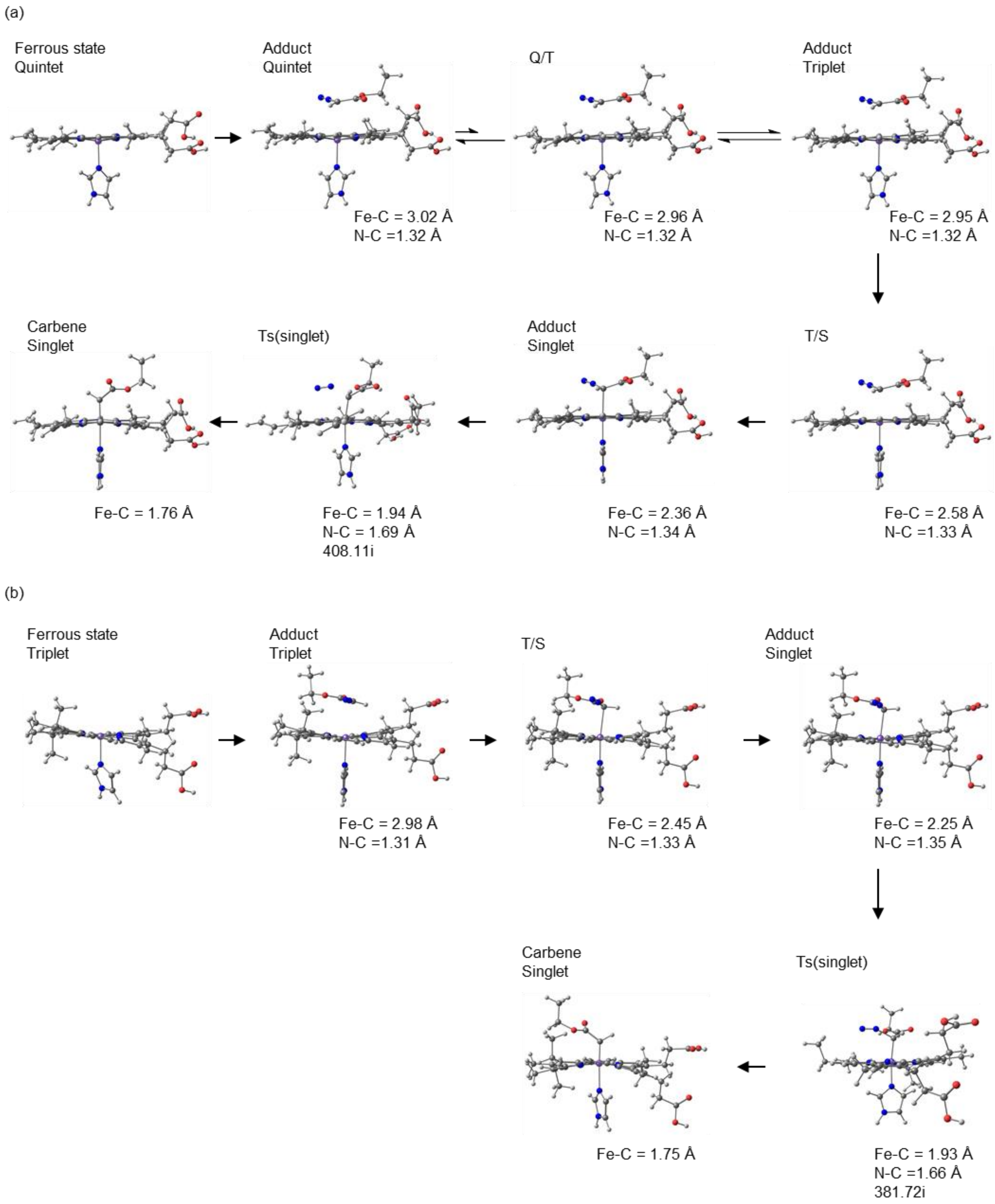

Figure 9 DFT-optimized structures of stable intermediates and transition states in different spin states at each step in the reaction of (a) nMb and (b) rMb with EDA.

A previous study by Shaik et al. focused on the electronic structure of the iron carbene porphyrin with negatively charged cysteine ligand $[SCH_3]^-$. They obtained the open-shell ground state which is about 5 kcal/mol lower than the closed-shell ground state. On the other hand, our system was with neutral imidazole ligand. The change of the ligand affects the stability. With the imidazole ligand, the ground state was calculated to be a closed-shell singlet state. When we did the same calculation as the previous one (stable=opt),[35] the open-shell singlet state was 6.2 kcal/mol and 11.5 kcal/mol higher than the closed-shell singlet state in the nMb and rMb, respectively. The electronic structures of our models, Fe(porphyrin)(imidazole)($CHCO_2Et$) and Fe(porphycene)(imidazole)($CHCO_2Et$), are shown in Fig. 10 and 11, respectively. The charge distributions of the fragments Fe(porphyrin)(imidazole) (or Fe(porphycene)(imidazole)) and $CHCO_2Et$ are same to the Shaik's work, where the Fe is a d^6 configuration and the carbene has no charge or unpaired electrons. The orbital composition analysis was conducted by using natural atomic orbital (NAO) method. In the case of Fe(porphyrin)(imidazole)($CHCO_2Et$), the electronic configuration is similar to that of Shaik's work but without unpaired electrons. There are two bonds between Fe and carbene, one vacant d_{z^2} (Fe) orbital and occupied sp^2 (carbene) orbital formed σ bond, one π-bonding formed by occupied d_{yz} (Fe) orbital and vacant $2p_y$ (carbene) orbital. In both σ and π bonding orbitals, the d orbitals are the major components while in the antibonding orbitals, the orbitals from carbene contribute more. There is no bonding orbital found between the N from imidazole and iron in this case. The electronic structure of Fe(porphycene)(imidazole)($CHCO_2Et$) is alike to the Fe(porphyrin)(imidazole)($CHCO_2Et$) but more complicated. The d orbitals are more delocalized. The energy of bonding σ orbital, which is formed by d_{z^2} orbital of iron and sp^2 orbital of carbene is very near to the energy of N (imidazole) $2p_z$ orbital. Thus, the σ bond also contains the component of N_{2p_z}. The antibonding interaction between N_{2p_z} and d_{z^2} is thought to also have similar energy with d_{xy} orbital. There are two reasons. First, although there is only one d_{xy} orbital showed in Fig. 11 middle column, in fact there are two molecule orbitals with very small energy gap (-0.0077 a.u.) that have d_{xy} component. These two orbitals also have a certain d_{z^2} and N_{2p_z} component. On the other hand, the d_{xy} orbital in the carbene molecular is out of standard shape but a mixed shape with d_{z^2} orbital. Thus, we believe the antibonding of d_{z^2} and N_{2p_z} splits the d_{xy} orbital.

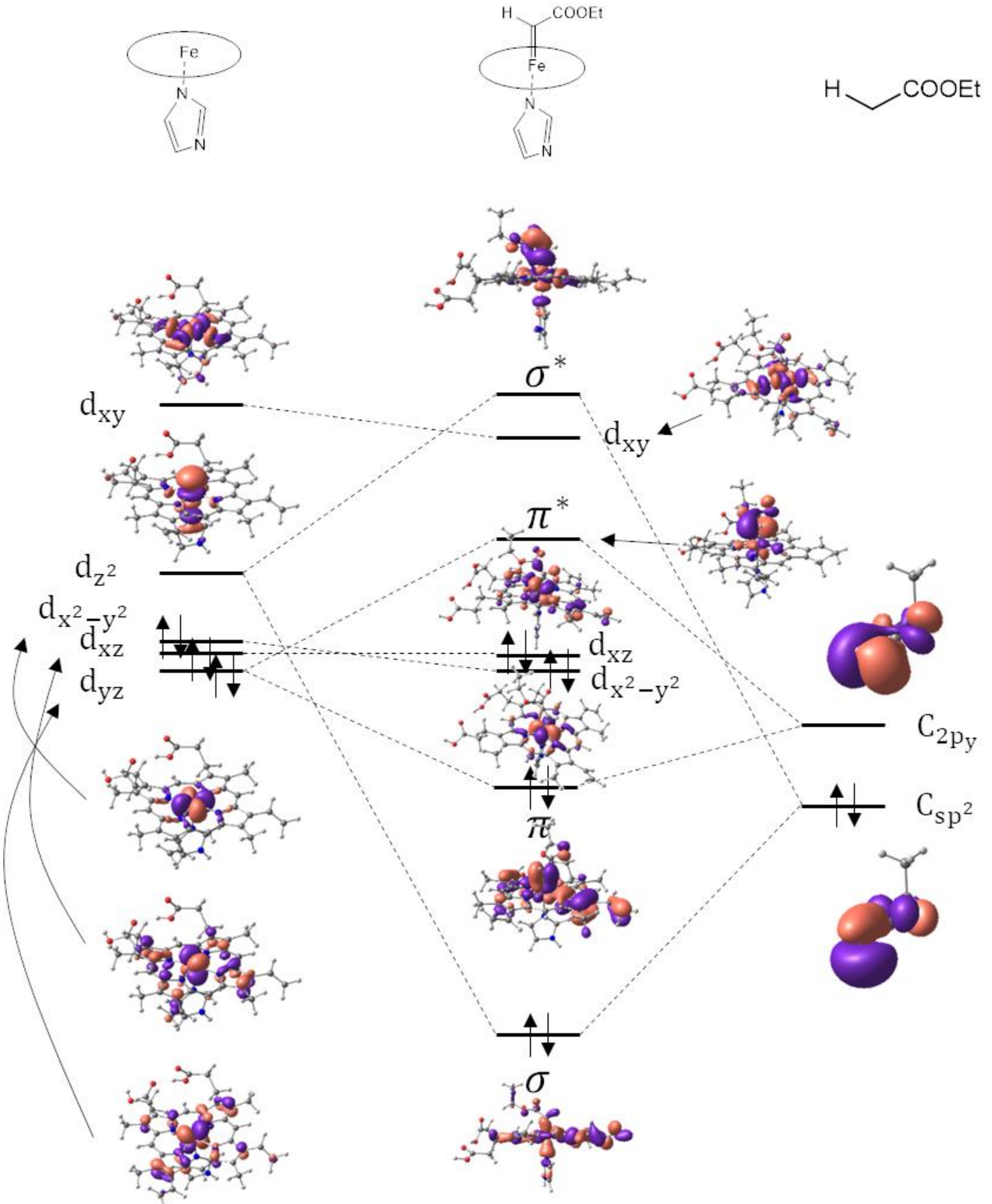

Figure 10 Electronic configurations of singlet Fe(porphyrin)(imidazole)($CHCO_2Et$) complex and its fragments.

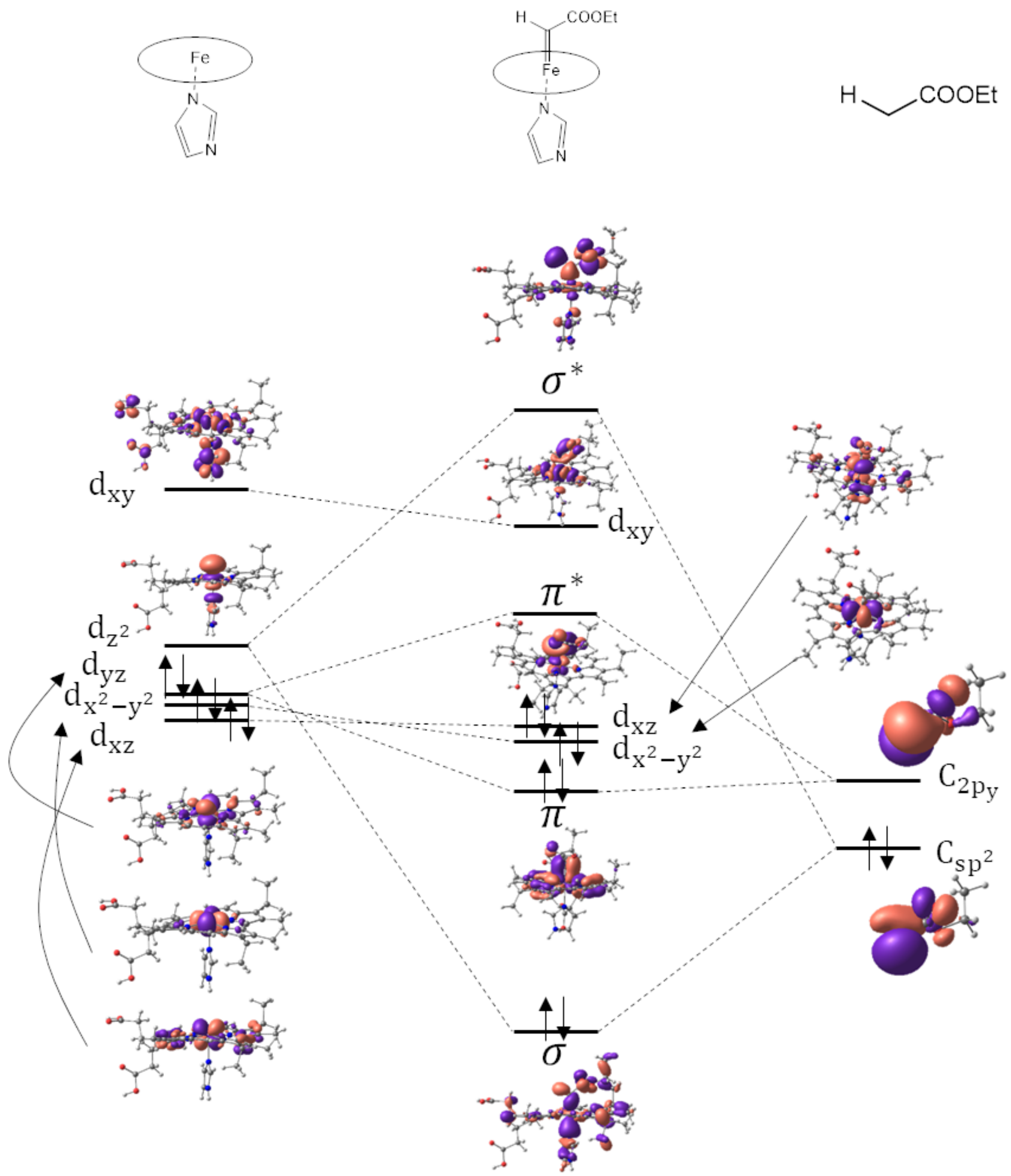

Figure 11 Electronic configurations of singlet Fe(porphycene)(imidazole)($CHCO_2Et$) complex and its fragments.

3.3.2 Large model

a) Geometries and potential surfaces

At first, we fully optimized the reactant, transition state, and product structures on three different spin surfaces with the explicit protein environment at QM/MM level. Also, the ISC points were located. The corresponding potential energy profiles are shown in Fig. 12. Optimized structures are shown in Fig. 13. In the case of nMb, similar to the results of the small model, there are two ISC points in the region of adduct complexes. Through these two points, the complex jumps from the most stable quintet state to the less stable singlet state. The major geometry change along the reaction pathway is the distance between EDA and iron, which is shortened from 3.16 Å to 2.96 Å. After approaching singlet adduct minima, through a 6.7 kcal/mol energy barrier, the singlet iron carbene complex can be formed. Counting the quintet adduct complex as the zero energy point, the total activation energy is 17.6 kcal/mol. The Q/T crossing point was found to be very near to the triplet adduct minima because these two complexes are structurally and energetically alike to each other. The T/S crossing point was also located near to the singlet adduct complex. In the case of rMb, the ground state of adduct complex is triplet state. There is no intersystem crossing happened before the transition state. After overcoming the energy barrier of 16.3 kcal/mol, the triplet iron carbene complex is yielded. Because triplet state is not the most stable state of the iron carbene complex, through a small energy barrier (4.9 kcal/mol) to reach the T/S crossing point, the iron carbene complex can relax to the singlet state. Thus, the ISC points will not cause higher energy barrier than the transition states. The activation energy barrier in the case of rMb is only 1.3 kcal/mol than that of nMb. From this perspective, it is difficult to compare their catalytic activity. The reaction energy of nMb is -7.2 kcal/mol while the reaction energy of rMb is -13.1 kcal/mol. Consequently, the iron carbene formation by using rMb is thermodynamically more favorable.

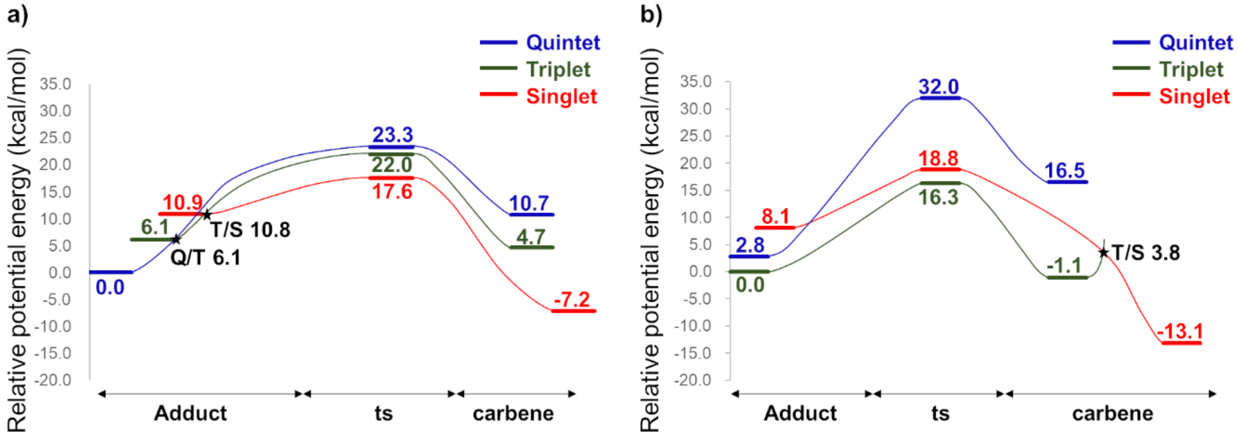

Figure 12 QM/MM method calculated potential energy surfaces of iron carbene formation. a) the case of nMb. b) the case of rMb.

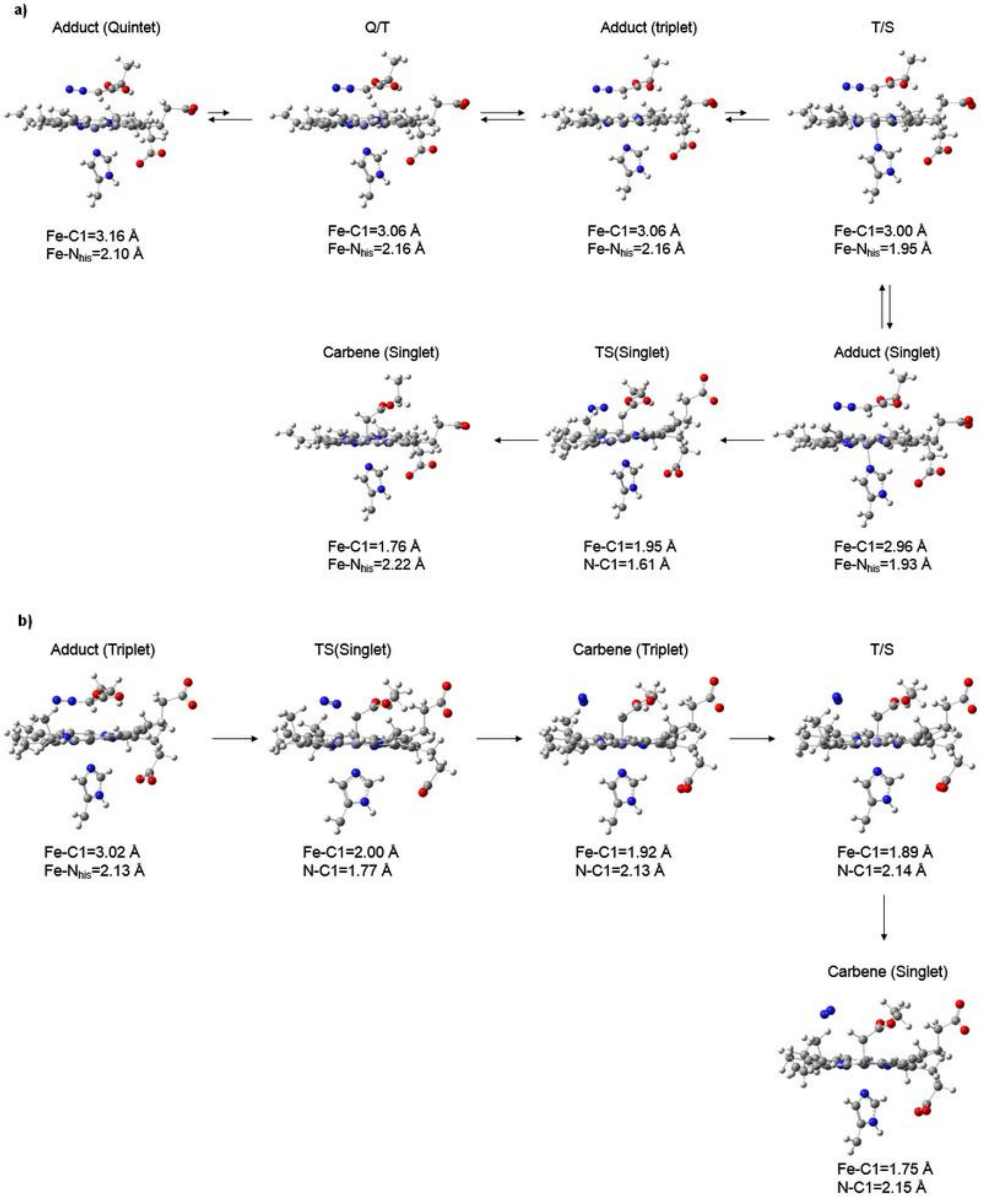

Figure 13 The QM geometries of QM/MM method optimized stable intermediates and transition states in different spin states at each step in the reaction of (a) nMb and (b) rMb with EDA.

Comparing the potential energy surfaces of the small model and the large model, they show high consistency of the tendency but still have notable differences. One obvious difference is that the energy barriers calculated with protein are higher than that of small model in both two cases, which are 5.0 kcal/mol and 7.4 kcal/mol higher for the case of nMb and rMb, respectively. The reasons for the differences will be discussed in the following two paragraphs.

For the case of nMb, we can divide the total energy barrier into two components, the relative energy differences corresponding to the stability of the adduct complexes and the activation energy on the singlet state. With or without protein, the second component contributes energy barrier around 7 kcal/mol (6.7 kcal/mol for the result with protein and 7.0 kcal/mol for the result without protein, see Fig. 8(a) and Fig. 12(a)). Thus, the total energy difference should be attributed to the different stability of the adducts. Naturally, there comes the question why the relative energy between different states of the adduct complex is enlarged when the protein environment is considered. To answer this question, we compared the important structural information of adduct complexes as shown in Table 1. It is easily to find the enlarged Fe-C distance with consideration of protein and solvent water. For the singlet, triplet, and quintet states, the Fe-C distances are larger by 0.60 Å, 0.11 Å, and 0.14 Å, respectively. By investigation, the solvent water molecule should be responsible for the distance changes. Inside the singlet adduct complex, there is a water

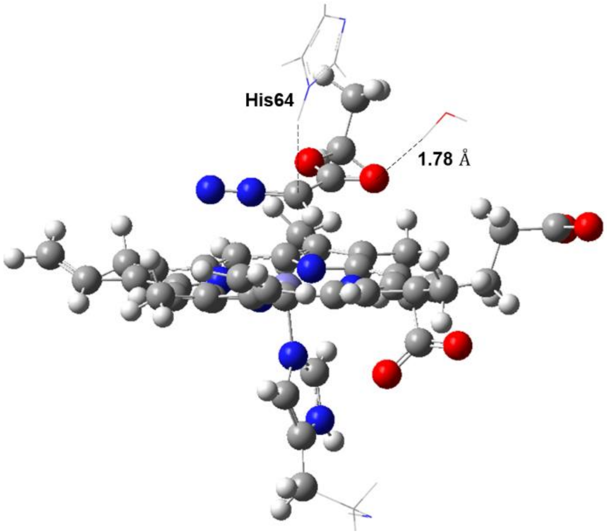

Figure 14 The H of water is close to the O of EDA. Their distance is 1.78 Å

.

molecule close to the O1 of the EDA (the O···H distance is 1.78 Å) as shown in Fig. 14. Because the position of that water is above the EDA, the interatomic interaction between H and O can drag EDA further from the porphyrin ring. Such short distance interaction was also found in the triplet and quintet adduct complexes. But, because the EDA-iron distances in the equilibrium structures of triplet and quintet states are already large, the influence of the water molecule is not so obvious. The longer Fe-C1 distance may indicates the less interaction between iron and EDA. Thus, the singlet adduct complex is less stable.

Table 1 Important geometric information of adduct complexes of different spin states. The values in the grey background were calculated with protein. The values in the white background were calculated without protein.

	Spin state	Fe-C1	Fe-N_{His}	Fe-N_{ring}*	H1-C1-C2-O1
nMb Adduct	Singlet	2.96	1.93	2.00	-17.12
		2.36	1.93	2.00	15.69
	Triplet	3.06	2.16	2.01	-20.23
		2.95	2.20	2.01	-3.64
	Quintet	3.16	2.10	2.09	-21.75
		3.02	2.16	2.08	-4.26
rMb Adduct	Singlet	2.63	1.94	1.96	-9.22
		2.25	1.95	1.96	21.04
	Triplet	3.02	2.13	1.96	-25.37
		2.98	2.20	1.95	-5.02
	Quintet	3.10	2.09	2.04	-24.15
		3.04	2.15	2.04	-5.42

As for the rMb, the larger activation energy calculated with protein is because the change of relative energy order of the transition states. In the small model, the singlet transition state is more stable than the triplet transition state by 5.5 kcal/mol. After considering protein environment, the singlet transition state becomes less stable than the triplet one by 2.5 kcal/mol. Relative to the triplet adduct complex, the stability of the triplet transition state doesn't change much whether protein is considered or not, but singlet transition state is 9.9 kcal/mol less stable with the consideration of the protein environment. The comparison of the structural parameters of the singlet transition states of two models (see Fig. 15 left) indicated their high similarity. The charge transfer between the adduct complexes and the transition states of singlet and triplet case are shown in Fig. 15 right. For simplicity, the singlet and triplet transition states optimized without protein is noted as nPS (no protein singlet state complex) and nPT (no protein triplet state complex), respectively. The corresponding structures optimized with protein environment are indexed as PS and PT, respectively. For the nPS and the nPT, there is large charge transfer between three pairs, C1 and Fe (-0.072e for the nPS, -0.175e for the nPT), N1 and C1 (-0.113e for the nPS, -0.211e for the nPT), and porphycene ring and Fe (-0.189e for the nPS, -0.425e for the nPT). When there is protein, in case of PT, this tendency keeps the same in the charge transfer. However, things get changed for the PS. The charge transfer between C1 and Fe reduces to as less as -0.002e which indicates that there is almost no charge transfer between the two atoms during the formation of the transition state. This is supported by the fact that no Fe-C1 bond was found in this case but the Fe-C1 bond was found in the case of nPS from the NBO analysis. Thus, C1 can't be stabilized by Fe if there is no obvious interaction, leading to the less stable singlet transition state. From another aspect, we can also find the influence of the protein environment to the electronic structure of the active site. There are -0.036e charge transfer from the Fe to the axial ligand in the nPS but -0.006e charge transfer from the axial ligand to the central metal in the PS. Similarly, there are -0.064e charge transfer from Fe to the axial ligand in the nPT but even more charge transfer happens in the same direction in the PT (-0.098e). These facts suggest that the protein environment passes more electron through the axial ligand to the central metal.

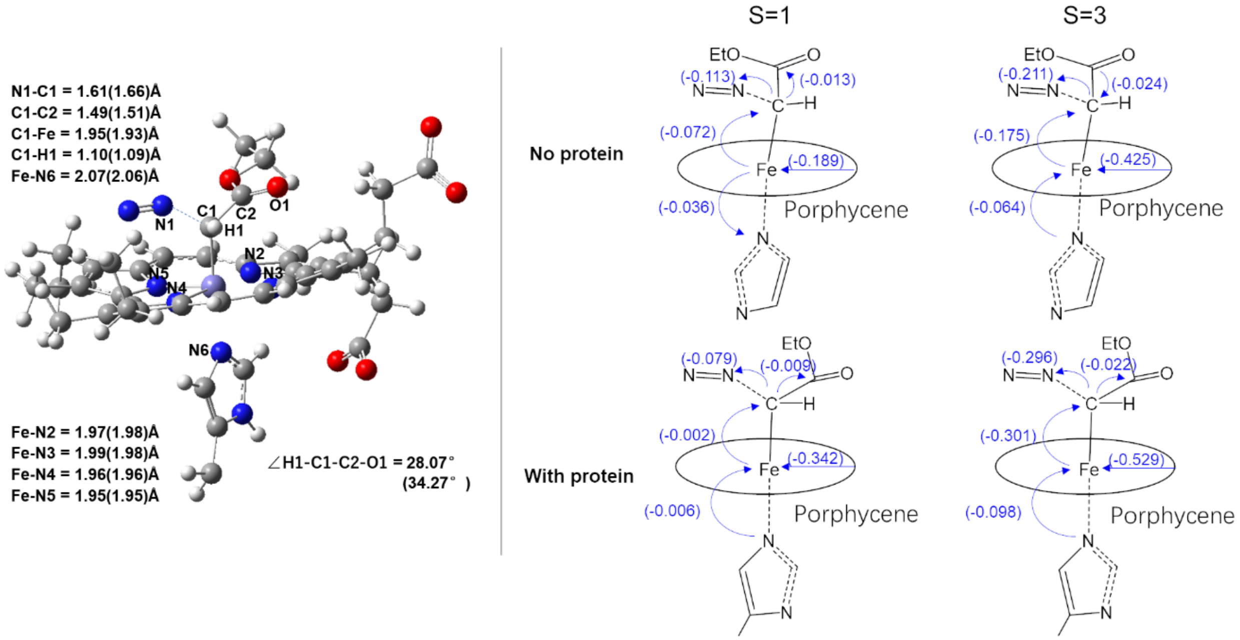

Figure 15 Left: the geometric information of the singlet transition state of the rMb case; the values with and without parenthesis are calculated under large and small models, respectively. Right: charge transfer between the adduct complexes and the transition states in singlet state and triplet state; the upper one shows the results of small model while the bottom one shows the results of the large model.

b) Free energy calculation

The results of free energy calculation are shown in Fig. 16. Because free energy calculation is time consuming, rather than consider all the spin states, only the relative free energy difference between the important structures on the reaction pathway were evaluated. At the same time, in the case of nMb, because the Q/T and T/S crossing points are near triplet and singlet adduct minima, respectively. It was assumed there is no free energy difference between the Q/T crossing point and the triplet minima. And, same assumption was made to the T/S crossing point and the singlet minima. In the case of rMb, we did simulation at the T/S crossing point and selected the structures on the crossing seam (the trajectories that the energy gap is smaller than 0.0001 Hartree were used) to do the free energy calculation. Interestingly, we found if using the QM structure of the crossing point in simulation, the trajectories are mostly on the crossing seam, suggesting that the QM structure is the main factor to control the crossing.

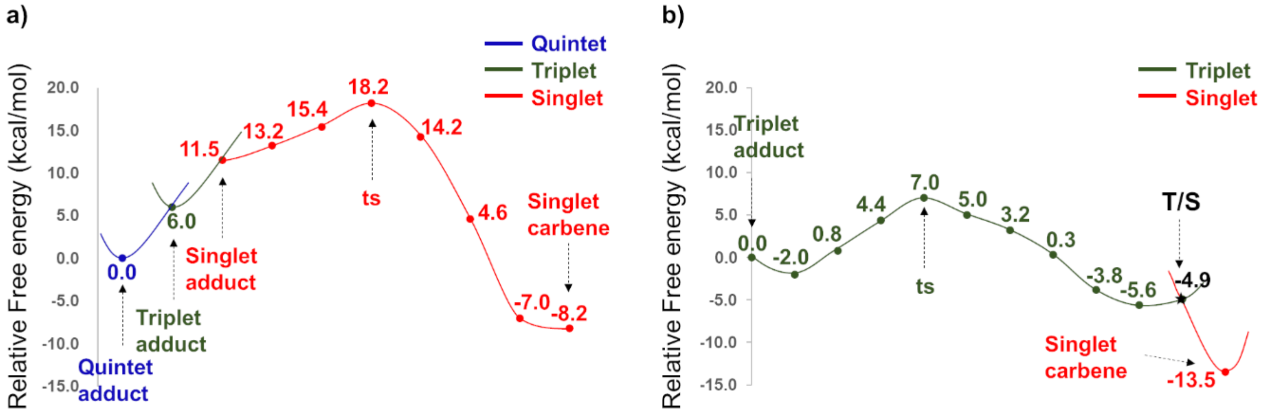

Figure 16 FEP method calculated free energy surfaces. a) the free energy surface of the nMb case. b) the free energy surface of the rMb case.

Fig. 16(b) shows the free energy surface of the case of rMb. From the adduct complex to the transition state, we optimized several structures with fixed Fe-C1 distance and three of these structures were selected to do the FEP calculation. The second window was calculated to be more stable than the optimized triplet adduct complex on the free energy surface. But on the potential energy surface, the second window is less stable than the adduct complex by 7.9 kcal/mol. The Fe-C1 distance of adduct complex is only 0.22Å further than that of the second window. We put the two QM structures in the same figure and moved one structure translationally to overlap their boundary atoms see Fig. 17. Most part of the QM atoms overlap well with each other while the position of one carboxyl groups were slightly different. Thus, it is most possible that the interaction between carboxyl group and the environment leads to the opposite energy order. In the calculation of potential energy, we considered the solvent water molecules around active site and exposed carboxyl groups were found to have interaction with the solvent. However, in the calculation of free energy, although all the windows were optimized under water condition like the optimization of important complexes (adduct, ts, and carbene) and the simulations were conducted in the water box, the water molecules were removed in the single point calculation. Consequently, whether there is water or not can influence the results. Table 2 shows effect of environment waters on energy. Considering only the QM part energy in Table 2, with water the adduct complex is more stable by 22.3 kcal/mol, however, without water the second is more stable by 9.1 kcal/mol. Obviously, the solvent water can stabilize the QM region through interatomic interaction to both structures. But this interaction is much stronger for the adduct complex. Thus, the energy orders of potential energy and the free energy between adduct complex and the second window becomes different.

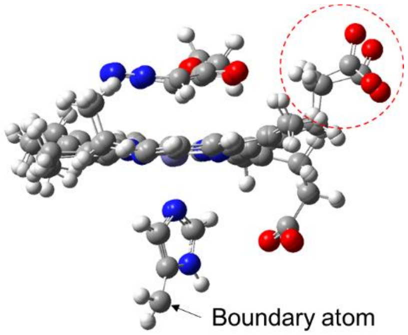

Figure 17 Structural differences between triplet adduct complex and the second window.

Table 2 Comparison of the potential energy between triplet adduct complex and the second window calculated with or without solvent water. The Values in the grey background are the QM part energy. The values in the white background are the total energy. The energy unit is in Hartree.

	With water	No water
Triplet adduct	-2640.66379	-2640.39820
	-2648.73404	-2646.94260
2nd Window	-2640.62827	-2640.41266
	-2648.72138	-2646.97142

3.4 Conclusions

In the experiment, the iron-porphycene substituted myoglobin is found to efficiently react with ethyl diazoacetate to generate the active carbene species for the cyclopropanation of styrene. The catalytic activity of rMb is 26-fold higher than that observed for the native iron porphyrin in the protein matrix.

The results calculated by using small model have already revealed the basic mechanism and strongly support the fact that the strong ligand field of porphycene is useful for the efficient formation of the central carbene intermediate. The reasons are the following, in the case of nMb,1) there is one more ISC point than in the case of rMb; 2) the position of Q/T crossing point is near triplet minima which leads to the easily quenching; 3) the total energy barrier is also 3.7 kcal/mol higher than that of rMb.

With a large computational model, similar potential energy surfaces were got for nMb and rMb involved carbene formation. However, the protein environment can influence the electronic structure of the active sites. Also, the interatomic interaction between the EDA and solvent water or the carboxyl group of porphycene ring and the water changes the stability of the intermediates. As the result, the potential energy surfaces were different. This interatomic interaction is especially obvious in the case of rMb, which leading to the potential energy barrier and the free energy barrier are notably different. We can safely say, without considering the solvent water, the free energy barrier of the rMb case is much lower than that of nMb. For more precise result, we suggest to consider the solvent effect when using FEP method to calculate the free energy.

Reference

1. Mansuy, D.; Lange, M.; Chottard, J.-C.; Guerin, P.; Morliere, P.; Brault, D.;

Rougee, M., Reaction of carbon tetrachloride with 5,10,15,20-tetraphenylporphinatoiron(II)[(TPP)Fe]: evidence for the formation of the carbene complex [(TPP)Fe(CCl2)]. *J. Chem. Soc., Chem. Commun.* **1977,** (18), 648-649.
2. Wang, Z. J.; Renata, H.; Peck, N. E.; Farwell, C. C.; Coelho, P. S.; Arnold, F. H., Improved Cyclopropanation Activity of Histidine-Ligated Cytochrome P450 Enables the Enantioselective Formal Synthesis of Levomilnacipran. *Angew. Chem. Int. Ed.* **2014,** *53* (26), 6810-6813.
3. Renata, H.; Wang, Z. J.; Kitto, R. Z.; Arnold, F. H., P450-catalyzed asymmetric cyclopropanation of electron-deficient olefins under aerobic conditions. *Catal. Sci. Technol.* **2014,** *4* (10), 3640-3643.
4. Heel, T.; McIntosh, J. A.; Dodani, S. C.; Meyerowitz, J. T.; Arnold, F. H., Non-natural Olefin Cyclopropanation Catalyzed by Diverse Cytochrome P450s and Other Hemoproteins. *ChemBioChem* **2014,** *15* (17), 2556-2562.
5. Gober, J. G.; Ghodge, S. V.; Bogart, J. W.; Wever, W. J.; Watkins, R. R.; Brustad, E. M.; Bowers, A. A., P450-Mediated Non-natural Cyclopropanation of Dehydroalanine-Containing Thiopeptides. *ACS Chem. Biol.* **2017,** *12* (7), 1726-1731.
6. Bordeaux, M.; Tyagi, V.; Fasan, R., Highly Diastereoselective and Enantioselective Olefin Cyclopropanation Using Engineered Myoglobin-Based Catalysts. *Angew. Chem. Int. Ed.* **2015,** *54* (6), 1744-1748.
7. Sreenilayam, G.; Moore, E. J.; Steck, V.; Fasan, R., Metal Substitution Modulates the Reactivity and Extends the Reaction Scope of Myoglobin Carbene Transfer Catalysts. *Adv. Synth. Catal.* **2017,** *359* (12), 2076-2089.
8. Key, H. M.; Dydio, P.; Clark, D. S.; Hartwig, J. F., Abiological catalysis by artificial haem proteins containing noble metals in place of iron. *Nature* **2016,** *534* (7608), 534-537.
9. Moore, E. J.; Steck, V.; Bajaj, P.; Fasan, R., Chemoselective Cyclopropanation over Carbene Y–H Insertion Catalyzed by an Engineered Carbene Transferase. *J. Org. Chem.* **2018,** *83* (14), 7480-7490.
10. Wolf, M. W.; Vargas, D. A.; Lehnert, N., Engineering of RuMb: Toward a Green Catalyst for Carbene Insertion Reactions. *Inorg. Chem.* **2017,** *56* (10), 5623-5635.
11. Tyagi, V.; Fasan, R., Myoglobin-Catalyzed Olefination of Aldehydes. *Angew. Chem. Int. Ed.* **2016,** *55* (7), 2512-2516.
12. Tyagi, V.; Sreenilayam, G.; Bajaj, P.; Tinoco, A.; Fasan, R., Biocatalytic Synthesis of Allylic and Allenyl Sulfides through a Myoglobin-Catalyzed Doyle–Kirmse Reaction. *Angew. Chem. Int. Ed.* **2016,** *55* (43), 13562-13566.
13. Dydio, P.; Key, H. M.; Nazarenko, A.; Rha, J. Y.-E.; Seyedkazemi, V.; Clark, D. S.; Hartwig, J. F., An artificial metalloenzyme with the kinetics of native enzymes. *Science* **2016,** *354* (6308), 102-106.
14. Vargas, D. A.; Tinoco, A.; Tyagi, V.; Fasan, R., Myoglobin-Catalyzed C−H Functionalization of Unprotected Indoles. *Angew. Chem. Int. Ed.* **2018,** *57* (31), 9911-9915.
15. Zhang, R. K.; Chen, K.; Huang, X.; Wohlschlager, L.; Renata, H.; Arnold, F. H., Enzymatic assembly of carbon–carbon bonds via iron-catalysed sp3 C–H functionalization. *Nature* **2019,** *565* (7737), 67-72.
16. Kan, S. B. J.; Lewis, R. D.; Chen, K.; Arnold, F. H., Directed evolution of cytochrome c for carbon–silicon bond formation: Bringing silicon to life. *Science* **2016,** *354* (6315), 1048-1051.
17. Wang, Z. J.; Peck, N. E.; Renata, H.; Arnold, F. H., Cytochrome P450-catalyzed insertion

of carbenoids into N–H bonds. *Chem. Sci.* **2014,** *5* (2), 598-601.
18. Sreenilayam, G.; Fasan, R., Myoglobin-catalyzed intermolecular carbene N–H insertion with arylamine substrates. *Chem. Commun.* **2015,** *51* (8), 1532-1534.
19. Tyagi, V.; Bonn, R. B.; Fasan, R., Intermolecular carbene S–H insertion catalysed by engineered myoglobin-based catalysts. *Chem. Sci.* **2015,** *6* (4), 2488-2494.
20. Kan, S. B. J.; Huang, X.; Gumulya, Y.; Chen, K.; Arnold, F. H., Genetically programmed chiral organoborane synthesis. *Nature* **2017,** *552* (7683), 132-136.
21. Huang, X.; Garcia-Borràs, M.; Miao, K.; Kan, S. B. J.; Zutshi, A.; Houk, K. N.; Arnold, F. H., A Biocatalytic Platform for Synthesis of Chiral α-Trifluoromethylated Organoborons. *ACS Cent. Sci.* **2019,** *5* (2), 270-276.
22. Chen, K.; Huang, X.; Zhang, S.-Q.; Zhou, A. Z.; Kan, S. B. J.; Hong, X.; Arnold, F. H., Engineered Cytochrome c-Catalyzed Lactone-Carbene B–H Insertion. *Synlett* **2019,** *30* (04), 378-382.
23. Meunier, B.; de Visser, S. P.; Shaik, S., Mechanism of Oxidation Reactions Catalyzed by Cytochrome P450 Enzymes. *Chem. Rev.* **2004,** *104* (9), 3947-3980.
24. Bernhardt, R., Cytochromes P450 as versatile biocatalysts. *J. Biotechnol.* **2006,** *124* (1), 128-145.
25. de Visser, S. P.; Kumar, D.; Cohen, S.; Shacham, R.; Shaik, S., A Predictive Pattern of Computed Barriers for C−H Hydroxylation by Compound I of Cytochrome P450. *J. Am. Chem. Soc.* **2004,** *126* (27), 8362-8363.
26. Irigaray, P.; Belpomme, D., Basic properties and molecular mechanisms of exogenous chemical carcinogens. *Carcinogenesis* **2009,** *31* (2), 135-148.
27. Matsuo, T.; Dejima, H.; Hirota, S.; Murata, D.; Sato, H.; Ikegami, T.; Hori, H.; Hisaeda, Y.; Hayashi, T., Ligand Binding Properties of Myoglobin Reconstituted with Iron Porphycene: Unusual O2 Binding Selectivity against CO Binding1. *J. Am. Chem. Soc.* **2004,** *126* (49), 16007-16017.
28. Hayashi, T.; Murata, D.; Makino, M.; Sugimoto, H.; Matsuo, T.; Sato, H.; Shiro, Y.; Hisaeda, Y., Crystal Structure and Peroxidase Activity of Myoglobin Reconstituted with Iron Porphycene. *Inorg. Chem.* **2006,** *45* (26), 10530-10536.
29. Oohora, K.; Kihira, Y.; Mizohata, E.; Inoue, T.; Hayashi, T., C(sp3)–H Bond Hydroxylation Catalyzed by Myoglobin Reconstituted with Manganese Porphycene. *J. Am. Chem. Soc.* **2013,** *135* (46), 17282-17285.
30. Morita, Y.; Oohora, K.; Sawada, A.; Doitomi, K.; Ohbayashi, J.; Kamachi, T.; Yoshizawa, K.; Hisaeda, Y.; Hayashi, T., Intraprotein transmethylation via a CH3–Co(iii) species in myoglobin reconstituted with a cobalt corrinoid complex. *Dalton Trans.* **2016,** *45* (8), 3277-3284.
31. Oohora, K.; Meichin, H.; Zhao, L.; Wolf, M. W.; Nakayama, A.; Hasegawa, J.-y.; Lehnert, N.; Hayashi, T., Catalytic Cyclopropanation by Myoglobin Reconstituted with Iron Porphycene: Acceleration of Catalysis due to Rapid Formation of the Carbene Species. *J. Am. Chem. Soc.* **2017,** *139* (48), 17265-17268.
32. Mbuvi, H. M.; Woo, L. K., Catalytic C−H Insertions Using Iron(III) Porphyrin Complexes. *Organometallics* **2008,** *27* (4), 637-645.
33. Dzik, W. I.; Xu, X.; Zhang, X. P.; Reek, J. N. H.; de Bruin, B., ‘Carbene Radicals’ in CoII(por)-Catalyzed Olefin Cyclopropanation. *J. Am. Chem. Soc.* **2010,** *132* (31), 10891-10902.
34. Khade, R. L.; Zhang, Y., Catalytic and Biocatalytic Iron Porphyrin Carbene Formation: Effects of Binding Mode, Carbene Substituent, Porphyrin Substituent, and Protein Axial Ligand.

J. Am. Chem. Soc. **2015,** *137* (24), 7560-7563.
35. Sharon, D. A.; Mallick, D.; Wang, B.; Shaik, S., Computation Sheds Insight into Iron Porphyrin Carbenes' Electronic Structure, Formation, and N–H Insertion Reactivity. *J. Am. Chem. Soc.* **2016,** *138* (30), 9597-9610.
36. Torrent-Sucarrat, M.; Arrastia, I.; Arrieta, A.; Cossío, F. P., Stereoselectivity, Different Oxidation States, and Multiple Spin States in the Cyclopropanation of Olefins Catalyzed by Fe–Porphyrin Complexes. *ACS Catalysis* **2018,** *8* (12), 11140-11153.
37. Khade, R. L.; Fan, W.; Ling, Y.; Yang, L.; Oldfield, E.; Zhang, Y., Iron Porphyrin Carbenes as Catalytic Intermediates: Structures, Mössbauer and NMR Spectroscopic Properties, and Bonding. *Angew. Chem. Int. Ed.* **2014,** *53* (29), 7574-7578.
38. Mansuy, D.; Battioni, J. P.; Lavallee, D. K.; Fischer, J.; Weiss, R., Nature of the complexes derived from the reaction of 1,1-bis(p-chlorophenyl)-2,2,2-trichloroethane (DDT) with iron porphyrins: crystal and molecular structure of the vinylidene carbene complex Fe(TPP)(C:C(p-ClC6H4)2). *Inorg. Chem.* **1988,** *27* (6), 1052-1056.
39. Guerin, P.; Battioni, J.-P.; Chottard, J.-C.; Mansuy, D., Complexes de la ferrotetraphenylporphyrine avec des halogenoalkylcarbenes: Fe[TPP][C(X)R]. *J. Organomet. Chem.* **1981,** *218* (2), 201-209.
40. Li, Y.; Huang, J.-S.; Zhou, Z.-Y.; Che, C.-M.; You, X.-Z., Remarkably Stable Iron Porphyrins Bearing Nonheteroatom-Stabilized Carbene or (Alkoxycarbonyl)carbenes: Isolation, X-ray Crystal Structures, and Carbon Atom Transfer Reactions with Hydrocarbons. *J. Am. Chem. Soc.* **2002,** *124* (44), 13185-13193.
41. Mansuy, D.; Lange, M.; Chottard, J. C.; Bartoli, J. F.; Chevrier, B.; Weiss, R., Dichlorocarbene Complexes of Iron(II)-Porphyrins–Crystal and Molecular Structure of Fe(TPP)(CCl2)(H2O). *Angewandte Chemie International Edition in English* **1978,** *17* (10), 781-782.
42. Liu, Y.; Xu, W.; Zhang, J.; Fuller, W.; Schulz, C. E.; Li, J., Electronic Configuration and Ligand Nature of Five-Coordinate Iron Porphyrin Carbene Complexes: An Experimental Study. *J. Am. Chem. Soc.* **2017,** *139* (14), 5023-5026.
43. Wang, H.; Schulz, C. E.; Wei, X.; Li, J., New Insights into the Ligand Nature of Carbene: Synthesis and Characterizations of Six-Coordinate Iron(II) Carbene Porphyrin Complexes. *Inorg. Chem.* **2019,** *58* (1), 143-151.
44. Nicolas, I.; Maux, P. L.; Simonneaux, G., Synthesis of chiral water-soluble metalloporphyrins (Fe, Ru,): new catalysts for asymmetric carbene transfer in water. *Tetrahedron Lett.* **2008,** *49* (40), 5793-5795.
45. Khade, R. L.; Zhang, Y., C−H Insertions by Iron Porphyrin Carbene: Basic Mechanism and Origin of Substrate Selectivity. *Chem. Eur. J.* **2017,** *23* (70), 17654-17658.
46. Wei, Y.; Tinoco, A.; Steck, V.; Fasan, R.; Zhang, Y., Cyclopropanations via Heme Carbenes: Basic Mechanism and Effects of Carbene Substituent, Protein Axial Ligand, and Porphyrin Substitution. *J. Am. Chem. Soc.* **2018,** *140* (5), 1649-1662.
47. Lewis, R. D.; Garcia-Borràs, M.; Chalkley, M. J.; Buller, A. R.; Houk, K. N.; Kan, S. B. J.; Arnold, F. H., Catalytic iron-carbene intermediate revealed in a cytochrome *c* carbene transferase. *Proc. Natl. Acad. Sci.* **2018,** *115* (28), 7308-7313.
48. English, D. R.; Hendrickson, D. N.; Suslick, K. S., Moessbauer spectra of oxidized iron porphyrins. *Inorg. Chem.* **1983,** *22* (2), 367-368.
49. Ling, Y.; Davidson, V. L.; Zhang, Y., Unprecedented Fe(IV) Species in a Diheme Protein MauG: A Quantum Chemical Investigation on the Unusual Mössbauer Spectroscopic Properties.

J. Phys. Chem. Lett. **2010,** *1* (19), 2936-2939.
50. Su, H.; Ma, G.; Liu, Y., Theoretical Insights into the Mechanism and Stereoselectivity of Olefin Cyclopropanation Catalyzed by Two Engineered Cytochrome P450 Enzymes. *Inorg. Chem.* **2018,** *57* (18), 11738-11745.
51. Villarino, L.; Splan, K. E.; Reddem, E.; Alonso-Cotchico, L.; Gutiérrez de Souza, C.; Lledós, A.; Maréchal, J.-D.; Thunnissen, A.-M. W. H.; Roelfes, G., An Artificial Heme Enzyme for Cyclopropanation Reactions. *Angew. Chem. Int. Ed.* **2018,** *57* (26), 7785-7789.
52. Tinoco, A.; Wei, Y.; Bacik, J.-P.; Carminati, D. M.; Moore, E. J.; Ando, N.; Zhang, Y.; Fasan, R., Origin of High Stereocontrol in Olefin Cyclopropanation Catalyzed by an Engineered Carbene Transferase. *ACS Catalysis* **2019,** *9* (2), 1514-1524.
53. Grimme, S., Semiempirical GGA-type density functional constructed with a long-range dispersion correction. *J. Comput. Chem.* **2006,** *27* (15), 1787-1799.
54. Watanabe, K. j.; Nakatani, N.; Nakayama, A.; Higashi, M.; Hasegawa, J.-y., Spin-Blocking Effect in CO and H2 Binding Reactions to Molybdenocene and Tungstenocene: A Theoretical Study on the Reaction Mechanism via the Minimum Energy Intersystem Crossing Point. *Inorg. Chem.* **2016,** *55* (16), 8082-8090.
55. Dolg, M.; Wedig, U.; Stoll, H.; Preuss, H., Energy‐adjusted ab initio pseudopotentials for the first row transition elements. *J. Chem. Phys.* **1987,** *86* (2), 866-872.
56. Frisch, M. J.; Trucks, G. W.; Schlegel, H. B.; Scuseria, G. E.; Robb, M. A.; Cheeseman, J. R.; Scalmani, G.; Barone, V.; Petersson, G. A.; Nakatsuji, H.; Li, X.; Caricato, M.; Marenich, A.; Bloino, J.; Janesko, B. G.; Gomperts, R.; Mennucci, B.; Hratchian, H. P.; Ortiz, J. V.; Izmaylov, A. F.; Sonnenberg, J. L.; Williams-Young, D.; Ding, F.; Lipparini, F.; Egidi, F.; Goings, J.; Peng, B.; Petrone, A.; Henderson, T.; Ranasinghe, D.; Zakrzewski, V. G.; Gao, J.; Rega, N.; Zheng, G.; Liang, W.; Hada, M.; Ehara, M.; Toyota, K.; Fukuda, R.; Hasegawa, J.; Ishida, M.; Nakajima, T.; Honda, Y.; Kitao, O.; Nakai, H.; Vreven, T.; Throssell, K.; Montgomery, J. A.; Jr.; Peralta, J. E.; Ogliaro, F.; Bearpark, M.; Heyd, J. J.; Brothers, E.; Kudin, K. N.; Staroverov, V. N.; Keith, T.; Kobayashi, R.; Normand, J.; Raghavachari, K.; Rendell, A.; Burant, J. C.; Iyengar, S. S.; Tomasi, J.; Cossi, M.; Millam, J. M.; Klene, M.; Adamo, C.; Cammi, R.; Ochterski, J. W.; Martin, R. L.; Morokuma, K.; Farkas, O.; Foresman, J. B.; Fox, D. J. *Gaussian 09 Rev. B.01*, Wallingford, CT, 2016.
57. Levine, B. G.; Coe, J. D.; Martínez, T. J., Optimizing Conical Intersections without Derivative Coupling Vectors: Application to Multistate Multireference Second-Order Perturbation Theory (MS-CASPT2). *J. Phys. Chem. B* **2008,** *112* (2), 405-413.
58. Nakayama, A.; Harabuchi, Y.; Yamazaki, S.; Taketsugu, T., Photophysics of cytosine tautomers: new insights into the nonradiative decay mechanisms from MS-CASPT2 potential energy calculations and excited-state molecular dynamics simulations. *Phys. Chem. Chem. Phys.* **2013,** *15* (29), 12322-12339.
59. Case, D. A.; Betz, R. M.; Cerutti, D. S.; Cheatham, T. E.; III; Darden, T. A.; Duke, R. E.; Giese, T. J.; Gohlke, H.; Goetz, A. W.; Homeyer, N.; Izadi, S.; Janowski, P.; Kaus, J.; Kovalenko, A.; Lee, T. S.; LeGrand, S.; Li, P.; Lin, C.; Luchko, T.; Luo, R.; Madej, B.; Mermelstein, D.; Merz, K. M.; Monard, G.; Nguyen, H.; Nguyen, H. T.; Omelyan, I.; Onufriev, A.; Roe, D. R.; Roitberg, A.; Sagui, C.; Simmerling, C. L.; Botello-Smith, W. M.; Swails, J.; C.Walker, R.; Wang, J.; Wolf, R. M.; Wu, X.; Xiao, L.; Kollman, P. A. *AMBER 2016*, University of California, San Francisco.
60. Humphrey, W.; Dalke, A.; Schulten, K., VMD -- Visual Molecular Dynamics. *J. Mol.*

Graph. **1996,** *14*, 33-38.
61. Li, P.; Merz, K. M., MCPB.py: A Python Based Metal Center Parameter Builder. *J. Chem. Inf. Model.* **2016,** *56* (4), 599-604.
62. Frisch, M. J.; Trucks, G. W.; Schlegel, H. B.; Scuseria, G. E.; Robb, M. A.; Cheeseman, J. R.; Scalmani, G.; Barone, V.; Petersson, G. A.; Nakatsuji, H.; Li, X.; Caricato, M.; Marenich, A. V.; Bloino, J.; Janesko, B. G.; Gomperts, R.; Mennucci, B.; Hratchian, H. P.; Ortiz, J. V.; Izmaylov, A. F.; Sonnenberg, J. L.; Williams; Ding, F.; Lipparini, F.; Egidi, F.; Goings, J.; Peng, B.; Petrone, A.; Henderson, T.; Ranasinghe, D.; Zakrzewski, V. G.; Gao, J.; Rega, N.; Zheng, G.; Liang, W.; Hada, M.; Ehara, M.; Toyota, K.; Fukuda, R.; Hasegawa, J.; Ishida, M.; Nakajima, T.; Honda, Y.; Kitao, O.; Nakai, H.; Vreven, T.; Throssell, K.; Montgomery Jr., J. A.; Peralta, J. E.; Ogliaro, F.; Bearpark, M. J.; Heyd, J. J.; Brothers, E. N.; Kudin, K. N.; Staroverov, V. N.; Keith, T. A.; Kobayashi, R.; Normand, J.; Raghavachari, K.; Rendell, A. P.; Burant, J. C.; Iyengar, S. S.; Tomasi, J.; Cossi, M.; Millam, J. M.; Klene, M.; Adamo, C.; Cammi, R.; Ochterski, J. W.; Martin, R. L.; Morokuma, K.; Farkas, O.; Foresman, J. B.; Fox, D. J. *Gaussian 16 Rev. E.01*, Wallingford, CT, 2016.
63. Chung, L. W.; Sameera, W. M. C.; Ramozzi, R.; Page, A. J.; Hatanaka, M.; Petrova, G. P.; Harris, T. V.; Li, X.; Ke, Z.; Liu, F.; Li, H.-B.; Ding, L.; Morokuma, K., The ONIOM Method and Its Applications. *Chem. Rev.* **2015,** *115* (12), 5678-5796.
64. *Free Energy Calculations: Theory and Applications in Chemistry and Biology*. Springer: 2007.
65. Lu, N.; Kofke, D. A.; Woolf, T. B., Improving the efficiency and reliability of free energy perturbation calculations using overlap sampling methods. *J. Comput. Chem.* **2004,** *25* (1), 28-40.
66. Kästner, J.; Senn, H. M.; Thiel, S.; Otte, N.; Thiel, W., QM/MM Free-Energy Perturbation Compared to Thermodynamic Integration and Umbrella Sampling: Application to an Enzymatic Reaction. *J. Chem. Theory Comput.* **2006,** *2* (2), 452-461.
67. Rod, T. H.; Ryde, U., Accurate QM/MM Free Energy Calculations of Enzyme Reactions: Methylation by Catechol O-Methyltransferase. *J. Chem. Theory Comput.* **2005,** *1* (6), 1240-1251.
68. Zhang, Y.; Liu, H.; Yang, W., Free energy calculation on enzyme reactions with an efficient iterative procedure to determine minimum energy paths on a combined ab initio QM/MM potential energy surface. *J. Chem. Phys.* **2000,** *112* (8), 3483-3492.
69. Ikeue, T.; Ohgo, Y.; Takahashi, M.; Takeda, M.; Neya, S.; Funasaki, N.; Nakamura, M., Bis(tetrahydrofuran)(2,7,12,17-tetrapropylpor- phycenato)iron(III) Perchlorate: A Pure Intermediate Spin Complex. *Inorg. Chem.* **2001,** *40* (14), 3650-3652.
70. Ohgo, Y.; Neya, S.; Ikeue, T.; Takahashi, M.; Takeda, M.; Funasaki, N.; Nakamura, M., Molecular Structures of Five-Coordinated Halide Ligated Iron(III) Porphyrin, Porphycene, and Corrphycene Complexes. *Inorg. Chem.* **2002,** *41* (18), 4627-4629.

Chapter 4

Method Development and Applications for Finding Reaction Pathway Including Intersystem Crossing

One of the most important tasks in the study of a chemical reaction is to figure out the mechanism. Finding out the reaction pathway, also known as MEP, and the corresponding TS is the key to unlock this problem. For the nonadiabatic processes such as photophysical and photochemical reactions, the conical intersection point is as well nonnegligible to explain the mechanism.[1-6] In the subsection 4.1, an example a work we cooperated with the experimental group related to the photochemical reaction will be introduced as another example. For such multiple states reactions, we would wonder if there is a convenient way to optimize ISC points. Subsection 4.2 would introduce out newly developed method for this question.

4.1 An application of a penalty function method to locate MEISC point.

4.1.1 Introduction

In the experiment, it was first time found that dibenzofulvene (DBF) can be formed by photo-induced dehydration of alcohols.[7] The 9-fluorenylmethanol (FM) is converted into DBF under the Xe lamp irradiation. This photo-induced reaction was found to be clean and efficient. The only product olefin can be the source material for other important functional vinyl compounds such as poly(DBF) which has π-stack conformation.[8-13] This new synthesis approach owns many

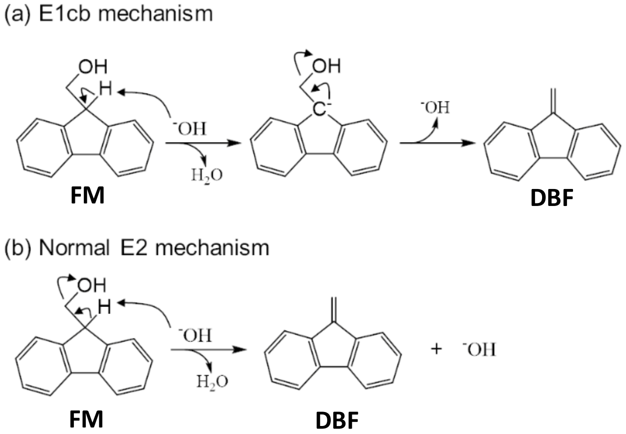

Figure 1 (a) An intermediate of carbanion is formed in E1cb mechanism. (b) A concerted E2 mechanism.

different features to the previous work.

In the previous work, similar process where DBF monomer was also obtained by FM conversion in the base environment was considered to happen in a elimination unimolecular conjugate base (E1cb) mechanism.[14-16] Another thing should be pointed out is, in the new synthesis method, base is not used. However, in the previous work, base was necessary. E1cb mechanism is a two-step mechanism as shown in Fig. 1(a). In the first step, hydroxy group grabs the hydrogen on the β-carbon, leading to the generation of carbanion. Then, the hydroxy group on the α-carbon leaves away, yielding the product of FM. Different from the E1cb mechanism, the product can be generated in a concerted way without appearance of carbanion in the normal E2 mechanism (see Fig. 1(b)).

Experimental results showed that the photo-induced β-elimination of FM to DBF could be a unimolecular reaction because the reaction rate is linearly growing according to the initial concentration of the FM. Because both E1cb and normal E2 mechanism are bimolecular process, they can‘t be used to explain this reaction. Besides, the type of solvent was found to influence the reaction rate greatly according to their dielectric constants. Reaction in the solvent with larger dielectric constant is slower. This effect of solvent is in the opposite order to the expected mechanism of previous work where the deprotonation reaction should be easier in the solvent with larger dielectric constant. [14-16] These evidences indicate the possibility of an E2 mechanism. On the other hand, it was observed that in the solvent with lower fluorescence efficiency, the rate constant was higher. Thus, the reaction may happen on the excited triplet state. Because the ground states of the reactant and the product are both singlet state, intersystem crossing could occur.

Considering the debates of the mechanism, it is necessary to investigate the reaction from the perspective of theorical view. Although it seems to be a unimolecular conversion reaction, in this section, the structural changes along the reaction will be introduced step by step. Also, different electronic states will be considered. Our computational results indicated that this reaction is not as simple as it seems to be and ISC plays a role. The computational details will be given in subsection 4.1.2. The results and discussion of the mechanism can be found in subsection 4.1.3.

4.1.2 Computational details

In this work, DFT method was adopted. Because excited states would also be studied, unrestrained B3LYP functional with 6-31g basis set were used for structures optimization and the energy evaluation. The difference of unrestrained functional and restrained functional lies in whether the spatial orbitals of α spin orbital and β spin orbital are forced to be degenerated, if not, it is unrestrained scheme. Unrestrained functional is more natural and precise description. The structure optimization was mainly conducted by using Gaussian09 software.[17] Some transition states were found by using GRRM program.[18, 19] The ISC point was optimized by using the code developed in our group.

4.1.3 Results and discussions

Calculated potential energy profile is shown in Fig. 2. The black line represents the energy surface of S_0 state, the red and the purple lines represent T_1 and S_1 state, respectively. Initially, the molecule is excited from the ground state of S_0 state to the first singlet excited state S_1 by Xe lamp irradiation. S_1 state is less stable than the ground state by 109.5 kcal/mol. At this structure, the energy of T_1 state is in between the two singlet states. By slightly structure relaxation, the molecule reaches the local minima of S_1 state. From S_0 minima to S_1 minima, the structure becomes different mainly because the single bond connection of the 9-position carbon around the -CH₂- group is rotated. Next, only 14.0 kcal/mol energy is needed to across an energy barrier on the T_1 surface. In this process, the same C-C single bond is rotated more and the bond length of C-O is enlarged, leading to the generation of an OH radical and a 9-fluorenylmethyl radical. This step is the rate-determining step in this reaction. Then, the position of OH radical is

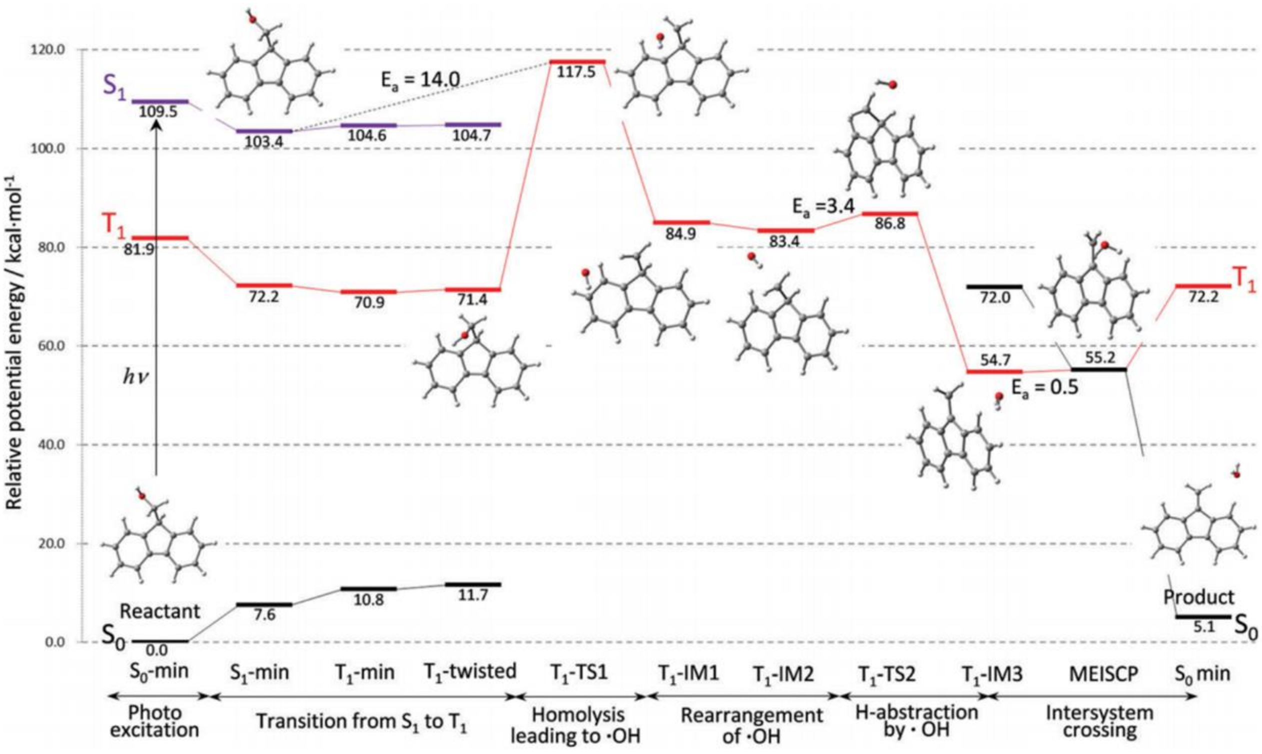

Figure 2 Proposed mechanism of the photo-induced β -elimination of 9-fluorenylmethanol leading to dibenzofulvene. Numbers and E_a denote relative potential energies and activation energy in kcal/mol, respectively. MEISCP stands for the minimum energy intersystem crossing point.

rearranged. We found there is interaction between the OH radical and the hydrogen at 1-position of the fluorene back bone in rearranged structures (T_1-IM1 and T_1-IM2). This kind of interaction was thought to be the weak hydrogen-bonding interaction. After the arrangement, through another transition state (T_1-TS2) where the energy barrier is as small as 3.4 kcal/mol, the OH radical takes away the hydrogen at the 9-position, leading to the formation of product DBF (T_1-IM3). At this time, the product is on the minima of triplet state which is more stable than the S_0 state by 17.3 kcal/mol and the methylene unit in DBF is perpendicular to the fluorene backbone in the triplet state. However, this is not the most stable minima. Along with the methylene unit rotating to the planar of fluorene backbone, one MEISCP was found and yields the most stable product in S_0 state. From the triplet local minima (T_1-IM3) to the MEISCP, only 0.5 kcal/mol is needed. The singlet product is more stable than T_1-IM3 by 49.6 kcal/mol. The product is a little less stable than the reactant by 5.1 kcal/mol. Thus, this is an endothermic reaction.

Because there is a homolysis step of the C-O bond to generate OH radical and this radial finally takes away the hydrogen on the neighbor carbon, this reaction is considered occur through an E2 mechanism. However, it should be noticed that this reaction is different from the normal E2 mechanism because usually strong base environment is required in the normal E2 mechanism, but in this reaction no base was used. It should be noted that, the generated OH radial takes the role of $^{-}$OH. We don't think it is the E1cb mechanism because not only there was no base but also no carbanion was generated in the reaction pathway. On the other hand, basing on the experiment affect that the appearance of radical scavenger did not influence the rate constant, the lifetime of the OH radical and 9-fluorenylmethyl radical may be too short in the concerted E2 reaction so that these two radicals have less chance to collide with the radical scavenger.

As we mentioned before, in the solvent with larger dielectric constant the reaction rate is smaller. This can be explained in terms of mobility of the reactive species. There is possibility that OH radical has interaction with MeOH or CH_3CN or H_2O through hydrogen-bonding and/or dipole-dipole interactions. Consequently, OH radical have lower mobility in the polar solvents, leading to the less efficiency in the rearrangements in formation of T_1-IM1 and T_1-IM2, as depicted in Fig. 2.

Our results calculated by DFT mechanism is opposite to the expect of references where the fluorene derivatives[20-25] and benzylalcohol derivatives are predicted to form an iron or radical on the carbon atom at the benzylic position which is stabilized by conjugation with aromatic system. In this calculation, however, the homolysis of the C-O bond of FM is confirmed. Considering DFT method have been used to successfully interpret radical reactions,[26, 27] we believe the results are trustable.

4.1.4 Conclusions

In this work, a new approach to synthesize dibenzofulvene by using 9-fluorenylmethanol was proposed. Different from traditional E1cb mechanism in similar reactions, the photo-induced β-elimination of FM was found to go through E2 mechanism. Experimentally, this mechanism is supported by the effects of solvent and the observation of the reaction rate. Theoretically, the DFT calculation results also suggested the E2 mechanism because the OH radical take a role in the reaction and no carbanion was generated. Besides, the homolysis of C-O bond on the FM was predicted by DFT calculation. This is the opposite result as expected in the previous work.

4.2 Nudged elastic band method development for multiple states reactions

4.2.1 Introduction

The configuration of the minimal energy conical intersection point is of great importance because it opens an effective and efficient way for nonradiative transition.[28] Spin-forbidden reactions, which are ubiquitous in transition metal compounds involved reactions, is subject to the conical intersection. MEISCPs in spin-forbidden reactions have attracted lots of scientific concern because of the key roles in the reaction pathways.[29-35] Many researches have revealed that these spin-changes can either accelerate the reactions or induce the reaction barriers.[36-38] The determinations of spin crossing geometries help to investigate the reaction mechanism, explain the experimental phenomenon, and sometimes estimate the reaction rate.[29, 36, 39, 40]

Methods for locating the conical intersections can be classified into three, known as Lagrange multiplier method,[30, 41, 42] gradient projection method,[43] and penalty function method.[44, 45] These methods have their own advantages and disadvantages.[46] Among the three, penalty function method is quite useful when the two state intersect coupling vectors are unavailable,[46, 47] for example when the computational model is large or the electronic method can’t calculate more than one electronic state simultaneously.[28, 48] There are two typical penalty functions proposed by Ciminelli et al.[44] and Martinez et al.,[45] respectively. Maeda et al. also used a simpler form of Martinez type penalty function.[49] When applying penalty function method, one needs to prepare an initial structure that is better to be close to the real MEISCP, not only to save the computational resources but also to improve the degree of accuracy. Actual ISCs constitute a multidimensional seam on the potential surface. The optimized structure depends largely on the initial guess. For a spin crossing reaction, it is not straightforward to prepare a proper starting point that leads to the MEISCP.

A significant number of computational methods have been developed to calculate TS. The mostly used methods can be divided into three groups basing on the initial conditions. A class of methods such as Newton-Raphson and quasi-Newton method starts from a proper guess of TS.[50,

[51] Methods like isopotential searching method start from the reactant.[52] The third class of methods begin with structures of reactant and product. Among the third type, nudged elastic band (NEB) method is one of the most widely used one.[53] Since the original NEB method was developed, different variants were proposed to extend its applicable fields. Climbing image NEB (CI NEB) and improved tangent estimate NEB (IT NEB) were proposed in the same period.[54] The former method made a small change to the image with highest energy. This climbing image doesn't feel spring force but optimized towards TS. So that, CI NEB can yield TS while finding MEP without extra computational costs. IT NEB highlighted a new way to estimate tangent. New tangent was said to be more stable and can help to eliminate the problem with kinks. There were also methods developed for improving the accuracy near TS by maintaining the proper density of images. Adaptive NEB (ANEB) and free-end NEB (FENEB) method were proposed for this problem.[55] Recently, a combination of these two methods was published.[56] Another direction for the improvement is to accelerate the NEB calculation. Peterson introduced the machine learning into NEB method while Koistinen and coworkers adopted the strategy to use gaussian process regression.[57, 58] All the improvements of NEB method made until now were developed basing on a single spin surface MEP searching.

As we have mentioned, the determination of ISC bares another serious problem in addition to those of TS. Although our chemical intuition can give an initial guess to the TS, it is hard to do so for the ISC. Maeda and coworkers have a strategy to find all of the available crossing points by combining a penalty function method and automated search methods such as global reaction route mapping (known as GRRM) and artificial force induced reaction (noted as AFIR).[59] On the other hand, we are interested in finding crossing points in the course of reaction pathway. In this work, we will apply a penalty function method to NEB method so that ISC points can be automatically located while optimizing the reaction pathway. In the next subsection, a simple review about traditional NEB method will be given. Then the algorithm about multiple states NEB (MS NEB) method will be discussed. The computational details about testing examples will be stated in the third subsection. The fourth subsections will show the results we tested.

4.2.2 NEB method

NEB method is a two-ending controlled method. By using optimized structure of reactant ($\vec{R}_0$) and product ($\vec{R}_{N+1}$), a set of intermediate images $\{\vec{R}_i | i \in [1, N]\}$ can be generated as the initial guess, where $\vec{R}_i$ represents cartesian coordination of image i. Then, these images would be optimized iteratively under the influence of both electronic potential and spring potential. This spring force is applied to avoid the sliding into a minimum.

Linear interpolation (LI) method or improved dependent pair potential method are available for initial guess.[60] In this work, LI method was adopted. The coordinate of image i is generated by

$$r_\alpha^i = r_\alpha^0 + (r_\alpha^{N+1} - r_\alpha^0) \times i/(N+1), \tag{1}$$

where N represents the total number of images. r_α^0, r_α^i, and r_α^{N+1} $(\alpha = x, y,$ or $z)$ are the cartesian coordinates of reactant, image i, and product, respectively.

The object function of NEB method, $S(\{\vec{R}_i\})$, is consisted of potential energy and spring energy.

$$\mathrm{S}\big(\vec{R}_0, \dots, \vec{R}_{N+1}\big) = \sum_{i=1}^{N} V\big(\vec{R}_i\big) + \sum_{i=1}^{N+1} k_i/2 \times (\vec{R}_i - \vec{R}_{i-1})^2 \,, \tag{2}$$

where k_i is a spring constant. The first term represents for the accumulation of potential part and second term is the sum of spring energy. To avoid the corner cutting problem or sliding problem,[61] only the parallel component (or say, the component parallel to the reaction pathway which is defined by tangent) of the true force and the perpendicular component of the spring force are adopted.

$$\vec{F}_i = -\nabla V(\vec{R}_i)|_{\perp} + \vec{F}_i^S|_{\parallel}\,, \tag{3}$$

where $\perp$ means perpendicular component and $\parallel$ means parallel component. See Fig. 3 for the direction of the vectors.

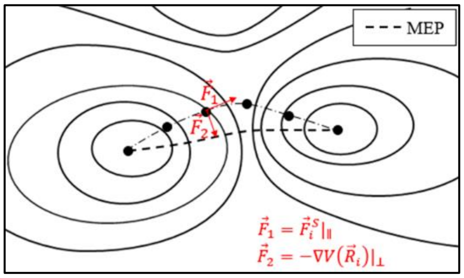

Figure 3 The direction of forces in equation (3).

Climbing image (CI) NEB method is a good choice if we want to locate TS at the same time. The image energetically on the top of the reaction pathway is optimized towards TS by using force

$$\vec{F}_{E_{max}} = -\nabla V(\vec{R}_{E_{max}}) + 2\nabla V(\vec{R}_{E_{max}})|_{\parallel} \tag{4}$$

Considering the benefits of IT NEB, we used this method as a good estimation of tangent in this work. For more details of the tangent, please refer to the reference.[62]

4.2.3 Multiple spin states NEB method

Our group had experience of calculating the reaction systems related to ISC.[7, 63-67] ISC points were found crucial to explain the experimental phenomena. Inspired by CI-NEB method, MS NEB method is designed to locate ISC point together with normal NEB strategy. For simplicity, only two-state reactions will be discussed. This method, however, can be generalized for systems with more complicate multiple spin states.

The initial setting-up is the same as normal NEB method. After the initial guesses are given, images will be optimized on the more stable spin surface. Spin multiplicity for each image is determined by comparing the single point energy of each spin state.

In MS NEB optimization, the force acts on the image with highest energy is same as CI NEB, shown in equation 4. If the spin multiplicity is changed between two images, one of the two can be optimized as ISC point. The object function for the ISC image is

$$\mathrm{S}(\vec{R}_i) = (V_I(\vec{R}_i) + V_J(\vec{R}_i))/2 + \sigma \Delta {V_{IJ}}^2/(\Delta V_{IJ} + \alpha), \tag{5}$$

where I or J refer to the higher and the lower spin state, respectively. ΔV_{IJ} is the positive energy difference between two states. The parameters σ and α are defined as in the previous work.[45] Consequently, the force is

$$\vec{F}_{ISC} = -\left(\nabla V_I + \nabla V_J\right)/2 + \sigma(\Delta V_{IJ}^2 + 2\alpha \Delta V_{IJ})/(\Delta V_{IJ} + \alpha)^2 \times (\nabla V_I - \nabla V_J), \tag{6}$$

where α and σ are constant parameters. The mathematical roles of α and σ are discussed in the original paper.[45]

The major procedures of MS-NEB method can be summarized in a flow chart as shown in Fig. 4(a). In more details, the following steps were processed:

1. Initial settings: input initial geometric information (the optimized reactant and product) and the convergence conditions. In the following iterations, the displacement of each atom will be calculated by using mass-weighted cartesian coordinates. The total distance is the sum of these displacements. One image is considered to be converged if the total distance is less than 0.0001 Bohr.
2. Generate images: generate coordinates of intermediate images by LI method.
3. (Optional)Pre-optimization for several iterations (In this work, it is set as 5).
   3-1. First, carry out SCF calculation for each spin state of each image.
   3-2. Determine the multiplicity by comparing the energy. Use the force of the most stable spin

state to optimize the images, where the force was given by equation 3.

  3-3. Exit if the convergency conditions (same criteria as mentioned in step 1) are met or the max number of iterations is reached. Or, go back to step 3-1.

4. (Optional)Redistribute images. If the energy difference of image 1 and reactant is smaller than the certain threshold (in this work, the threshold is 0.003 a.u.), then the image 1 will be discarded, and a new image will be generated in between the image of the highest energy and its former image as in the LI method (see Fig. 4(b)). The same process is done between image N and the product. This step is intended to improve the image density around TS.
5. Main MS NEB optimization iterations.

  5-1. SCF calculations are done as in step 3-1.

  5-2. The images are divided into three groups as illustrated in Fig. 5(b). The one with highest energy is optimized with CI-NEB method by using the force of the most stable spin state. The one chose as the candidate of ISC point is optimized with equation 6. The rest are optimized by equation 3.

  5-3. Check the converged image numbers. If all the images are converged, the NEB optimization is normally finished. Else, repeat step 5.

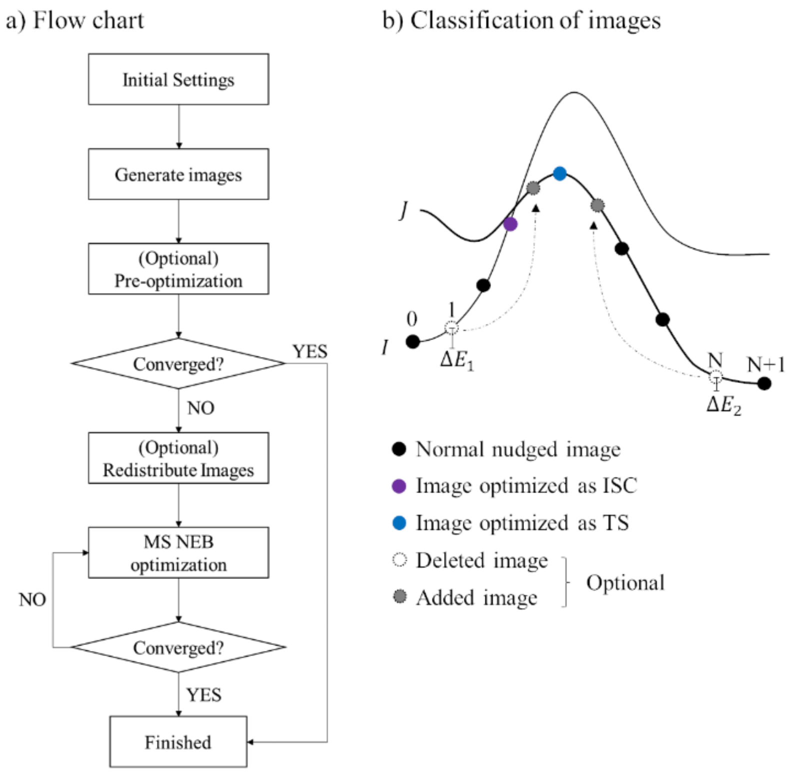

Figure 4 (a) Flow chart of the algorithm of MS NEB method; (b) Classification of images. States J and I have different spin multiplicity. The purple image will be optimized towards ISC, the blue image will be optimized to TS while the black images will be nudged. If the energy difference (ΔE_1) between image 1 and 0 is small enough, image 1 will be discarded and another image will be generated before TS. Same will be done to image N.

The pre-optimization is meant to give more reasonable initial structures for the special images. The step 4 helps to avoid the waste of efforts on the area near the flat minimums and increase the accuracy around TS. These two steps are, however, optional. In the main optimization step, selections of an image for ISC point should be very carefully done.

4.2.4 Computational details

We adopted density functional theory (DFT) for all the calculations. Exchange-correlation functionals and basis sets depend on the system. In the first example, C-C bond rotation of ethylene, the B3LYP functional with 6-31G* basis set was used for all the elements. In the second example, the ωB97XD functional was adopted. Stuttgart/Dresden basis set was used for In where 46 core electrons were replaced by the effective core potentials (ECPs), and the 6-31G* sets for the others. Choice between a closed shell and an open shell calculation depends on the molecule's spin state in two examples. The last example is a more complicated case where ISC happened twice in one reaction. Zhang and coworker studied the methane activation by MH^+ (M = Fe, Co, and Ni) both experimentally and theoretically.[68] According to their result, all the three cases went through ISC point twice. We tested CoH^+ as the example. To keep consistency of the results, we adopted the same DFT functional and basis set as Zhang's work. In their study, unrestricted B3LYP functional was used. As for the basis set, cc-pVTZ was applied for carbon and hydrogen. (14s9p5d)/[8s4p3d] Wachters basis with two diffuse p functions, one diffuse d function, and a (3f)[1f] polarization function was employed for cobalt. All the potential force was generated by Gaussian 09 program package.[69] A quasi-Newton scheme, BFGS,[70] was implemented for the NEB optimizer. The step size was evaluated by line search method. Except for the last example where the spring constant k_i is 0.5, the spring constant of 0.1 was used. We adopted 0.02 for the α (Equation 5) in all the examples. The σ values, which controls the energy gap, were different depending on cases. It will be explained in each example

4.2.5 Benchmark calculations

A. C-C double bond rotation of ethylene

For the first and simplest example, the rotation of C-C double bond of ethylene was tested. Initially, the four hydrogen atoms are planarly oriented as the equilibrium structure of ethylene. In this case a closed-shell singlet state is the ground state. Along with C-C double bond is rotated until one CH_2 group becomes vertical to the other, two parallel 2p orbitals also become vertical in the final state, leading to the two 2p electrons unpaired.

According to the intrinsic reaction coordinate (IRC) calculation, as the dihedral angle increasing from 0 to 90 degrees, the energy of singlet state continuously grows up while the energy of triplet decreases. In MS NEB calculation, this tendency can be displayed in just one calculation as shown in Fig. 5. Image 9 (whose dihedral angle is 72.0°) was automatically appointed to find the minimum energy ISC point. With the σ value of 3.5 (see equation 5), calculated energy gap of two spin states was 5.7 kcal/mol. The energy gap dropped to 4.1 kcal/mol when a larger σ value (σ = 10) was used without much structural change of the other images. When σ value became even larger (σ = 30), the degeneracy can be much improved within the gap of 0.1 kcal/mol. The dihedral values of ISC points calculated with σ = 3.5, 10, and 30 are 72.0, 72.3, and 72.3 degrees, respectively. The bond lengths in the same order are 1.38, 1.39, and 1.45 Å, respectively. Obviously, the geometries optimized with smaller σ value are geometrically near to the refined ISC point (σ = 30). The relatively energy of the three are 0.0, 0.5, and 2.5 kcal/mol, respectively, which also shows the similarity.

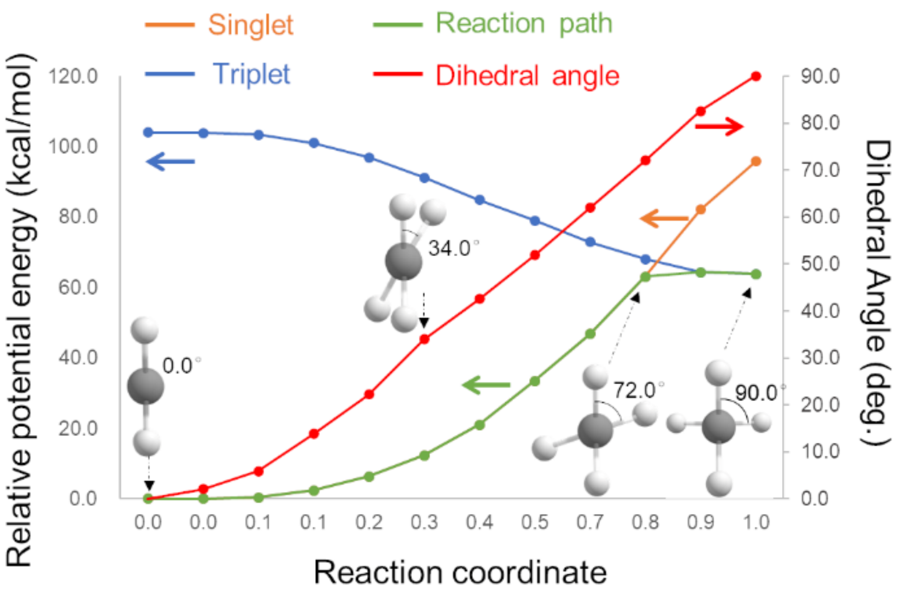

Figure 5 Relative potential energy profile of ethylene C-C double bond rotation obtained by MS NEB method.H-C-C-H dihedral angle changes are represented by the red line.

B. In-catalyzed C-H bond activation

In our previous study, intersystem crossing was found in C-H bond activation of methane catalyzed by In_2.[71] At the reactant side, methane and In_2 were close to each other under intermolecular interaction. Because the ground state of In_2 is in triplet state, the reactant state has triplet multiplicity. After In_2 takes one hydrogen atom from the methane, homolytic dissociation of the C-H bond leads to two unpaired electrons which couple with those of In_2. Thus, singlet state is more favorable in the product state. Different spin states of the reactant and product states indicate the existence of ISC point.

MS NEB calculated reaction pathway with 9 intermediate images is presented in Fig. 6(a). Only image 4 was optimized as a transition state while other points were treated as normal nudged images. Image 4 had the highest energy in the singlet state. At the same time the spin change also happened in between image 3 and 4, and the energy gap at image 4 is smaller than that of other images. In a word, image 4 was found to be the nearest point to both TS and ISC point. In this case, we put a higher priority on TS optimization because TS should be in MEP. What is interesting in Fig. 6(a) is, although image 4 was only optimized as TS, the energy gap is still smallest at this point which is only 2.3 kcal/mol. That means the ISC can happen together with or at least near this TS. The structure information of important images can be found in Fig. 7

As discussed, there was no image optimized towards ISC point in the last calculation because of its coupling with the saddle point. In order to have a more precise ISC point, we made a little change to the strategy of optimization. If one image meets the criterion of being both TS and ISC point, then it will be optimized as the TS while the neighbor will be optimized towards the ISC point. Because the energy change from image 3 to image 4 is large in Fig. 6(a), we also increased the number of images to 10. The resulting energy profile is presented as Fig. 6(b) which

(a) Intermediate image number equals to 9

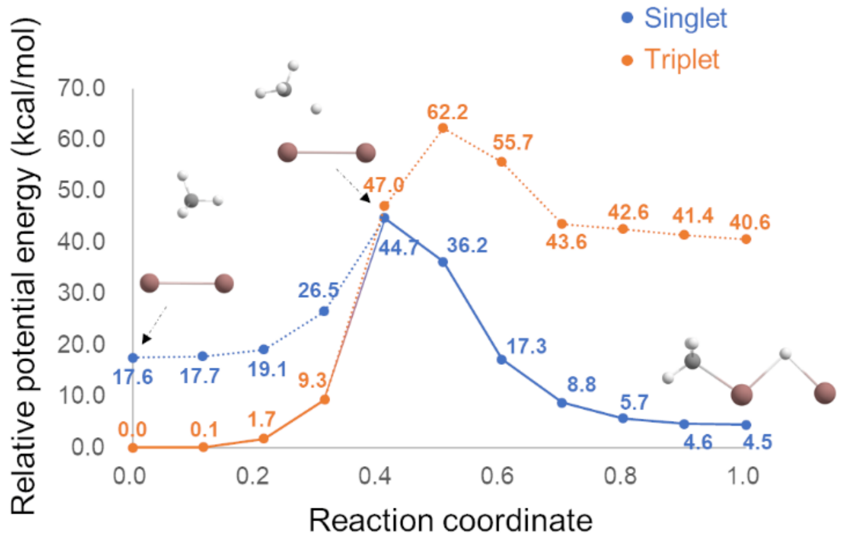

(b) Intermediate image number equals to 10

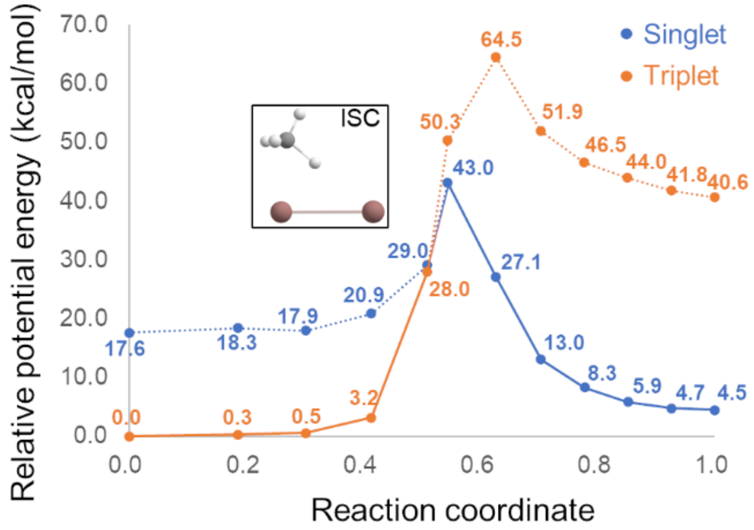

Figure 6 (a)Relative potential energy profile of In_2-catalyzed C-H bond activation with 9 intermediate images (No image was optimized as ISC point). (b) Relative potential energy profile of In_2-catalyzed C-H bond activation with 10 intermediate images (One image was optimized as ISC point).

keeps similar tendency to Fig. 6(a). Besides, one ISC structure was optimized with an acceptable energy gap (1.0 kcal/mol). In this calculation, the σ value was set to 10.0. Because the degeneracy was already small enough, we didn't try another ISC optimization for the refinement. In Fig. 6, two ISC points were energetically different by around 17 kcal/mol. For the former calculation, we can expect an ISC point around 44 kcal/mol but in the later calculation it is only 28 kcal/mol. This suggested that the singlet and the triplet energy surfaces are close to each other within a certain reaction coordinate range.

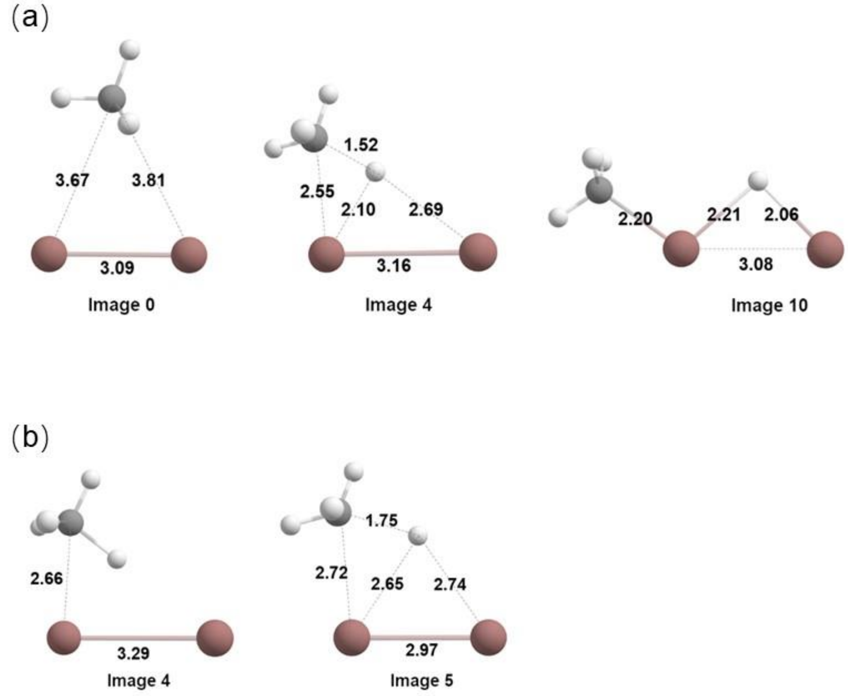

Figure 7 (a) Structural information of image 0, image 4, and image 10 in Figure 6(a). (b) Structural information of image 4 and image 5 in Figure 6(b). The unit is in angstrom.

There is the possibility that the ISC is not the minimum energy ISC, because the CI-NEB calculation with limited image density did not yield tightly converged TSs.[54, 55, 72] An improved transition structure can drag other images nearer to the reaction pathway. Thus, if there is the demand for high precision of the ISC structures, the better TS geometries are required. Instead of optimizing TS and ISC points simultaneously, MS NEB can be revised into TS optimization and ISC points location two steps.

There are different approaches to improve the TS. ANEB method or two climbing image NEB (C2-NEB) methods can be combined with MS NEB method to find more accurate saddle points.[55, 73] With a reliable TS, both reactant-TS and TS-product pathways are two two-ending pairs to run MS NEB without climbing. Obviously, a larger computational resource is needed to achieve this algorithm. Because we focused on applying NEB method in a spin-forbidden reaction, no extra effort was put on how to refine a better TS. We simply used Gaussian09 to re-optimize the TS structure. With fully optimized reactant, TS, and product, the reaction pathway was revised as Fig. 8. Image 5 was optimized as the ISC point with a gap of 1.7 kcal/mol. Image 4 was dragged to approach the crossing region by spring force thus the energy gap is as small as 1.9 kcal/mol. Comparing with Fig. 6(b), in Fig. 8 there is a small barrier before the transition state. This is because the images before the ISC points were optimized on the triplet surface. There are complicated multiple dimensional reaction coordinates such as the C-H bond distance, the In-In distance, the C-In distance, the H-In distance and so on. It is hard to draw a figure that display all the changes along all these directions. We chose two dimensions, the C-In2 and the H-In1 (see Fig. 9) distances to show that the images in Fig. 6(b) and Figure 8 have different reaction coordination. Thus, there is a small energy barrier in Figure 5 singlet surface before the transition state which is

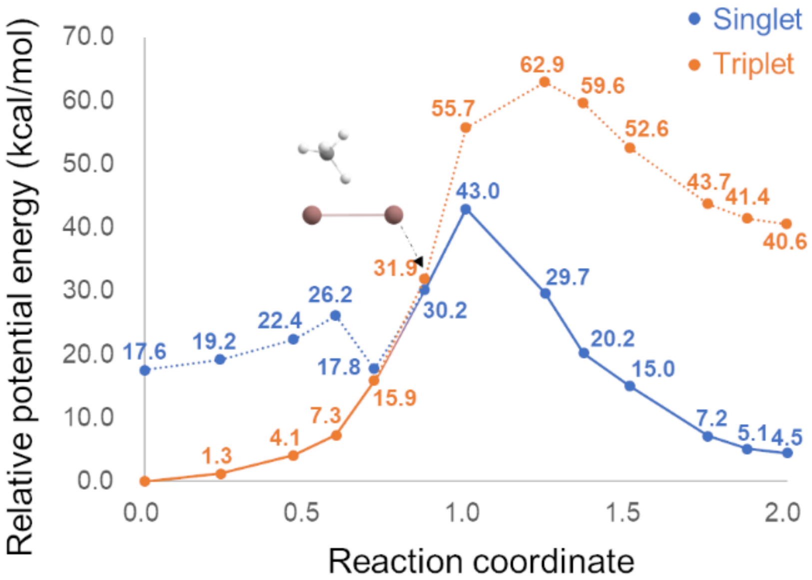

Figure 8 The result of stepwise MS NEB. Image 5 was optimized as the ISC.

not found in Fig. 6(b). Fig. 9 shows that the reaction pathways in two figures were represented by the points with different reaction coordinates. In this case, ISC point located by stepwise MS NEB (30.2 kcal/mol) and normal MS NEB (28.0 kcal/mol) are energetically similar, suggesting the effectiveness of normal MS NEB. When the geometry predicted by normal MS NEB method is poor, then stepwise MS NEB is better choice to optimize ISC points.

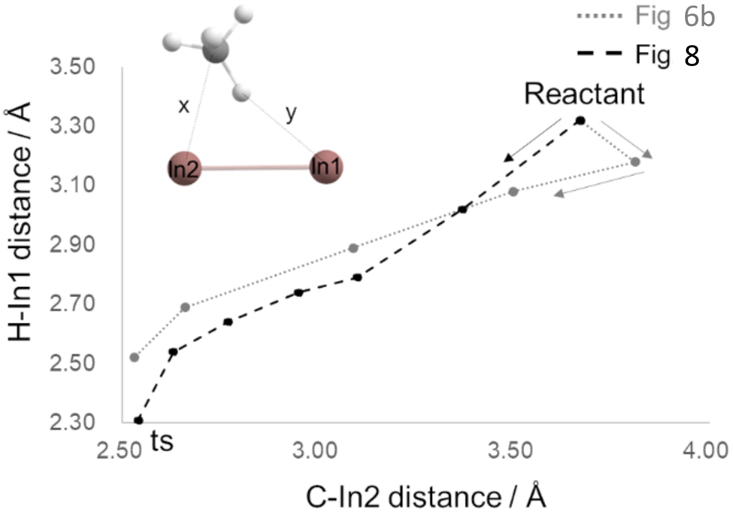

Figure 9 From the reactant to the transition state, two-dimensional reaction coordinates of images in Figure 6(b) and Figure 8.

C. Activation of methane by CoH^+

We also applied the MS NEB to a more complicated reaction

$$CoH^+ + CH_4 \rightarrow CoCH_3^+ + H_2.$$

According to DFT calculations by Zhang and co-worker,[68] a high spin state is the ground state at both reactant and product configuration, while the low spin state is more stable near TS region. Consequently, two ISC points are expected in the reaction pathway.

For the cases where intersystem crossing may occur more than once along the reaction pathway, the images for optimization of ISC points should be chosen more carefully. In the last subsection, two-image-selection strategy was adopted. An image would be optimized as an ISC point, if the neighbor image is the climbing image and has different multiplicity. An image is also a candidate for ISC point, if the nudged image has different spin states and also has a smaller energy gap. However, this two-image-selection strategy failed in this example because unnecessarily many special points could be located. These spring force-free images can lead to a reaction pathway far from the MEP.

To limit the number of ISC images, we proposed a three-image-selection scheme as shown in Fig. 10. Two cases would be recognized as ISC points. In case 1 (Fig. 10(a)), spin change is happened in between image i and i-1 while spin states are the same for image i and i+1. In addition, the energy gap at image i should be smaller than that of image i-1. In case 2 (Fig. 10(b)), spin states are different between image i and i+1 but keep the same between image i and i-1. Besides, image i has a smaller energy gap than image i+1. On the other hand, there is the case where image i won't be optimized as ISC point. As shown in Fig. 10(c), the spin states of image i-1 and i+1 are the same but different from image i. It is assumed that the step size is small enough that intersystem crossing is difficult to happen continuously. Of course, there could be the situation that two spin surfaces are crossing at a certain point like Fig. 10(d). However, this is the limited cased. On the other hand, because one spin surface is always lower except for the crossing point, the spin crossing

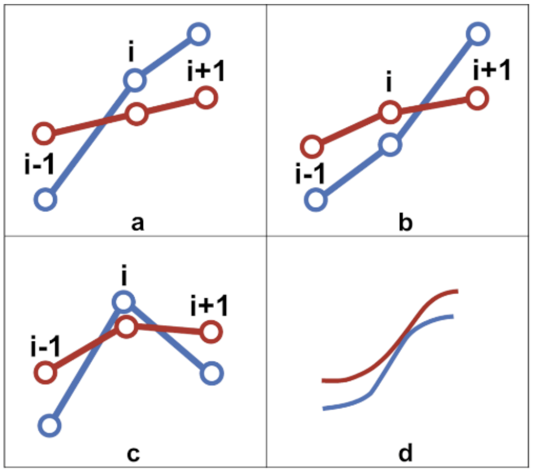

Figure 10 Three-image-selection scheme for defining ISC points. In the case of (a) and (b), image i will be recognized as ISC point. In case of (c), image i will be nudged.

is less likely to happen. Thus, it is reasonable to omit such crossing point. In the final calculation, this stricter scheme limited exactly two images to be ISC points (image 3 and image 9 in Fig. 11).

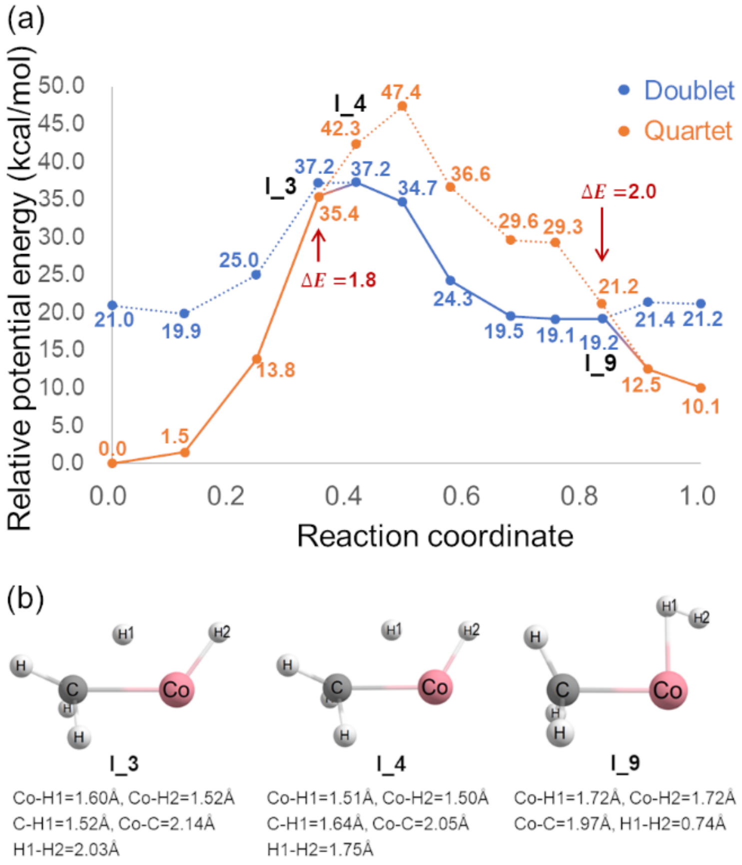

Figure 11 (a) Reaction pathway of CoH^+ catalyzed methane activation (two images, I_3 and I_9, were optimized as ISC point). (b) Geometric information of important images.

As a comparison, the reaction pathway calculated by the two-image selection scheme is shown in Fig. 12. In the early iterations, the spin crossings were found between image 4 and image 5, image 9 and image 10. Although the energy gap of different spin states at image 5 was smaller than at image 4, the image 5 was optimized towards transition state. Instead, image 4 was chosen as the candidate as the ISC point. Thus, there were three spring-force-free images, one candidate of transition state (image 5) and two ISC candidates (image 4 and 9). In the later interactions, image 3 was found more stable in the doublet state. Because of the small energy gap at image 3, according to the two-image-selection scheme, image 3 was also optimized as the ISC points. From Fig. 12 we can see, the image 2 and image 4 were more stable on the quartet state. In the three-image-selection scheme, image 3 can be attributed to case (c) in Fig. 12, which won't be optimized ISC point. In short, in the later iterations there were one image for transition state (image 5) and three images for ISC points (image 3, image 4, and image 9). The final energy gap at image 4 is large because the initial structure of image 4 is far from the spin crossing point thus after the maximum optimization steps reached it hadn't been driven to the crossing point.

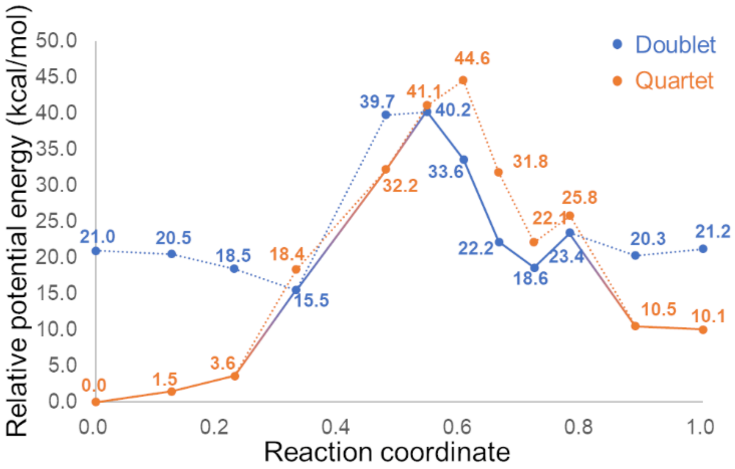

Figure 12 Relative potential energy profile of CoH^+-catalyzed methane activation. Calculated by using two-image-selection scheme.

Comparing the results of Fig. 11 and Fig. 12, the reaction pathways after image 7 are similar to a certain degree. Fig. 13 shows the comparison of structures after image 7. The images in two reaction pathways are alike structurally and energetically indicating that they attended to converge to the same reaction pathway. In this region, there is only one spring force-free image (image 9) which suggests that with the spring force helps to converge to ISC. On the other hand, before image 7, there are 3 spring force-free images and their structures in Fig. 11 and Fig. 12 are much different.

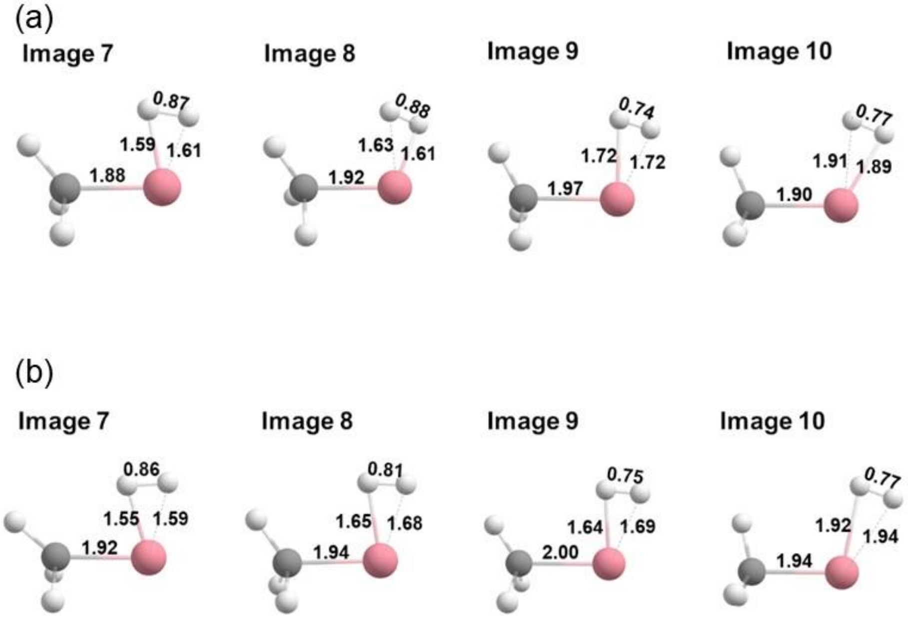

Figure 13 Comparison structures from image 7 to 10 in Figure 11 and Figure 12. The unit is in angstrom. (a) Structures in Fig. 11. (b) Structures in Fig. 12.

4.2.6 Conclusions

In this work, we expanded the application of NEB method to multi-spin systems. Here we propose MS NEB method to solve the difficulty in defining an initial structure for optimization of ISC point. The MS NEB method can also automatically search out the MEISC points and saddle point while finding the MEP. This new method predicted reasonable results for the three benchmark calculations even in complicated case where more than one MEISC points were located. The second and third examples suggest that the image type definition should be especially careful. Whether two-image selection scheme or three-image scheme is used should depend on case. According to our experience, if there the intersystem crossing happens only once, two-image-selection scheme performs better. If more than one ISC points are expected, a relatively stricter standard, three-image-selection scheme should be used. Besides, more precise ISC point and MEP can be obtained by optimizing TS and ISC point separately. In most cases, the normal MS NEB is enough to evaluate the geometry of ISC point and TS. However, if the program can't yield a good structure of TS, the stepwise MS NEB is suggested. Correspondingly, stepwise MS NEB method usually requires more computational cost. On the other hand, although we applied the MS NEB only to the two-state system, it is possible to be expanded to more states system by modifying the penalty function.

References

1. Robb, M. A.; Bernardi, F.; Olivucci, M., Conical intersections as a mechanistic feature of organic photochemistry. *Pure Appl. Chem.* **1995,** *67* (5), 783.
2. Yarkony, D. R., Diabolical conical intersections. *Reviews of Modern Physics* **1996,** *68* (4), 985-1013.
3. Yarkony, D. R., Current Issues in Nonadiabatic Chemistry. *J. Phys. Chem.* **1996,** *100* (48), 18612-18628.
4. Yarkony, D. R., Conical Intersections: Diabolical and Often Misunderstood. *Accounts of Chemical Research* **1998,** *31* (8), 511-518.
5. Yarkony, D. R., Conical Intersections: The New Conventional Wisdom. *J. Phys. Chem. A* **2001,** *105* (26), 6277-6293.
6. Levine, B. G.; Martínez, T. J., Isomerization Through Conical Intersections. *Annu. Rev. Phys. Chem.* **2007,** *58* (1), 613-634.
7. Nageh, H.; Zhao, L.; Nakayama, A.; Hasegawa, J.-y.; Wang, Y.; Nakano, T., Photo-induced β-elimination of 9-fluorenylmethanol leading to dibenzofulvene. *Chem. Commun.* **2017,** *53* (60), 8431-8434.
8. Nakano, T.; Takewaki, K.; Yade, T.; Okamoto, Y., Dibenzofulvene, a 1,1-Diphenylethylene Analogue, Gives a π-Stacked Polymer by Anionic, Free-Radical, and Cationic Catalysts. *J. Am. Chem. Soc.* **2001,** *123* (37), 9182-9183.
9. Nakano, T.; Yade, T., Synthesis, Structure, and Photophysical and Electrochemical Properties of a π-Stacked Polymer. *J. Am. Chem. Soc.* **2003,** *125* (50), 15474-15484.
10. Nakano, T.; Nakagawa, O.; Tsuji, M.; Tanikawa, M.; Yade, T.; Okamoto, Y., Poly(2,7-di-n-pentyldibenzofulvene) showing chiroptical properties in the solid state based purely on a chiral conformation. *Chem. Commun.* **2004,** (2), 144-145.
11. Nakano, T.; Yade, T.; Fukuda, Y.; Yamaguchi, T.; Okumura, S., Free-Radical Polymerization of Dibenzofulvene Leading to a π-Stacked Polymer: Structure and Properties of the Polymer and Proposed Reaction Mechanism. *Macromolecules* **2005,** *38* (20), 8140-8148.
12. Tamaki, N.; Tohru, Y.; Masaaki, Y.; Norio, N., Charge Transport in a π-Stacked Poly(dibenzofulvene) Film. *Chem. Lett.* **2004,** *33* (3), 296-297.
13. Nakano, T., Synthesis, structure and function of π-stacked polymers. *Polym. J.* **2010,** *42* (2), 103-123.
14. O'Ferrall, R. A. M.; Slae, S., The reaction of 9-fluorenylmethanol with base: a carbanion mechanism of β-elimination. *J. Chem. Soc. D* **1969,** (9), 486-487.
15. O'Ferrall, R. A. M.; Slae, S., β-Elimination of 9-fluorenylmethanol in aqueous solution: an E1cB mechanism. *J. Chem. Soc. B* **1970,** (0), 260-268.

16. O'Ferrall, R. A. M., β-Elimination of 9-fluorenylmethanol in solutions of methanol and t-butyl alcohol. *J. Chem. Soc. B* **1970,** (0), 268-274.
17. Frisch, M. J.; Trucks, G. W.; Schlegel, H. B.; Scuseria, G. E.; Robb, M. A.; Cheeseman, J. R.; Scalmani, G.; Barone, V.; Petersson, G. A.; Nakatsuji, H.; Li, X.; Caricato, M.; Marenich, A.; Bloino, J.; Janesko, B. G.; Gomperts, R.; Mennucci, B.; Hratchian, H. P.; Ortiz, J. V.; Izmaylov, A. F.; Sonnenberg, J. L.; Williams-Young, D.; Ding, F.; Lipparini, F.; Egidi, F.; Goings, J.; Peng, B.; Petrone, A.; Henderson, T.; Ranasinghe, D.; Zakrzewski, V. G.; Gao, J.; Rega, N.; Zheng, G.; Liang, W.; Hada, M.; Ehara, M.; Toyota, K.; Fukuda, R.; Hasegawa, J.; Ishida, M.; Nakajima, T.; Honda, Y.; Kitao, O.; Nakai, H.; Vreven, T.; Throssell, K.; Montgomery, J. A.; Jr.; Peralta, J. E.; Ogliaro, F.; Bearpark, M.; Heyd, J. J.; Brothers, E.; Kudin, K. N.; Staroverov, V. N.; Keith, T.; Kobayashi, R.; Normand, J.; Raghavachari, K.; Rendell, A.; Burant, J. C.; Iyengar, S. S.; Tomasi, J.; Cossi, M.; Millam, J. M.; Klene, M.; Adamo, C.; Cammi, R.; Ochterski, J. W.; Martin, R. L.; Morokuma, K.; Farkas, O.; Foresman, J. B.; Fox, D. J. *Gaussian 09 Rev. B.01*, Wallingford, CT, 2016.
18. Maeda, S.; Harabuchi, Y.; Osada, Y.; Taketsugu, T.; Monokuma, K. http://grrm.chem.tohoku.ac.jp/GRRM/ (accessed April 22, 2017).
19. Maeda, S.; Ohno, K.; Morokuma, K., Systematic exploration of the mechanism of chemical reactions: the global reaction route mapping (GRRM) strategy using the ADDF and AFIR methods. *Phys. Chem. Chem. Phys.* **2013,** *15* (11), 3683-3701.
20. Donckt, E. V.; Nasielski, J.; Thiry, P., Photochemistry of fluorene derivatives. *J. Chem. Soc. D* **1969,** (21), 1249-1250.
21. Ireland, J. F.; Wyatt, P. A. H., Acid-Base Properties of Electronically Excited States of Organic Molecules. In *Advances in Physical Organic Chemistry*, Gold, V., Ed. Academic Press: 1976; Vol. 12, p 131-221.
22. Tolbert, L. M., *Comprehensive Carbanion Chemistry*. Elsevier: Amsterdam, 1987.
23. Budac, D.; Wan, P., Excited-state carbon acids. Facile benzylic carbon-hydrogen bond heterolysis of suberene on photolysis in aqueous solution: a photogenerated cyclically conjugated eight .pi. electron carbanion. *J. Org. Chem.* **1992,** *57* (3), 887-894.
24. Wan, P.; Krogh, E., Contrasting photosolvolytic reactivities of 9-fluorenol vs. 5-suberenol derivatives. Enhanced rate of formation of cyclically conjugated four .pi. carbocations in the excited state. *J. Am. Chem. Soc.* **1989,** *111* (13), 4887-4895.
25. Tomioka, H.; Nakamura, H.; Izawa, Y., Irradiation of diazofluorene in alcohols: unusual behaviour of fluorenyl ethers. *J. Chem. Soc., Chem. Commun.* **1983,** (19), 1070-1071.
26. Aguilera-Iparraguirre, J.; Curran, H. J.; Klopper, W.; Simmie, J. M., Accurate Benchmark Calculation of the Reaction Barrier Height for Hydrogen Abstraction by the Hydroperoxyl Radical from Methane. Implications for CnH2n+2 where n = 2 → 4. *J. Phys. Chem. A* **2008,** *112* (30), 7047-7054.
27. Tishchenko, O.; Truhlar, D. G., Benchmark Ab Initio Calculations of the Barrier Height and Transition-State Geometry for Hydrogen Abstraction from a Phenolic Antioxidant by a Peroxy Radical and Its Use to Assess the Performance of Density Functionals. *J. Phys. Chem. Lett.* **2012,** *3* (19), 2834-2839.
28. Liu, X.-Y.; Cui, G.; Fang, W.-H., Three-state conical intersection optimization methods: development and implementation at QM/MM level. *Theor. Chem. Acc.* **2016,** *136* (1), 8.
29. Harvey, J. N.; Aschi, M.; Schwarz, H.; Koch, W., The singlet and triplet states of phenyl cation. A hybrid approach for locating minimum energy crossing points between non-interacting

potential energy surfaces. *Theor. Chem. Acc.* **1998,** *99* (2), 95-99.

30. Koga, N.; Morokuma, K., Determination of the lowest energy point on the crossing seam between two potential surfaces using the energy gradient. *Chem. Phys. Lett.* **1985,** *119* (5), 371-374.
31. Smith, K. M.; Poli, R.; Harvey, J. N., Ligand dissociation accelerated by spin state change: locating the minimum energy crossing point for phosphine exchange in CpMoCl2(PR3)2 complexes. *New J. Chem.* **2000,** *24* (2), 77-80.
32. Chachiyo, T.; Rodriguez, J. H., A direct method for locating minimum-energy crossing points (MECPs) in spin-forbidden transitions and nonadiabatic reactions. *J. Chem. Phys.* **2005,** *123* (9), 094711.
33. Lundberg, M.; Siegbahn, P. E. M., Minimum energy spin crossings for an O–O bond formation reaction. *Chem. Phys. Lett.* **2005,** *401* (4), 347-351.
34. Harvey, J. N., Understanding the kinetics of spin-forbidden chemical reactions. *Phys. Chem. Chem. Phys.* **2007,** *9* (3), 331-343.
35. Hirao, H.; Kumar, D.; Que, L.; Shaik, S., Two-State Reactivity in Alkane Hydroxylation by Non-Heme Iron−Oxo Complexes. *J. Am. Chem. Soc.* **2006,** *128* (26), 8590-8606.
36. Poli, R.; Harvey, J. N., Spin forbidden chemical reactions of transition metal compounds. New ideas and new computational challenges. *Chem. Soc. Rev.* **2003,** *32* (1), 1-8.
37. Fiedler, A.; Schroeder, D.; Shaik, S.; Schwarz, H., Electronic Structures and Gas-Phase Reactivities of Cationic Late-Transition-Metal Oxides. *J. Am. Chem. Soc.* **1994,** *116* (23), 10734-10741.
38. Schröder, D.; Shaik, S.; Schwarz, H., Two-State Reactivity as a New Concept in Organometallic Chemistry. *Acc. Chem. Res.* **2000,** *33* (3), 139-145.
39. Harvey, J. N.; Poli, R.; Smith, K. M., Understanding the reactivity of transition metal complexes involving multiple spin states. *Coord. Chem. Rev.* **2003,** *238-239*, 347-361.
40. Harvey, J. N., Spin-forbidden reactions: computational insight into mechanisms and kinetics. *WIRES Comput. Mol. Sci.* **2014,** *4* (1), 1-14.
41. Yarkony, D. R., Systematic determination of intersections of potential energy surfaces using a Lagrange multiplier constrained procedure. *J. Phys. Chem.* **1993,** *97* (17), 4407-4412.
42. Manaa, M. R.; Yarkony, D. R., On the intersection of two potential energy surfaces of the same symmetry. Systematic characterization using a Lagrange multiplier constrained procedure. *J. Chem. Phys.* **1993,** *99* (7), 5251-5256.
43. Bearpark, M. J.; Robb, M. A.; Bernhard Schlegel, H., A direct method for the location of the lowest energy point on a potential surface crossing. *Chem. Phys. Lett.* **1994,** *223* (3), 269-274.
44. Ciminelli, C.; Granucci, G.; Persico, M., The Photoisomerization Mechanism of Azobenzene: A Semiclassical Simulation of Nonadiabatic Dynamics. *Chem. Eur. J.* **2004,** *10* (9), 2327-2341.
45. Levine, B. G.; Coe, J. D.; Martínez, T. J., Optimizing Conical Intersections without Derivative Coupling Vectors: Application to Multistate Multireference Second-Order Perturbation Theory (MS-CASPT2). *J. Phys. Chem. B* **2008,** *112* (2), 405-413.
46. Sheppard, D.; Terrell, R.; Henkelman, G., Optimization methods for finding minimum energy paths. *J. Chem. Phys.* **2008,** *128* (13), 134106.
47. Keal, T. W.; Koslowski, A.; Thiel, W., Comparison of algorithms for conical intersection optimisation using semiempirical methods. *Theor. Chem. Acc.* **2007,** *118* (5), 837-844.
48. Cui, G.; Thiel, W., Intersystem Crossing Enables 4-Thiothymidine to Act as a

Photosensitizer in Photodynamic Therapy: An Ab Initio QM/MM Study. *J. Phys. Chem. Lett.* **2014,** *5* (15), 2682-2687.
49. Maeda, S.; Ohno, K.; Morokuma, K., Automated Global Mapping of Minimal Energy Points on Seams of Crossing by the Anharmonic Downward Distortion Following Method: A Case Study of H2CO. *J. Phys. Chem. A* **2009,** *113* (9), 1704-1710.
50. Ypma, T. J., Historical Development of the Newton–Raphson Method. *SIAM Review* **1995,** *37* (4), 531-551.
51. J. E. Dennis, J.; Moré, J. J., Quasi-Newton Methods, Motivation and Theory. *SIAM Review* **1977,** *19* (1), 46-89.
52. Irikura, K. K.; Johnson, R. D., Predicting Unexpected Chemical Reactions by Isopotential Searching. *J. Phys. Chem. A* **2000,** *104* (11), 2191-2194.
53. Mills, G.; Jónsson, H.; Schenter, G. K., Reversible work transition state theory: application to dissociative adsorption of hydrogen. *Surf. Sci.* **1995,** *324* (2), 305-337.
54. Henkelman, G.; Uberuaga, B. P.; Jónsson, H., A climbing image nudged elastic band method for finding saddle points and minimum energy paths. *J. Chem. Phys.* **2000,** *113* (22), 9901-9904.
55. Maragakis, P.; Andreev, S. A.; Brumer, Y.; Reichman, D. R.; Kaxiras, E., Adaptive nudged elastic band approach for transition state calculation. *J. Chem. Phys.* **2002,** *117* (10), 4651-4658.
56. Zhang, J.; Zhang, H.; Ye, H.; Zheng, Y., Free-end adaptive nudged elastic band method for locating transition states in minimum energy path calculation. *J. Chem. Phys.* **2016,** *145* (9), 094104.
57. Peterson, A. A., Acceleration of saddle-point searches with machine learning. *J. Chem. Phys.* **2016,** *145* (7), 074106.
58. Koistinen, O.-P.; Dagbjartsdóttir, F. B.; Ásgeirsson, V.; Vehtari, A.; Jónsson, H., Nudged elastic band calculations accelerated with Gaussian process regression. *J. Chem. Phys.* **2017,** *147* (15), 152720.
59. Maeda, S.; Saito, R.; Morokuma, K., Finding Minimum Structures on the Seam of Crossing in Reactions of Type A + B → X: Exploration of Nonadiabatic Ignition Pathways of Unsaturated Hydrocarbons. *J. Phys. Chem. Lett.* **2011,** *2* (8), 852-857.
60. Smidstrup, S.; Pedersen, A.; Stokbro, K.; Jónsson, H., Improved initial guess for minimum energy path calculations. *J. Chem. Phys.* **2014,** *140* (21), 214106.
61. Jónsson, H.; Mills, G.; Jacobsen, K. W., Nudged elastic band method for finding minimum energy paths of transitions. In *Classical and Quantum Dynamics in Condensed Phase Simulations*, p 385-404.
62. Henkelman, G.; Jónsson, H., Improved tangent estimate in the nudged elastic band method for finding minimum energy paths and saddle points. *J. Chem. Phys.* **2000,** *113* (22), 9978-9985.
63. Bai, F.-Q.; Nakatani, N.; Nakayama, A.; Hasegawa, J.-y., Excited States of a Significantly Ruffled Porphyrin: Computational Study on Structure-Induced Rapid Decay Mechanism via Intersystem Crossing. *J. Phys. Chem. A* **2014,** *118* (23), 4184-4194.
64. Arulmozhiraja, S.; Nakatani, N.; Nakayama, A.; Hasegawa, J.-y., Energy dissipative photoprotective mechanism of carotenoid spheroidene from the photoreaction center of purple bacteria Rhodobacter sphaeroides. *PCCP* **2015,** *17* (36), 23468-23480.
65. Kitagawa, Y.; Chen, Y.; Nakatani, N.; Nakayama, A.; Hasegawa, J.-y., A DFT and multi-configurational perturbation theory study on O2 binding to a model heme compound via the spin-change barrier. *PCCP* **2016,** *18* (27), 18137-18144.

66. Watanabe, K. j.; Nakatani, N.; Nakayama, A.; Higashi, M.; Hasegawa, J.-y., Spin-Blocking Effect in CO and H2 Binding Reactions to Molybdenocene and Tungstenocene: A Theoretical Study on the Reaction Mechanism via the Minimum Energy Intersystem Crossing Point. *Inorg. Chem.* **2016,** *55* (16), 8082-8090.

67. Oohora, K.; Meichin, H.; Zhao, L.; Wolf, M. W.; Nakayama, A.; Hasegawa, J.-y.; Lehnert, N.; Hayashi, T., Catalytic Cyclopropanation by Myoglobin Reconstituted with Iron Porphycene: Acceleration of Catalysis due to Rapid Formation of the Carbene Species. *J. Am. Chem. Soc.* **2017,** *139* (48), 17265-17268.

68. Zhang, Q.; Bowers, M. T., Activation of Methane by MH+ (M = Fe, Co, and Ni): A Combined Mass Spectrometric and DFT Study. *J. Phys. Chem. A* **2004,** *108* (45), 9755-9761.

69. Frisch, M. J.; Trucks, G. W.; Schlegel, H. B.; Scuseria, G. E.; Robb, M. A.; Cheeseman, J. R.; Scalmani, G.; Barone, V.; Petersson, G. A.; Nakatsuji, H.; Li, X.; Caricato, M.; Marenich, A.; Bloino, J.; Janesko, B. G.; Gomperts, R.; Mennucci, B.; Hratchian, H. P.; Ortiz, J. V.; Izmaylov, A. F.; Sonnenberg, J. L.; Williams-Young, D.; Ding, F.; Lipparini, F.; Egidi, F.; Goings, J.; Peng, B.; Petrone, A.; Henderson, T.; Ranasinghe, D.; Zakrzewski, V. G.; Gao, J.; Rega, N.; Zheng, G.; Liang, W.; Hada, M.; Ehara, M.; Toyota, K.; Fukuda, R.; Hasegawa, J.; Ishida, M.; Nakajima, T.; Honda, Y.; Kitao, O.; Nakai, H.; Vreven, T.; Throssell, K.; Montgomery, J. A.; Jr.; Peralta, J. E.; Ogliaro, F.; Bearpark, M.; Heyd, J. J.; Brothers, E.; Kudin, K. N.; Staroverov, V. N.; Keith, T.; Kobayashi, R.; Normand, J.; Raghavachari, K.; Rendell, A.; Burant, J. C.; Iyengar, S. S.; Tomasi, J.; Cossi, M.; Millam, J. M.; Klene, M.; Adamo, C.; Cammi, R.; Ochterski, J. W.; Martin, R. L.; Morokuma, K.; Farkas, O.; Foresman, J. B.; Fox, D. J. *Gaussian 09 Rev. E.01*, Wallingford, CT, 2016.

70. Press, W. H.; Teukolsky, S. A.; Vetterling, W. T.; Flannery, B. P., *Numerical Recipes in Fortran 77: The Art of Scientific Computing*. Press Syndicate of the University Cambridge: 1996; Vol. 1.

71. Ohtsuka, Y.; Nishikawa, Y.; Ogihara, H.; Yamanaka, I.; Ratanasak, M.; Nakayama, A.; Hasegawa, J.-y., Theoretical Study on the C–H Activation of Methane by Liquid Metal Indium: Catalytic Activity of Small Indium Clusters. *J. Phys. Chem. A* **2019,** *123* (41), 8907-8912.

72. Trygubenko, S. A.; Wales, D. J., A doubly nudged elastic band method for finding transition states. *J. Chem. Phys.* **2004,** *120* (5), 2082-2094.

73. Zarkevich, N. A.; Johnson, D. D., Nudged-elastic band method with two climbing images: Finding transition states in complex energy landscapes. *J. Chem. Phys.* **2015,** *142* (2), 024106.

Chapter 5

General conclusion

In this thesis, first, a homogenous Rh-catalyzed hydrosilylation of ketone and alkene was theoretically studied to show the good performance of transition metal catalyt.Then, two cases of spin crossing reactions are introduced to show the theoretical method used in such reactions. One is a biochemical reaction and another one is the photochemical reaction. The ISC points are indeed very important to explain the reaction mechanism. At the same time, from these practices I found the difficulty in ISC point optimization. Then, one step further, to overcome the difficulty a new approach named MS NEB method was proposed. Through this method, only the geometries of reactant and product are needed to locate both ISC point, TS and the reaction pathway. Thus, no special chemical knowledge or good sense is needed for an initial guess.

In Chapter 2, reaction mechanisms of hydrosilylation of ketone and alkene with tertiary silane using Wilkinson-type catalyst were theoretically investigated on the basis of density functional calculations using ωB97XD functional. Not only traditional mechanisms, CH, mCH and outer sphere mechanism were investigated. We also proposed two new mechanisms, aCH and DH mechanism. In the aCH mechanism, a four-coordinate rhodium hydride complex formed through elimination of R3Si-Cl is a catalytically active species. In the DH mechanism, the active species is a six-coordinate complex with two Rh-H bonds. For the C=O double bond hydrosilylation, the rate-determining steps of the aCH and DH mechanisms are both acetone insertion into the Rh-H bond, and the order of the activation barriers is that DH < aCH ≈ CH < mCH. For the C=C double bond hydrosilylation, except for the mCH pathway whose rate-determining step is the hydrosilane addition reaction, the rate-determining steps of the CH, aCH, and DH pathways are Si-C reductive elimination reaction. The order of the energy barrier is that DH ≈ mCH < aCH ≈ CH. In the outer-sphere mechanism, no stable intermediate or transition state was found. Consequently, we concluded that the DH mechanism is adopted as the mechanism for the Rh-catalyzed hydrosilylation of carbonyl group while mCH or DH is adopted as that for alkenes under a condition where their active intermediates are formed. The present result revises a hypothesis that the hydrosilylation of carbonyl group is in general accomplished by the mCH mechanism. The active species in DH mechanism has one more extra Rh-H bond than that of the other pathways, and its interaction with silyl group, trans-influence, and small steric effect are the origin of the highly efficient catalytic activity, which was not reported before.

In Chapter 3, a theoretical study of myoglobin catalyzed cyclopropanation was investigated with two models. In the experiment, iron porphycene substituted myoglobin was found to be much more active than the wild-type myoglobin in the styrene cyclopropanation with EDA. With small model, the DFT calculation results explained the reactivity difference by the different number of ISC points, the position of the ISC point, and the different total activation energy. These results indicate that for spin-forbidden reactions it is necessary to optimize the structure of ISC points. On the other hand, the results by using small model already well explained the import observations from the experiment, suggesting that when there is limited resource, for a biological system, only considering the active site can get reasonable results. Also, the DFT method is demonstrated to be a good tool to study hemoprotein system. The larger model simulated both protein environment and some solvent water molecules. The calculated potential energy surfaces are similar to that of small model. Thus, the basic conclusions remain same. However, the relative potential energy of some intermediates is changed. The reasons for the changes can be attributed to two aspects. First, the protein environment can change the electronic structure of the active site. Second, the solvent water can influence the complex stability through hydrogen-bonding. Finally, we first applied FEP method to the heme system to calculate the free energy surfaces. The simulation results of the ISC points indicated that the energy of the crossing point is majorly determined by the QM part. In other words, if the QM structure is optimized to the ISC point, most of the trajectories from the simulation with this frozen QM structure are on the crossing seam. Our first trying to apply FEP method together with ONIOM method shows the possibility to evaluate the influence of the fluctuation of the protein and the solvent in an explicit way for such myoglobin system. It is worthy to mention that if enough computational resource is available, the solvent should be carefully considered not only in the simulation, but also in the single point energy evaluation.

From the practice of ISC points optimization in Chapter 3 and a case study in the first part of Chapter 4, the difficulty of the optimization procedure is well understood. Thus, we proceeded to method development for intersystem crossing system, as described in Chapter 4. Inspired by the merits of traditional NEB method, we attempt to apply penalty function method to the NEB method to develop an applicable way of MEP optimization for multiple-states reaction. The benefit of our program is that it can give ISC points and TS at the same time even for complex cases like the third tested example in Chapter 4. There is one important point we should pay attention to, the scheme of determining the ISC point candidate. In the simple cases, like the ethylene C-C bond rotation and the In_2 catalyzed C-H bond activation, two-image selection scheme performs better. However, when more ISC points are expected, we have to use a three-image selection scheme. In other words, the scheme to determine candidates for the ISC points is not unique. To sum up, the newly proposed MS NEB method can give reasonable results for calculating reaction pathway in spin crossing reactions, at least three tested examples were succeeded. Although we only tested two-state reactions, of course, this method can be generalized to more states reactions by modifying the form of the penalty function.

From the mechanism calculations, we can see, sometimes ISC point would play a role in the reaction but it won't significantly change the reaction rate like the first case study in Chapter 1.

But sometimes it will influence the reaction rate not because of its influence to the activation barrier but through the position and the number of the ISC points. There are other reports that the ISC points caused energy barrier. In general, for the spin-forbidden reactions, it is necessary to figure out the exact position of ISC points. In this thesis, the biological system was also calculated. The basic intrinsic mechanism of such reactions can be investigated by DFT method with only consideration of the active site. But this is not enough especially when we are meant to study the origin of stereoselectivity, the solvent effect, and the other protein effect. Such studies are quite important for the catalysts design, for example control mutation of protein. And, the calculation of free energy is of great meaning to the chemical reaction. FEP method is one widely used method. However, there are still a lot of difficulties in the free energy calculation for large systems. For example, there is no standard procedure to define the gradually geometrically changed intermediates. The configuration overlap conditions of these intermediates are crucial for the final results. How to find a way to select better intermediates or how to improve the efficiency of the sampling should be considered in the future.

Acknowledgements

First and foremost, I’d like thank my supervisor, Prof. Jun-ya Hasegawa, who guided me during my doctoral period. I feel lucky to join his group where I not only gained a lot of chemical knowledge but also made friends with many people. Prof. Hasegawa provided me precious opportunities to attend different academic conferences, short visit and workshop abroad. He gave me useful suggestions in academic and life. His passion in research encouraged me to overcome all the difficulties in my study. His kindness and understanding are some of my motivation to continue the research work. Most important, I learned from him to be confident, to be independent, to be strong and to be patient. He is really nice and also the group members. I should say thanks to these kind people for their helps in my daily life and research work.

A similar gratitude belongs to my collaborators. In Chapter 2, I collaborated with Prof. Hideo Nagashima (Kyushu University) and his group members. In Chapter 3, the experimental part is done by Prof. Takashi Hayashi (Osaka University) and his co-workers. I got many useful suggestions from them. In chapter 4, the research topic about photochemical reaction was collaborated with Prof. Tamaki Nakano (Hokkaido University) and his group members. Also, I got expert advices from Prof. Xin Xu (Fudan University, China) and other members in his group. I enjoyed the discussions with these collaborators.

I also want to thank several former members in Hasegawa’s group. Prof. Naoki Nakatani (Tokyo Metropolitan University) is another important person who guided me into the scientific research. Prof. Akira Nakayama (the University of Tokyo) often helped me when I met software problems. Dr Yue Chen, the former postdoctoral, he shared with me his experience and knowledge in computational chemistry. And, he and his wife told me useful tips about life in Japan when I first came

here.

Special thanks should be given to Chinese Scholarship Council (CSC) who provided me scholarship for the first four years. Without this financial support, I was not able to study in Hokkaido University.

Of course, thanks must go to my parents. Although they don’t understand my work at all, they show their best support and love to me. They continuously encourage me to be brave and positive. Also, they always care about my health and my life. They are one source of my strength.

Finally, I want to thank my boyfriend, Ce Xu. Since we knew each other 9 years ago, he always listens to my complaints patiently and helps me to solve problems. He never disturbed me when I was busy. I feel happy and lucky that we have similar hobbies and we can deeply understand each other.